Mechanics and Dynamics of Dictyostelium discoideum adhesion

Dissertation

zur Erlangung des mathematisch-naturwissenschaftlichen Dotkorgrades
"Doctor rerum naturalium"
der Georg-August-Universität Göttingen

im Promotionsprogramm
"Grundprogramm Chemie"
der Georg-August University School of Science (GAUSS)

vorgelegt von

Nadine Kamprad

aus Dresden, Germany
Göttingen, 2021

Betreuungsausschuss

Prof. Dr. Burkhard Geil
Institut für Physikalische Chemie
Georg-August-Universität Göttingen

Dr. Marco Tarantola
Abteilung für Fluidphysik, Strukturbildung und Biokomplexität
Max-Planck-Institut für Dynamik und Selbstorganisation

Prof. Dr. Jörg Großhans
Institut für Entwicklungsbiochemie
Georg-August-Universität Göttingen

Mitglieder der Prüfungskommission

Referent:
Prof. Dr. Andreas Janshoff
Institut für Physikalische Chemie
Georg-August-Universität Göttingen

Korreferent:
Dr. Marco Tarantola
Abteilung für Fluidphysik, Strukturbildung und Biokomplexität
Max-Planck-Institut für Dynamik und Selbstorganisation

Weitere Mitglieder der Prüfungskommission:

Prof. Dr. Jörg Großhans
Institut für Entwicklungsbiochemie
Georg-August-Universität Göttingen

Dr. Alexey I. Chizhik
Drittes Physikalisches Institut
Georg-August-Universität Göttingen

Prof. Dr. Tim Salditt
Institut für Röntgenphysik
Georg-August-Universität Göttingen

Prof. Dr. Stefan Klumpp
Institut für Dynamik komplexer Systeme
Georg-August-Universität Göttingen

Tag der mündlichen Prüfung: 26.05.2021

”Lernen ist wie Rudern gegen den Strom. Hört man damit auf, treibt man zurück.”

old Chinese proverb, author unknown

Abstract

The amoeba *Dictyostelium discoideum* (*D.d.*) is an excellent laboratory model system for studying amoeboid adhesion. In its natural habitat, *D.d.* lives in the soil and hunts for bacteria, an environment which is very heterogeneous where surface properties changes rapidly. This phenomenon requires a high degree of flexibility from the adhesion apparatus of *D.d.*. To block amoeboid adhesion of *D.d.*, first studies used polyethylene glycol (PEG) "brushes" as surface functionalization. In the present study, it was shown that gels of PEG are a good alternative, and it was possible to identify that developmental stage of *D.d.*, axenic background and cytoskeletal fluorescence labelling can reduce the effect of surface passivation.

In a second set of experiments conducted in the present work, the focus lay on the adhesion versatility of *D.d.* to a variety of substrates, which bases on several non-specific driving forces. To specify these forces, model substrates made of silicon were used, which influence DLVO forces based in their layered structure. It was found that Van der Waals forces, hydrophobic effects and electrostatic interactions are involved in *D.d.* adhesion. Besides membrane- and glycocalyx-based interactions, these forces are complemented by additional structures, individual adhesion bonds and adhesion bond clusters of the transmembrane protein SadA (Substrate Adhesion-deficient A), while *D.d.* does not possess integrins and thus focal contacts.

Furthermore, actin foci, dynamic structures of freshly polymerised actin in the ventral membrane, have been shown to be involved in amoeboid adhesion and migration. In the present work, it was possible to analyse SadA adhesion bonds and actin foci both from a mechanical point of view employing step spectroscopy based on single cell force spectroscopy, but also in a more dynamical approach using reflection interference contrast and total internal reflection microscopy. Several established axenic laboratory strains as well as corresponding mutants deficient for components of actin-adhesome- and endocytosis-signalling were analysed.

The following two phenomena could were observed: I) reduction of the adhesion forces and step as well as spot density for inhibition of the Arp2/3 complex II) manipulation of adhesion apparatus (anchoring protein TalA, transmembrane protein SadA) increases the number of actin foci, with a simultaneous reduction in adhesion force.

Finally a quantification of the role of actin foci in adhesion and endocytosis was achieved. It was possible to show that actin foci exist independently of clathrin-mediated endocytosis, which also affects the lifetime of actin foci. Furthermore, clathrin-containing structures could also be detected after the appearance of actin foci, which may stabilise adhesive structures.

It was shown that *D.d.* is a very versatile organism that adapts substrate-dependently to the environment by non-specific adhesion. Furthermore, it could also be shown that specific adhesion of *D.d.* works very similarly to that of integrins.

Contents

Nomenclature

Acronym	Definition
αM	α-Mannosidase
AFM	Atomic force microscopy
Arp	Actin-related protein
BF	Bright field microscopy
cAMP	Cyclic adenosine monophosphate
Clc	Clathrin light chain
CLSM	Confocal laser scanning miscroscopy
CME	Clathrin-mediated endocytosis
COM	Centre of mass
ct	Cycle time
D.d.	*Dictyostelium discoideum*
ECIS	Electric cell-substrate impedance sensing
ECM	Extracellular Matrix
FD	Force-distance curve
For	Formin
GFP	Green fluorescent protein
IS	Ionic strength
k.o.	Knock-out
KDE	Kernel density estimation
$\mathcal{L}$	Long term experiments
N-wafer	Wafer with native SiO_2 layer
OTS	Octadecyltrichlorosilicane
PEG	Polyethylene glycol
PB	Phosphate buffer
RICM	Reflection interference contrast Microscopy
RFP	Red fluorescent protein
$\mathcal{S}$	Short term experiments
SadA	Substrate adhesion protein A
SAM	Self-assembled monolayer
Scar	suppressor of cAMP receptor
SCFS	Single cell force spectroscopy
SD	Spinning disk microscopy
SibA	Similar to integrin β
Tal	Talin
TIRFM	Total internal reflection fluorescence microscopy
T-wafer	Wafer with thick/thermal grown SiO_2 layer
V.d.W. forces	Van der Waals forces
WT	Wildtype cells

1 Introduction

One of the most common cause of death worldwide is cancer[1]. For metastasis a high degree of dynamics are relevant for spreading, but also variability and order. Central features of the cellular adhesion apparatus are often identified as causes of dissemination[2]. A similar interplay of adhesion and cell migration is also required from immune cells patrolling the blood vessels, e.g. processes of tumbling and extravasation to find centres of inflammation. In all these processes the right balance between repulsive and adhesive structures promotes migration, and strong perturbations can lead to the cell becoming less motile, up to slipping or swimming. In higher eukaryotic cells the adhesion apparatus is specialized and optimized for the specific underlying substrate, which is usually the extracellular matrix (ECM), other cells or whole tissues. This environment is essential for regulatory functions of cells and contributes substantially to cancer cell migration, immune cell function as well as embryonic development of tissues and complex organs. The ECM of higher eukaryotes has ubiquitous structures composed for example of proteoglycans, growth factors or filaments containing tripeptide Arginine-Glycine-Aspartate (RGD) -rich structures. These structures specifically interact with integrins, the major adhesive cellular transmembrane protein. Conditions where integrin-ECM interactions are altered can influence the above mentioned development or invasion phenomena.

Amoeboid adhesion can be regarded as an ancestral version of mammalian cell adhesion. Its prime features are: integrin-free, non-specific adhesion fuelled by contractile forces and therefore under control of cortical tension. Furthermore, they have very bulky cell processes and the ability to squeeze through pores in three-dimensional environments[3]. This phenotype is often found for chemotacting cells. It is therefore described in early metastasis for cancer cells but also in immune system cells like dendritic cells. As a simple laboratory model system to study amoeboid adhesion we used the amoeba *Dictyostelium discoideum* (*D.d.*). Compared to several eukaryotes, *D.d.* dwells in the soil, which is very heterogeneous. Surface properties like particle shape, particle size, porosity, composing material change constantly. Water can accumulate in small cavities and minerals can dissolve from the soil, so the ionic strength can change quickly over orders of magnitude requesting a high degree of flexibility from the *D.d.* adhesome.

A common method of passivating a substrate and thus to block amoeboid adhesion is coating the substrate with macromolecular "brushes" of polyethylene glycol (PEG)[4]. However, when the density or molecular weight of PEG is too low, cellular processes can compensate the effect of the repulsive bulky head-groups. This leads to the first aim of this dissertation:

I) Is there an efficient protocol to reliably prevent the adhesion of *D.d.*?

A gecko is able to climb up vertical glass panes by increasing the contact area on the tip of its toes, called seta (arrays of densely packed hair-like protuberances). This raises the question of whether the adhesion of *D.d.* is similarly non-specific to that of a gecko, from which the following second objective is derived:

II) Can we identify and quantify forces involved in *D.d.* adhesion by intelligent substrate design?

To answer this aspect, multi-layer model substrates were used, as these systems can modify Van der Waals forces. Additionally, the surface coating gives us the possibility to change the wettability and thus make a statement about the strength of the hydrophobic effect. Finally, varying the cell culture buffer composition allowed us to study the influence of electrostatics on amoeboid adhesion.

In this work, atomic force microscopy-based single cell force spectroscopy was carried out as the main adhesion sensing technique. Here, a single cell is attached to a cantilever and the characteristic force-distance (FD) curve measured: the cell is pressed onto a substrate of our choice and after a specific contact time, which allows adhesion clusters to be formed, again detached from the substrate. Thereby a variety of different rupture events can be observed depending on the type of bond or bond cluster. These FD curves allow the quantification of adhesion force and adhesion work. Furthermore step spectroscopy captures key features of the rupture events.

When taking a closer look into the interface between the cell and the substrate, we see that not the entire cell is connected to the surface. Within the total contact area, there are areas of close substrate proximity (30 nm). The lateral surface distance is usually 100 nm. As *D.d.* does not posses integrins, the question remains which proteins mediate its adhesion that are also integrated into the cell membrane and connect the cell to the substrate. *D.d.* expresses two major adhesion proteins, one being a protein that has a minor similarity to integrin β, SibA, which has multiple isoforms due to alternative splicing, making it very difficult to handle and impossible to tag this protein so far. It also expresses the substrate adhesion protein called SadA, which we have studied in the present work both in a fusion protein version as well as in a cellular knock-out form. Both proteins are known for their importance in the adhesion of vegetative *D.d.*. However, it is still unclear how they connect to the actin network, thus how similar they are to focal contacts. Actin-rich structures, so-called actin foci, have been described as novel feet[5] in the past and are supposed to be involved in adhesion, which leads to the third hypothesis:

III) Actin foci represent signalling hubs relevant for the adhesion of *D.d.*

For this purpose, actin foci were mainly characterised by total internal reflection fluorescence microscopy (TIRFM). Due to its experimental design, this method is ideally suited for the investigating of dynamical reorganisation at the ventral side of cells. To study actin foci, the actin binding domain LimE fused to various fluorescent proteins was used. In addition, the influence of key actin binding proteins on properties of actin foci was studied using deletion or inhibition approaches.

However, the term 'feet' is misleading, as these propulsions can also reflect membrane ruffles or contour deformations linked to actin waves and therefore the mechanism of substrate detachment can vary. Tanaka et al.[6] have furthermore shown that the membrane turnover rate controls the migration speed: both apical and basal membrane move towards the rear in a retrograde fashion depending on exo- and endocytosis mediating the excess membrane recycling from back to front.

Clathrin is an essential protein for fluid phase, membrane or protein uptake from the plasma membrane by clathrin-mediated endocytosis (CME). In mammalian cells, clathrin has been shown to play an additional role in cell adhesion, both in the disassembly of focal adhesion and in the formation of persistent clathrin-coated structures on stiff substrates. Recent studies by Amato et al.[7] showed that the amoeboid CME shares characteristics with CME of mammalian cells. Rac regulates parts of actin nucleation-promoting factor Wiskott-Aldrich syndrome protein (WASp) functions. However, the binding motif of WASp inhibits Rac activity. WASp without a functional binding domain was localised to clathrin pits during endocytosis and appears to activate the Arp2/3 complex.

Here, the membrane is pinched off by a ring of actin, which cannot be clearly distinguished from an actin focus, resulting in the last hypothesis:

IV) Are actin foci both involved in adhesion and endocytosis?

To answer this question, co-localisation studies were performed using TIRFM with fluorescence-labelled actin and clathrin. Furthermore, clathrin-rich regions were found to have a reduced membrane-substrate distance. Therefore, TIRFM was combined with RICM to observe the movement of the membrane of actin foci.

In summary, *D.d.* is a very suitable model to study adhesion. In the following work, a number of open questions about the adhesion of *D.d.* are answered, both mechanical (e.g. forces involved, types of binding) and dynamic processes (e.g. proteins involved, lifetime, co-localisation) are investigated.

2 Background

2.1 *Dictyostelium discoideum* (*D.d.*)

D.d. is an amoeba living in the soil, where it feeds on bacteria. Within the so called vegetative cycle, when nutrients are plentiful, *D.d.* grows as single cells by binary fission, with a cell doubling time of eight to nine hours. *D.d.* is a profession phagocyte, most similar to the phagocytes of the innate immune system in mammalian such as macrophages and neutrophils[8]. Evolutionary pressure, like darkness or wetness[9], can best be countered with genetic diversity, which is why *D.d.* reproduces sexually in a second cycle, the so called sexual cycle.

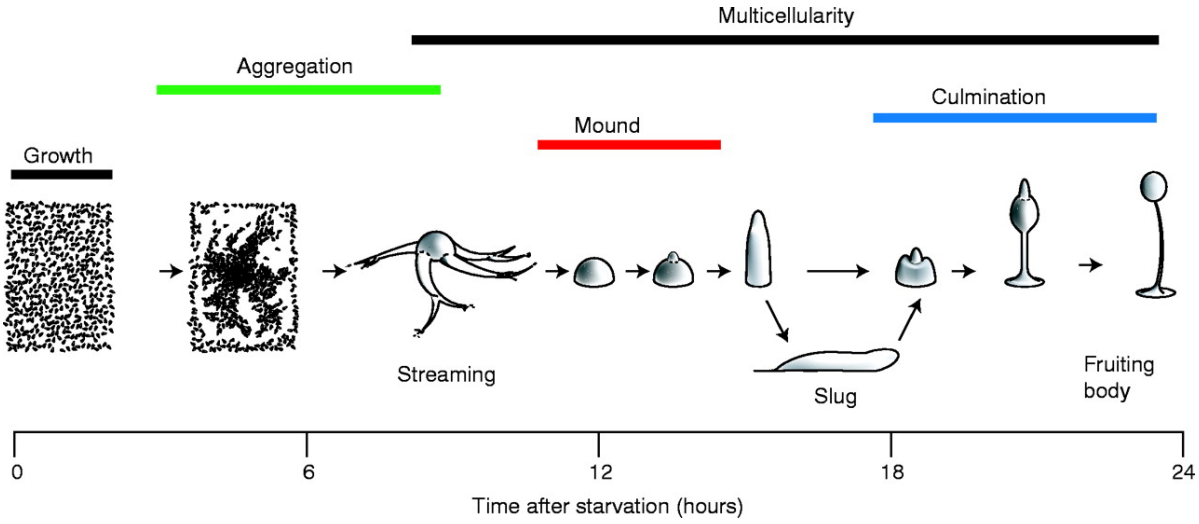

Figure 2.1: Social life cycle - After starvation has started, single cells start aggregating. The multicellular phase starts with the streaming state, followed by the mound state. In the culmination state the fruiting body is constructed. This phase can be delayed by the transient slug state. Printed with the permission of the publisher[10].

Starvation forces major changes in the third and most studied social life cycle of *D.d.*, as shown in figure 2.1. Cyclic AMP (cAMP) is synthesised and secreted by the *D.d.* cells, which promotes aggregation. The cell surface contains cAMP receptors (cAR) to target the cAMP, promoting the dissociation and activation of a heterotrimeric G protein. Various downstream effectors are activated which mediate chemotaxis to cAMP and the cAMP relay, as shown in figure 2.2. As a result, the signal is transmitted through the entire cell population. The chemotactic response includes activation of

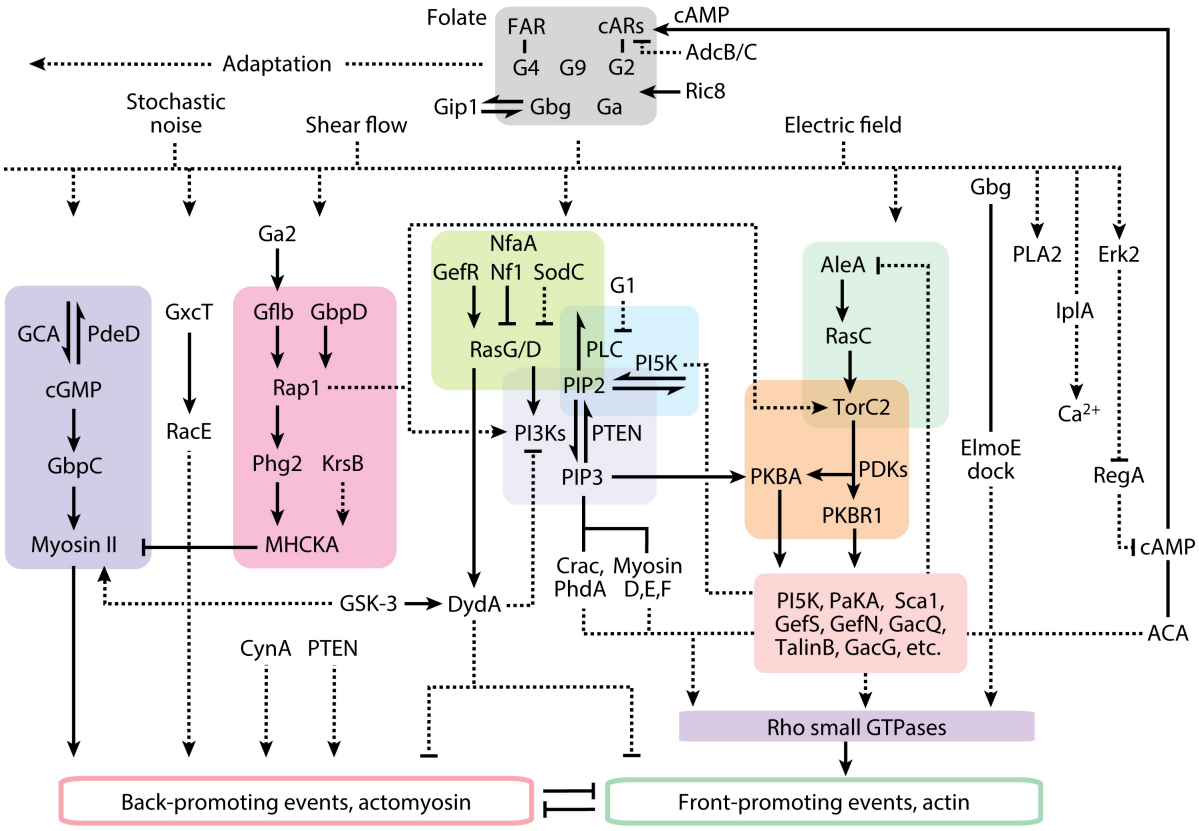

Devreotesc PN, et al. 2017.
Annu. Rev. Cell Dev. Biol. 33:103–25

Figure 2.2: Network of signal transduction pathways *D.d.* directed migration - Solid arrows, show phenotypic or stimulus-induced biochemical and biosensory compounds in comparison to the wildtype. Dashed arrows show substrate - product relationships. Solid connectors show direct interactions between components and dashed connectors indicate derived or indirect compounds. Printed with the permission of the publisher[15].

phosphatidylinositol-3-kinase (PI3K) and protein kinase B (PKB)[11], while the cAMP relay includes activation of adenylyl cyclase (ACA)[12].

The cells differentiate into multiple different cell types, followed by a transformation into a multicellular organism ($\approx 10^5$ cells), called a mound. The result can initially be a slug-like structure to cover a larger area for foraging. The slug will migrate towards heat and light to reach the soil surface. Either directly from a mound or after the slug, the cells differentiate further to generate a fruiting body containing spores, which can be scattered to find new sources of food, while the stalk cells are sacrificed for this greater good[13]. This entire developmental cycle can be completed within a day[14] under laboratory conditions.

The morphological variability of *D.d.* has made it an attractive organism to investigate many cellular processes. This is favoured by a small haploid genome, making it amenable to genetic manipulation via recombinational methods. Redundancy of genomes, like in

higher eukaryotes[16], are not present. *D.d.* diverged from the animal lineage before fungi and after plants, as shown in figure 2.12, the genome is fully sequenced and has retained much of the ancestral eukaryotic genome[16]. *D.d.* possesses a number of genes that have been subsequently lost in other lineages, most notably in the contracted genome of *Saccharomyces cerevisiae*[17]. Simple genetic manipulation is coupled with the ability to generate a large number of cells for biochemical studies as well as for fluorescence microscopy.

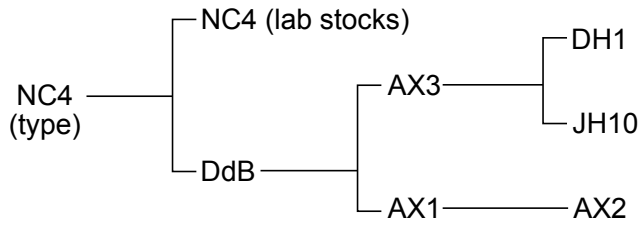

Figure 2.3: Relationships *Dictyostelium* strains - Simplified genealogical tree with the NC4 as origin and the relationships between common laboratory strains. Based on [18].

D.d. is isolated from the soil and an efficient phagocyte. Cell cultures without bacteria have both genetic and biochemical advantages. Therefore, the independent axenic strains AX2 and AX3 were created to grow on an axenic medium that was free from bacteria or particles[19, 20, 21]. All laboratory strains are derived from NC4, which was isolated in 1933 in North Carolina[18], as shown in figure 2.3. Bloomfield et al.[18] pointed out that there are differences between the strains which relate to several gene deletions and provoke strong phenotypic differences. Later he showed that the axenic strains always have a mutation in RasGAP NF1, which probably leads to increased macropinocytosis[22]. DH1 is a uracil auxotroph mutant[23] and JH10 is a thymidine auxotroph[24], which were mainly used in genetic studies.

Within this work the wildtype strains AX2, AX3 and DH1 were used, which can be grown in the simplified axenic HL5 medium[25] at room temperature. The cultivation of *D.d.* under laboratory conditions is simple, inexpensive and easily accessible for biochemical, molecular and cell biological studies.

2.2 Cell-substrate adhesion in mammalian cells

Cell-substrate adhesion is essential for cellular motion. In order to connect and interact with the substrate, proteins are needed in the plasma membrane. Therefore mainly transmembrane proteins are involved, which have to be in a right balance between adhesive and repulsive structures. If the amount of adhesive structures is too high, the cell is stuck and unable to migrate. If the amount of adhesive structures is too low, the cell has no grip and cannot migrate. These proteins are also used by the cells to obtain information on their environmental properties, for duro-[27], rheo-[28] or haptotaxis[29].

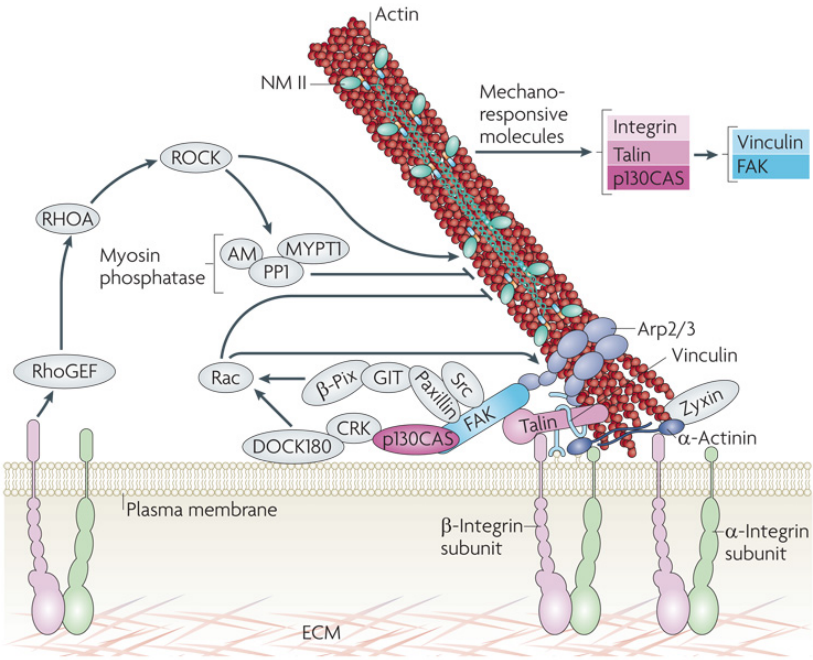

Figure 2.4: Integrin-mediated adhesion - Sketch shows the actin cytoskeleton, which is linked to integrin by actin binding proteins (talin, vinculin and α-actinin) and can interact with the extracellular matrix (ECM). Downstream processes (Rho-GTPase, like Rac) are activated by kinases (FAK) and adapter proteins (paxillin). Printed with the permission of the publisher[26].

In mammalian cells, integrins are the most important adhesion proteins. It is a transmembrane protein consisting of an α and a β-chain with an extracellular binding domain, which interacts very well with the Arginine-Glycine-Aspartate (RGD) amino acid sequences of molecules from the extracellular matrix (ECM), such as collagen or fibronectin. Patches of integrins, cluster like structures formed on the ventral side of the cell, adhere to the substrate by so called focal adhesions. These structures are connected to the actin cortex by a whole cascade of actin binding proteins including, paxillin and vinculin (figure 2.4). In addition, anchoring proteins (e.g. talin) and cross-linkers (e.g. α-actinin) reinforce the network. Furthermore it supplements with contractile activity by non-mussel myosin II (NMII).

D.d. migrates very similar to neutrophils. Cell migration is a complex, dynamic process that requires continuous transformation of the cell architecture. Key components are small GTPases, a kind of molecular switch that temporarily and locally regulates signals. Rho regulates the formation of contractile actomyosin filaments. The polymerisation of actin, to form peripheral lamellipodial or filopodial protrusions, is regulated by Rac and Cdc42. All the above-mentioned GTPases are involved in the formation of integrin-based adhesion complexes[30], as shown in figure 2.4. In addition, Cdc42 is essential for cell polarity[31].

2.3 Adhesion-relevant forces and measurement techniques

2.3.1 Forces

On a macroscopic level, *D.d.* adheres with the whole ventral side of the cell body to the substrate. The zoom-in of figure 2.16A shows that only parts of the cell have a direct contact to the underlying substrate mediated by proteins. At a microscopic scale, single atoms, which are part of the protein, interact with single atoms from the substrate. These atoms interact based on attractive and repulsive forces, which add up to the adhesion strength of the cell. In an aqueous environment, the following forces are important, which can be sorted into short range (hydrogen bonds and hydrophobic interactions) and long range forces (Van der Waals forces, electrostatic interaction, steric repulsive forces).

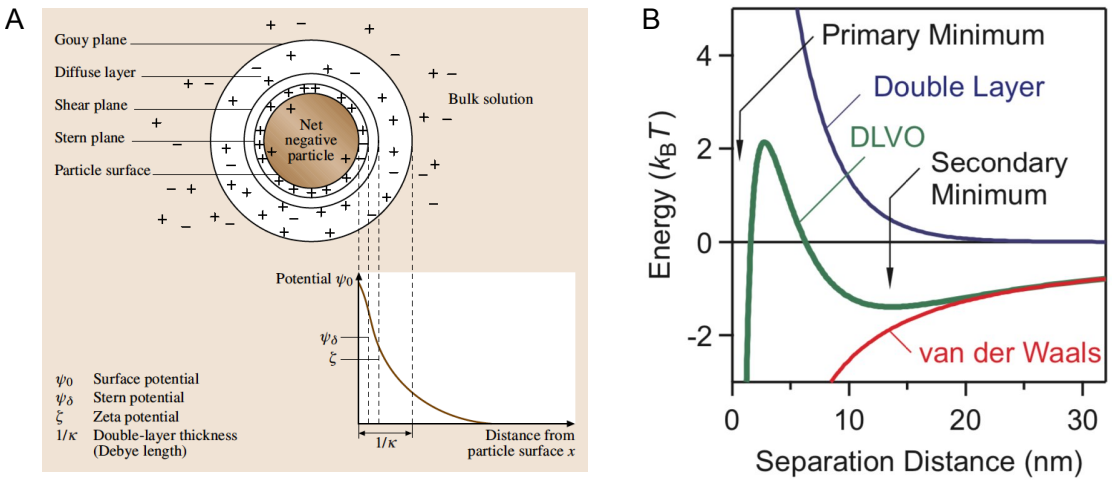

Figure 2.5: Forces near the surface - A: Electrical potential and double layer surrounding a charged particle in a polar liquid. Printed with the permission of the publisher[32]. B: Potential energy profile for two particles with equal charge. Combination of double layer forces (blue line) and Van der Waals forces (red line) can be summarized in the DLVO theory (green line), which show two characteristic minima. Printed with the permission of the publisher[33].

In a liquid, a sample gets ionized or surface groups dissociate and the charged atoms cooperate by electrostatic interactions. In addition, ions from the solution can be adsorbed by the substrate (figure 2.5A), which are influenced by ion concentration or the pH. This effect can be quantified by zetapotential measurement. A further layer of ions will be adsorbed, forming a stationary electrical double layer followed by a diffusive layer. The electrostatic interaction potential between two objects in solution decreases exponentially with increasing distance, as shown in the blue line of figure 2.5B.

Van der Waals (V.d.W.) interactions arise between electrical dipoles, which are classified as follows:

1. Keesom interaction: dipole-dipole interactions of permanent dipoles
2. Debye interaction: forces between a permanent dipole and a induced dipole, which is induced by a electrical field of a permanent dipole
3. London interactions: between two induced dipoles

All named V.d.W. forces are geometry-dependent[34]. The red line of figure 2.5B shows the distance dependent V.d.W. forces for two equal particles with the same charge. Steric repulsion between atoms arises from the superposition of their electron clouds, together with attractive V.d.W. interactions between the atoms. The scientists Derjaguin, Landau, Vervey and Overbeek (DLVO) developed a theory on the fundamental interaction of colloidal particles. The DLVO theory assumes that the interaction of two interfaces can be described approximately as follows

$$W(h) = W_{vdW}(h) + W_{DL}(h), \tag{2.1}$$

where $W(h)$ is the total energy per unit area as a function of distance h. The DLVO theory sums Van der Waals forces W_{vdW} and the double layer interactions W_{DL}, as shown in the green line of figure 2.5B. V.d.W. forces dominate at large and small distances, while at intermediate distances the double layer force plays a predominant role. At h=0 the energy profile is infinitely deep, due to repulsive forces at short distances. The combination of these forces creates a deep attractive well, the primary minimum. With increasing distance, the energy profile then passes through a maximum, followed by a shallow (secondary minimum).

In an aqueous solution hydrogen bonds appear between water molecules. Specifically they occur between electronegative atoms and hydrogen atoms, but can also exist in other compounds. These bonds are relatively weak (-20 to -30 kJ/mol[35]) and depend on the electronegativity and size of the participating atoms. When the polar water comes into contact with a non-polar surface, the water molecules are forced to increase the number of hydrogen bonds with each other. These hydrophobic interactions can be measured by water contact angle measurements.

2.3.2 Cell adhesion assays

There is a plethora of established cell adhesion assays, as shown in figure 2.6, which differ in scope of work and analysis as well as their information content. In general one can distinguish between bulk and single cell assays. The simplest of the bulk assays is the wash assay. Cells are seeded on a substrate. After a certain incubation time, they are washed off with buffer and the fraction of cells that remain attached to the substrate is measured. Neither the shear force nor the force distribution can be estimated. Thus the assay is not easy to control and reproduce. In contrast a spinning disc[36] or a flow chamber can be used, which are hydrodynamic assays. The system allows better control

by the pump or the rotating speed of the disc. There is a high reproducibility of the data, a wide applicable force range as well as the possibility of a height throughput. However, the force acts on the cell only parallel to the surface, as shear force, and is geometry-dependent. Based on the hydrodynamic laminar flow profile, the forces near the border are lower then in the middle of the channel. The exact force acting on each cell cannot be quantified.

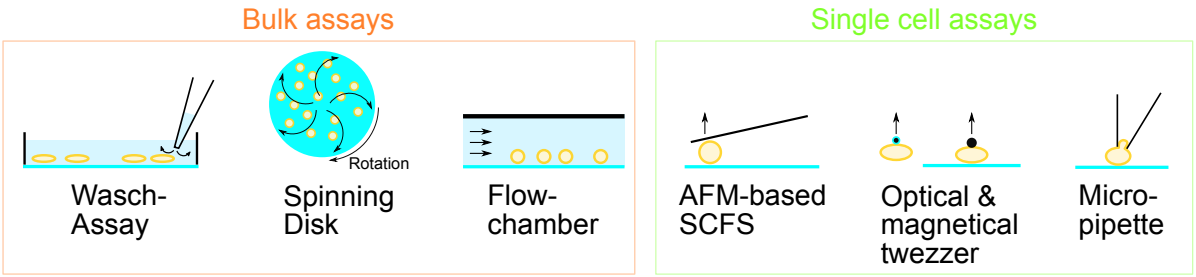

Figure 2.6: Overview of cell adhesion assays - Cell adhesion assays can be divided into bulk and single cell assays. Some common example of the two groups are shown.

In comparison single cell assays measure the adhesion force of every cell separately. The angle of the force acting on the cell can be changed, but most measure forces normal to the surface. These kind of assays are time consuming since the diversity of individual cells must be taken into account. To obtain a statistically significant result, a large number of cells must be measured. The micropipette has the advantage that a single cell can be picked immediately, but the forces to fix the cell are big and can trigger the cell and manipulate the result[37]. Forces from μN down to 1 nN can be measured, but with a low resolution. The resolution of optical tweezers is quite high (0.1-100 pN), but stronger adhesion forces cannot be detected[38]. The setup is very complex and restricted to low detachments forces. Atomic force microscopy based single cell force spectroscopy (SCFS) has an intermediate work range from 10 pN up to 100 nN and has the advantage that the cells stick directly on the tipless cantilever. The resolution is very high, the range of applicable force large and the contact conditions can be controlled very well. Kahili et al.[39] named further detachment techniques as well as attachment assay, as already named.

Schwarz et al.[40] summarized setups to measure traction forces on soft substrates, which has to be combined with optics (super resolution microscopy, light sheet microscopy).

2.3.3 Modelling biological adhesion

To measure the adhesiveness in a quantitative manner, we primarily used AFM-based SCFS. Instead using the cantilever as the indenter, a single cell was immobilized at the front of the cantilever as shown in figure 2.7A&B. Characteristic force-distance curves can be generated. To model such a setup, Witt[41] approximated the biological cell as a liquid droplet, as shown in figure 2.7A. The geometry of the cell can be described with

$U(r) = sin(\beta)$, where r is the distance to the axis of symmetry and β is the angle of the normal of the cell membrane and the symmetry axis. The radius R_0 is measured in the equatorial plane.

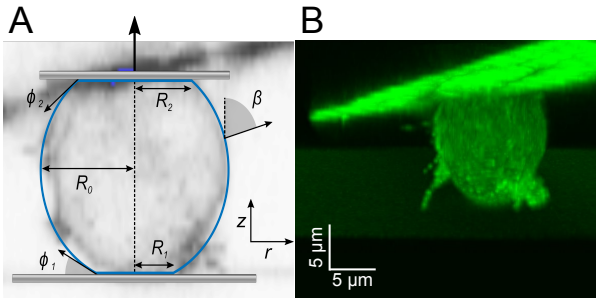

Figure 2.7: Geometry of a *D.d.* cell during detachment by AFM - A: Vertical section (from figure B) of a *D.d.* cell immobilised at a cantilever during detachment. On top the parametrization of the cell: β, angle between the normal on the cell membrane and the cell axis; R_1, contact radius between cell and substrate; R_0, equatorial cell radius; R_2, contact radius between cell and cantilever, ϕ_1 contact angle towards the substrate; ϕ_2, contact angle between cell and cantilever. B: Confocal image shows geometry of a single cell attached to the cantilever and exposed to a pulling force of 0.2 nN. Cell is visualized with GFP-tagged cAMP receptor (carA-1). Printed with the permission of the publisher [41].

The shape of the cell is determined by the variation of the free energy function, with the assumption that the volume is constant. A cell in suspension is approximated as a sphere with an initial radius R_{susp} and an initial volume $V = 4/3\pi R_{susp}^3$.

Since the adhesion to the cantilever and the substrate might be different, the upper and lower hemisphere of the cell have to be treated separately, resulting in the following volume:

$$V = \int_{R_1}^{R_0} \pi r^2 \frac{U(r)}{\sqrt{1-U(r)^2}} \mathrm{d}r + \int_{R_2}^{R_0} \pi r^2 \frac{U(r)}{\sqrt{1-U(r)^2}} \mathrm{d}r, \tag{2.2}$$

The shape of the cell must fulfil the force balance across the membrane. For this purpose, it is assumed that the pressure ΔP acts on the contact area πR_1^2. Together with the vertical force resulting from the membrane tension T at the perimeter of the contact $2\pi R_1 T sin(\phi)$, we get the following force F:

$$F = 2\pi R_1 T \sin(\phi_1) - \pi R_1^2 \Delta P, \tag{2.3}$$

where ϕ_1 is the contact angle.

The membrane tension T results from the initial tension T_0 and the elastic reaction of the cell to the expansion of the surface:

$$T = T_0 + K_\mathrm{A} \frac{A - A_\mathrm{susp}}{A_\mathrm{susp}}, \tag{2.4}$$

with the area compressibility modulus K_A, the area of the deformed cell A, and the initial cell area $A_{susp} = 4\pi R_{susp}^2$.

The third boundary condition is the Young-Dupré equation at the interface:

$$w = T\,(1 - \cos\phi_1)\,, \tag{2.5}$$

which describes the relation of the adhesion energy density w to the contact angle ϕ_1.

Based on equation 2.2, 2.3 and 2.5; the expected force-distance (FD) curve during an SCFS experiment can be calculated. Next to the FD curve, the cell shape can be calculated both are shown in figure 2.8.

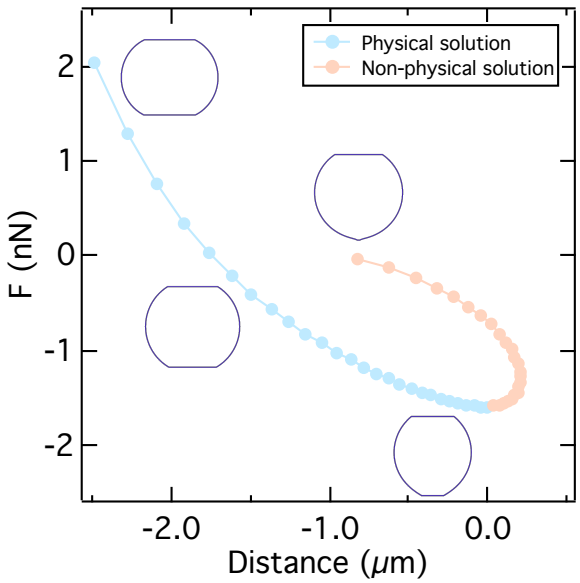

Figure 2.8: Computational force-distance curve - Force-distance curve calculated with equations 2.2, 2.3 and 2.5. In light blue, the physical solution up to the critical adhesion force is shown. Supplemented by the non-physical solution in light orange. In addition the typical shape of a cell during SCFS cycle is drawn. Printed with the permission of the publisher [41].

Until the minimum of the FD curve, the data follows the prediction. After the critical force[42]

$$F_{\text{crit}} = \pi w R_{\text{susp}} \tag{2.6}$$

is reached, the model show unstable equilibrium conditions and thus a non-physical solution. This part is referred to in the present work as the stochastic part of the FD curve, where clusters of adhesion proteins persist until they finally rupture even at higher forces and separation.

2.4 Contact guidance of cell migration

D.d. lives in the soil, which is a very heterogeneous environment. Substrate properties, like roughness, wettability and electrostatic properties, can change immediately. The adaptability makes it not easy to find substrates on which *D.d.* does not adhere, with the exception of high molecular polyethylene glycol (PEG, figure 2.9A), which can be applied to on surfaces as brushes[4] or as a gel[43]. This effect is based on the steric repulsion between PEG and the corresponding adhesion proteins[44], as illustrated in figure 2.9B. PEG is a chemically inert, water-soluble, non-absorbable and non-toxic polymer. Karmakar et al.[43] developed a method to further restrict the movement of *D.d.* using striped PEG gels for contact guidance. For this purpose a micro-patterning protocol was established to produce stripes of PEG-gel, as shown in figure 2.10. The result is a thin path lined with PEG walls on which *D.d.* usually can only move in one dimension, back and forth. Although exceptions to this migratory behaviour will be presented later in the results.

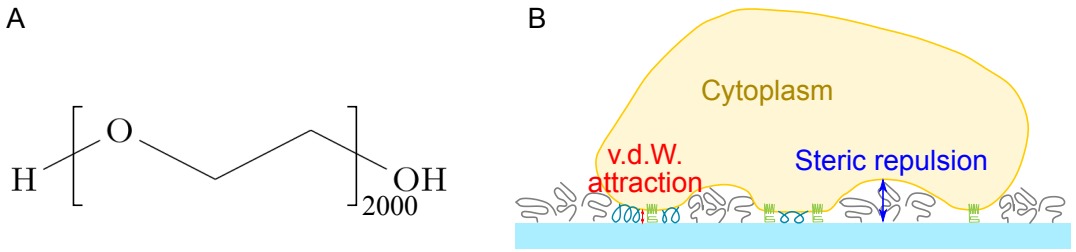

Figure 2.9: Polyethylene glycol (PEG) in cell adhesion - A: Chemical structure of high molecular (chain length: 2000) PEG. B: Schematic of PEG (grey) interfering with the adhesion of cells suppressed by steric repulsion. Adhesive structures (adhesions proteins and glycocalyx) are shown in green.

Next to the roughness of the substrate also the curvature of a substrate can influence cell migration[45], named contact guidance. Cells oriented parallel to the nanoridges move faster, form a protruding cell front and are more elongated than cells oriented orthogonally to the nanoridges[46]. In contrast, Reversat et al.[47] were able to show that leukocytes are able to migrate in a micrometer environment without adhesive structures. Furthermore Blum[48] could show that the migration of *D.d.* on cylindrical surfaces is influenced by curvature with cells preferring to move towards the highest curvature (radius $\leq 80\ \mu m$).

A further aspect is the stiffness of the substrate. Doss et al.[49] were able to show that the polarisation response correlates with the cell stiffness. The cell stiffness decreases if the active or passive cross-linking is reduced. Furthermore, he showed that softer cells are polarised on softer matrices. Durotaxis is the directional cell movement of cells on a gradient of varying stiffness. On anisotropic substrates *D.d.* as well as neutrophil-like HL-60 migrate in the direction of softer substrates[50].

Not only the substrate itself can influence cell-substrate adhesion, but also the under-

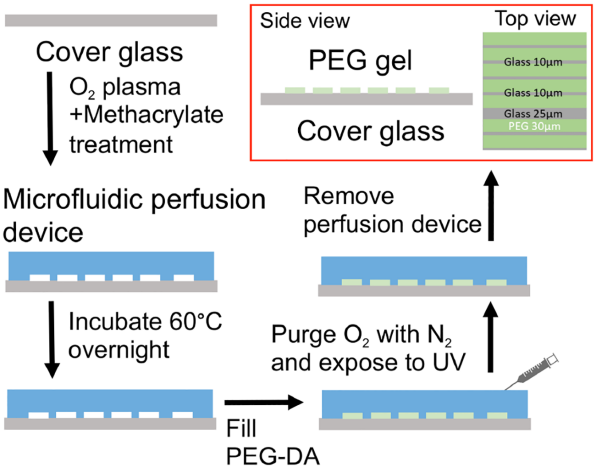

Figure 2.10: Schematic steps in micropattern substrate fabrication process - A micropattern of alternating PEG-gel and glass stripes is created by attaching a microfluidic chip to a clean microscope coverglass, reversibly bonding the device to the coverglass by overnight incubation at 60 °C, filling microchannels of the devices with PEG-gel pre-polymer, purging O_2 in an N_2 chamber, cross-linking the PEG-gel by a UV-exposure, and detaching the microfluidic chip from the coverglass.[43]

lying layer. That is why multilayered substrates can be used to measure V.d.W. forces. A well studied model substrate therefore are silicon (Si) wafer with a silicon dioxide (SiO_2) layer with a chosen thickness[51]. By changing the oxide layer thickness, the V.d.W. portion of the interface potential is varied independently of the surface properties.

In addition, the wettability of a substrate can be changed to manipulate the adhesion strength. A very common method therefore is the usage of self-assembled monolayers (SAM), where the head group interacts with the substrate and the tail defines the new surface properties. Mercapto groups are very common as heap groups on gold surfaces because the covalent interactions of Au/SAM are very strong and thus stable. For

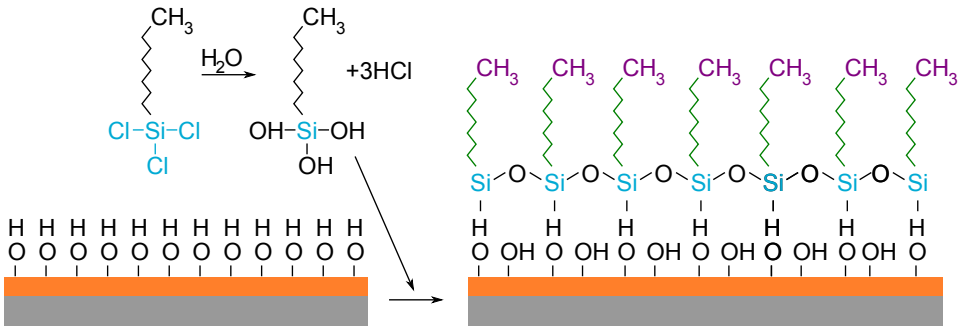

Figure 2.11: Self-assembled monolayer (SAM) on Si-wafer - Si-wafer (grey) with a SiO_2-layer (orange) on top. Headgroups (blue) of the alkylsilane interact with the substrate. Mesogene groups (green) interact by V.d.W. forces with neighbouring groups. Tail groups (purple) define the new surface properties.

Si-wafers, alkylsilanes are preferred. The large mesogene group of the neighbouring molecules interact by V.d.W. forces, which make the SAM very stable, as shown in figure 2.11.

2.5 *D.d.* adhesion

2.5.1 Adhesive structures of *D.d.* adhesion

D.d. migrates very similar to neutrophils. To adhere on a variety of substrates, like those present in the soil, the interaction to the substrate has also to be substrate unspecific but the working principle is very similar[16, 52](figure 2.12).

In several organisms (*Drosphila*[53], *S. cerevisiae*[54], *D.d.*[55]) TM9 proteins were found which seem to be relevant for adhesion. The family is characterised by a conserved structure of nine transmembrane domains, but their exact role is unclear. The inactivation of the TM9 protein Phg1A in *D.d.* strongly reduces the surface level of the SibA (Similar to Integrin Beta) adhesion molecule. Sib proteins show properties that are also found in the mammalian integrin beta chain. Beyond that, they have an extracellular Von Willebrandt A domain, a glycine-rich transmembrane domain and highly conserved cytosolic domains that interact with talin[56], as shown in figure 2.13A. The genetic inactivation of SibA leads to a partial loss of cellular adhesion[57].

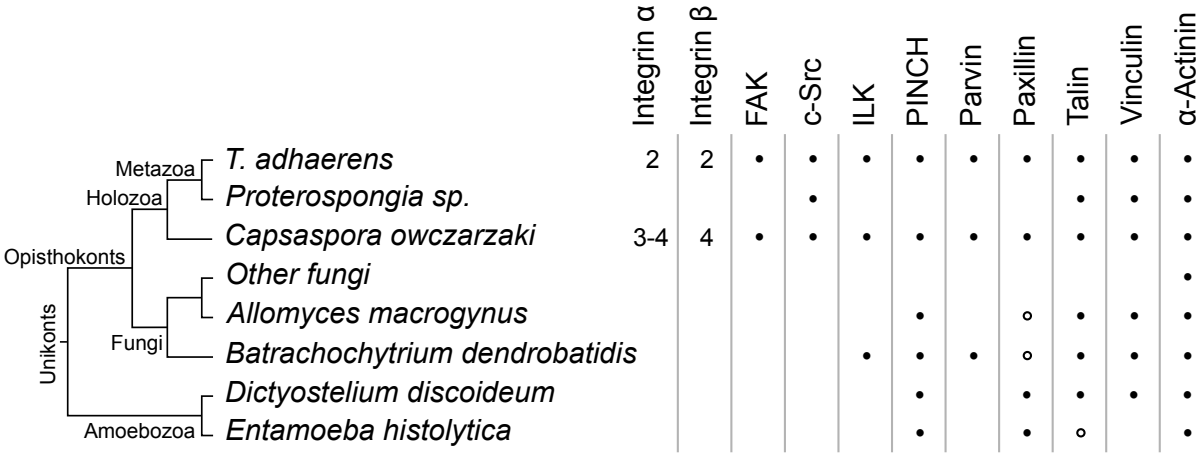

Figure 2.12: Distribution of different components of integrin adhesion complex in eukaryotic cells - The amount of integrin homologs is shown. In addition black dots show the presence of homologs, hollow dots show putative or degenerates homologs. Relationship between the species is shown by a phylogenetic tree. Figure bases on [52].

The inactivation of SadA (Substrate Adhesion-deficient) in *D.d.* also shows reduced adhesion properties[58], but no orthologues are known in other species. Similar to Phg1A, SadA has a long N-terminal domain and nine transmembrane domains, as shown in figure 2.13B, which classifies it topologically as a TM9, but has no sequence homology to Phg1A. In addition, SadA contains three EGF-like repetitions, similar to regions of

proteins known for adhesion, such as tenascins and integrins. The inactivation of SadA leads to an increase in cell size compared to the wildtype. The surface is rougher and increased blebbing can be observed[58]. The mutant also showed affected cytokinesis, an abnormal F-actin organisation and a phagocytosis defect. SadA is mainly organised in patches[58]. Kowal et al.[59] were able to identify a probable interaction partner of the SadA tail, Cortexillin I, a known actin bundling protein. Fey et al.[58] found significant down-regulation for SadA after 4 hours of starvation. After three hours of starvation, the cells start migrating to aggregate to a multicellular organism.

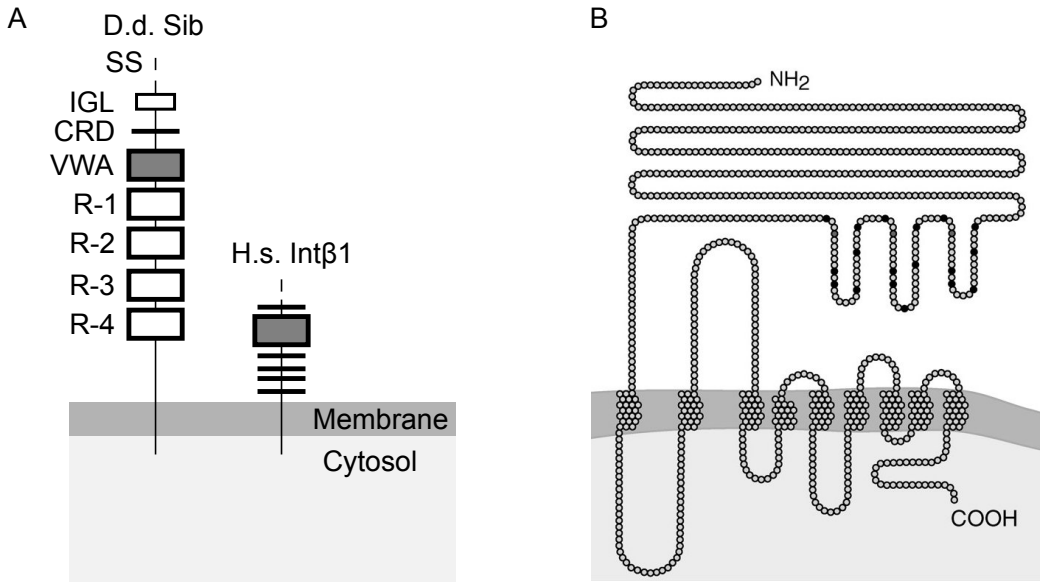

Figure 2.13: Transmembrane proteins of *D.d.* - A: Structure of *D.d.* SibA protein (left) and of human integrin β (right, H.s. Intβ1). In addition substructures are shown: cystein-rich domain (CDR), immunoglobulin-like fold (IGL), repeated motif (R), cleavable signal sequence (SS), von Willebrand factor type A domain (VWA). Based on [56]. B: Predicted protein structure of SadA. Nine transmembrane regions are shown as well as the extracellular domain. Similarities to epidermal growth factor (EGF) are highlighted, conserved cysteine (black dot) and glycine residue (dark grey dot). Printed with the permission of the publisher[58].

Neighbouring structures can form induced dipoles which attract each other in such a way that almost any surface is attracted to any other.[60] Geckos can hold their entire body weight on a vertical glass surface. Van der Waals forces of millions of 200 *nm* wide spatula structures on thousands of fine hairs on the feet make this possible[61]. Glycosylation of membrane proteins is widespread in all cell types and characterises their surfaces. Glycoproteins protrude from the cell surface and are part of the first molecules that are closely adjacent to the substrate, which forces steric interactions. Loomis et al[62] already provided first evidence that sugar residues on the surface of *D.d.* are involved in adhesion.

2.5.2 Adhesion mediator and the actin cytoskeleton

D.d. show similar migratory velocity and the ability to detect and follow chemical gradients as neutrophils[63]. In comparison to their adhesion points, the structure of adhesive regions at the ventral side of *D.d.* cells are reduced in complexity, as shown in figure 2.12. Besides glycoproteins, transmembrane proteins such as SadA or SibA (figure 2.13) represent the main components of adhesive structures instead of integrin-based focal contacts.

These proteins are connected to the cytoskeleton, in a similar manner to other eukaryotes via the actin anchoring protein talin. Talin is a large cytoskeletal protein with a modular structure: amino-terminal domain, membrane-interacting domain with sequence similarities to members of the band 4.1 family, carboxy-terminal region with F-actin and vinculin-binding domains[64]. The first talin homologue found in *D.d.* was talin A (TalA), which plays an important role in cell-substrate adhesion[65] and elastic properties of the cell[66]. TalA has a different length in wildtype (full length in AX2). The inactivation of TalA shows slightly cytokinese defects[65]. Tsujioka et al.[67] found another talin homologue, talin B (TalB). TalB is found at low but detectable levels in the growth phase, and reaches its maximum expression level in the mound stage. The inactivation of TalB stops the development in the mound stage. Mutants with similar morphological characteristics show an defect in the differentiation between pre-stalk and pre-spore cells[68]. TalB shows strong structural similarity to TalA. In addition it has a villin head group relevant for actin binding, which may allow actin bundling or separation[67]. The inactivation of TalB causes a reduction in the adhesion strength too. The deletion of both TalA and TalB causes a strong increase in speed as well as in the adhesion strength[69].

The cytoskeleton is composed of three kinds of cytoskeletal filament: Intermediate filaments, microtubules as well as microfilaments. Each of them is built out of protein monomers, which polymerise under energy consumption to fibres and posses specific functions. Microtubules consist of subunits of tubulin molecules, which are assembled into long tubular structures with an average diameter of 24 nm[71]. Together with other proteins they form complex structures such as the mitotic spindle, centrioles, cilia and flagella. They interfere with cell shape, motility and mitosis.

In contrast to microfilaments and microtubules, whose components are highly conserved and very similar within cells of a certain species, intermediate filaments show a variety in their number, sequence and frequency[72]. Despite their diversity, there is a common structure. Four dimers create a protofibril. Three to four protofibrils form an intermediate filament with a diameter of 10 nm. Intermediate filaments structure the cytoplasm and protect the cell from external stresses[73].

The actin network belongs to the microfilament system (diameter: 6 nm) and is important for cell shape, -adhesion and -migration. Actin is highly conserved and is an abundant protein, accounting for up to $5-10\%$ of total cell protein[74]. Fundamental dynamic reactions of actin are shown in figure 2.14 and are described in detail below. Actin occurs in two states: I) monomeric, also named globular actin (G-actin) II) polymerised, a right-handed, double-helical, elongated aggregate, which is known as filamentous actin

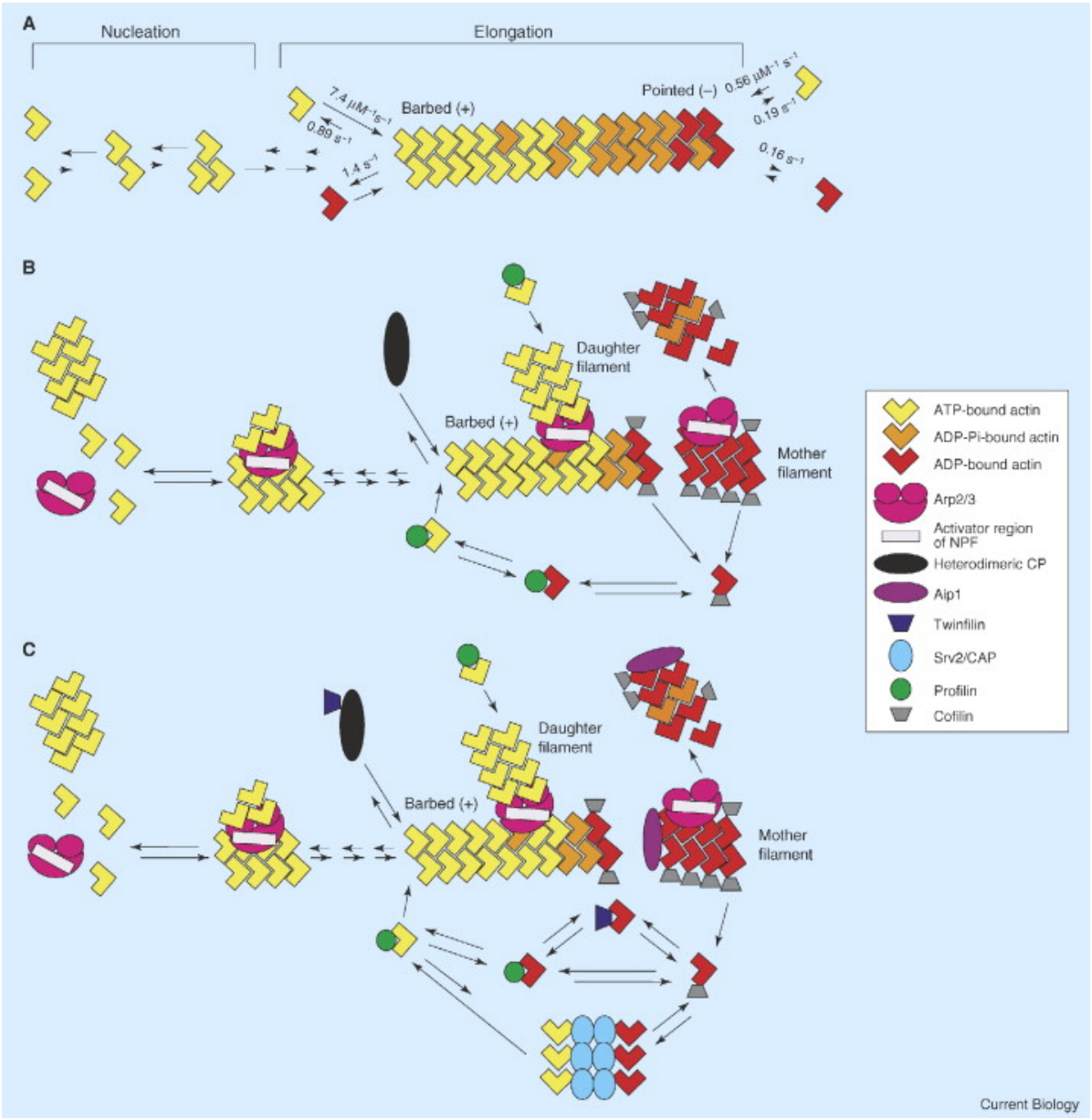

Figure 2.14: Fundamental reaction of actin - A: Nucleation and elongation of actin. Rapid growth at the barbed end and slow at the pointed end. B: Arp2/3 nucleated grows at the barbed end of a daughter filament. Actin monomer proteins, like cofilin and profilin, regulate the processes of de/polymerisation. C: Capping proteins, like Aip1 or Twinfilin, can bind and block the end or can accelerate monomer recycling, such as Srv2/CAP. Printed with the permission of the publisher[70].

(F-actin). Monomers can polymerise spontaneously to form an actin filament, which is energetically unfavourable, as shown in figure 2.14A. In the trimer stage, when three G-actins interact with each other, the polymerisation of the monomeric actin molecules with ATP binding becomes exothermic and proceeds more rapidly. Hydrolysis of the ATP molecule to ADP and inorganic phosphate takes place shortly after polymerisation and gives the actin molecule a polarisation at the so called barbed end of the filament. The dissociation rate for the ADP-containing so called pointed end, surpasses the association rate of the new monomers. As the actin filaments grow, the addition of monomers at the barbed end is favoured. The filament can reach a steady state in which elongation and dissociation of the monomers proceeds at the same speed[75], a process referred to as tread milling. Actin possesses a cation binding site on its surface, which can influence the polymerisation or filament stiffness[76].

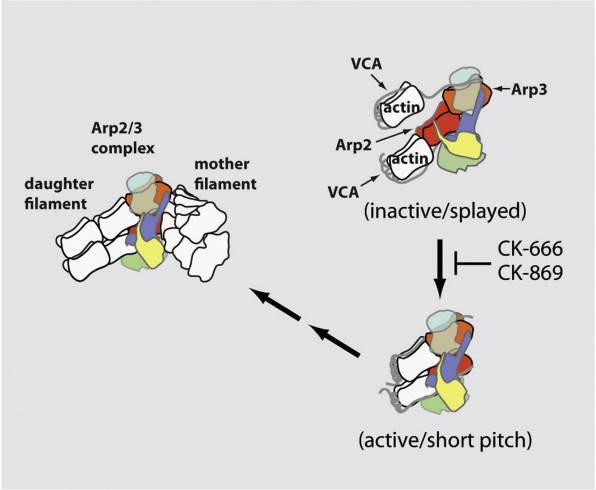

Figure 2.15: Arp2/3 complex and there inhibitors - Activation of the short pitch conformation by conformational change of Arp2 (red) and Arp3 (orange), which can be suppressed by inhibitors such as CK666 and CK869. Printed with the permission of the publisher[77].

More than 100 proteins are involved in the actin network, some of which are shown in figure 2.16A. Actin-binding proteins are capable of performing a variety of tasks: controlling the formation, degradation of actin, regulating filament branching as well as bundling to support the arrangement of actin filaments into higher order structures. Actin-monomer binding proteins control the amount and availability of monomers for polymerization, e.g. profilin. In comparison F-actin binding proteins are involved in barbed and pointed end capping, filament branching and cross-linking. Among those, the actin-related protein 2/3 (Arp2/3), Wiskott-Aldrich Syndrome proteins (WASp) and formins induce the nucleation of parallel bundles of F-actin. Elongation and nucleation of actin filaments are prevented by capping proteins[78]. Formins serve as antagonists and bind to the barbed end of the actin filament, anchoring the filament and preventing capping[79].

A single actin filament does not make up a whole network. Therefore the Arp2/3 complex branches and nucleates daughter filaments from an existing mother filament in

an angle of $70 \pm 7°$[80], figure 2.14B. The Arp2/3 complex consists of seven subunits[81]. A conformational change of the two actin-related subunits, Arp2 and Arp3, activates the complex[77]. Figure 2.15 shows both the activation of the Arp2/3 complex and its inhibition by CK666 and CK869. The Arp2/3 complex is activated by Scar (suppressor of cAMP receptor)/Wave protein, a member of the WASp-family, which regulate actin polymerisation[82].

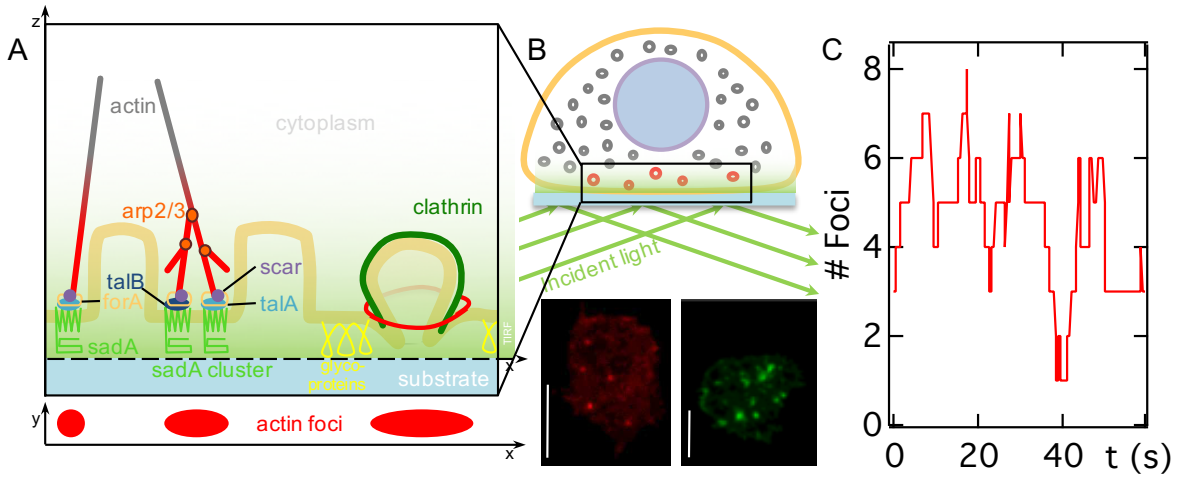

Figure 2.16: TIRFM to analyse actin foci - A: Sketch of actin foci and SadA cluster of an adherent *D.d.* cell. Both the actin and the involved adhesion mediator are coloured. Actin is illuminated by TIRFM, associated xy-projection is shown below. B: Sketch of the working principle of TIRFM. Illumination of labelled proteins within an adherent cell on top of a glass slide, limited by the penetration depth of TIRFM. In addition TIRFM image of AX3 with LimE-mRFP (left) as well as SadA0 in AX3 with LimE-GFP (right) is shown. Scale bar 5 μm. C: Time plot of the amount of actin foci (shown as an example for single AX3 cell).

Fibres, bundles and networks cannot transmit forces by themselves. This requires motor proteins, like kinesin and dynein. Both are relevant for microtubule transport or actin contraction and transport relevant myosins. *D.d.* possess 13 isoforms of myosin[16]. One of the most prominent is myosin II, which is also involved in *D.d.* movement[83]. Two myosin II motors can be connected to different actin filaments and stabilise the filaments or generate contraction forces. The force is generated by ATP-driven movement of the myosin II motor along the actin filaments. Since myosin II is composed into bipolar bundles and the actin filaments in these structures are arranged in bipolar arrays, the motor activity of the myosin II bundles leads to contraction of the actomyosin bundle, so-called stress fibres, which *D.d.* does not have. Myosin II is co-localised with adhesion regions on the ventral side of the cell, suggesting that the forces exerted may contribute to the dynamics of actin foci[5, 84].

The actin cortex is built up by a hundred nanometer thin actin layer with a network of actin filaments arranged parallel to the cell membrane. Protrusion is characterized by localised polymerisation orthogonal to the cell membrane. There are three ways how actin filaments can be organized: orthogonal, parallel or anti-parallel[85], depending on

the mechanism of polymerization, actin binding protein association or a combination of both, which will be described in the following section.

In the past, two actin-containing structures have been described which are supposed to act as "feet" in *D.d.*: I) eupodium, which only occurs in cells that are under pressure from the agar sheet[86] II) actin foci, which are observed on the ventral side of freely migrating cells[87], as shown at the bottom of figure 2.16B. Uchida et al.[5] observed: I) cell surface of actin foci is closer to the substrate II) cells are moving faster when the number of actin foci decreases III) traction forces are generated only at sites around actin foci.

2.5.3 Fluorescence and marker of actin activity

The emission of light from a substance, so called luminescence, occurs due to the relaxation of an electronically excited molecule. Fluorescence can be well explained by a Jablonski energy diagram, as shown in figure 2.17. The molecule absorbs an incoming photon and becomes exited, making a transition from ground to excited state. The wavelength of the absorbed photons is equal to the energy gap between ground and excited state. The excitation goes from singlet ground state S_0 to higher singlet state, followed by internal conversion to lowest vibrational state of S_1, within femtoseconds. The electron returns to any available vibrational levels of the singlet ground state S_0. The excitation energy is emitted as fluorescence. The total energy emitted by the system must always be equal to the excitation energy due to energy conservation. This directly leads to Stokes' rule, which states that the wavelength of the emitted photon can never be smaller than that of the absorbed photon.

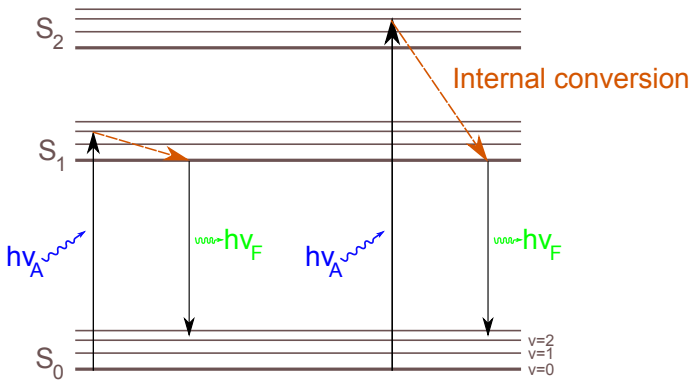

Figure 2.17: Schematic diagram depicting the fluorescence mechanism - Singlet ground state S_0 and higher singlet states are shown. Vibrational level of electronic states (v). Absorbed (blue) and emitted (green) light as well as the process of internal conversion (orange).

The emission spectrum is shifted to a higher wavelength than the absorption spectrum, the so called Stokes Shift (figure 2.18B). This effect is used in fluorescence microscopy to prevent overlapping of the absorption and emission spectrum (few nanometre to

several tens of nanometre[88]). Fluorochromes are molecules that absorb light of a certain wavelength and emit part of the absorbed light as longer-wave radiation. The colour and intensity of the emitted light are characteristic properties of the respective fluorescent molecule. Next to synthetic dyes and quantum dots, fluorescence proteins are becoming more and more important in fluorescence microscopy. Fluorescence proteins have the big advantage to be genetically introduced into cells and can be used to label single proteins. Dynamics and interactions of proteins can be monitored. In general, the chromophore of the fluorescence protein is enclosed in a β-barrel scaffold and provides a unique fluorescent probe. The ability of fluorescent proteins to fluoresce is mainly determined by the chemical structure of the chromophore. The expansion of the π-conjugated electrons determines the redshifted emission[89].

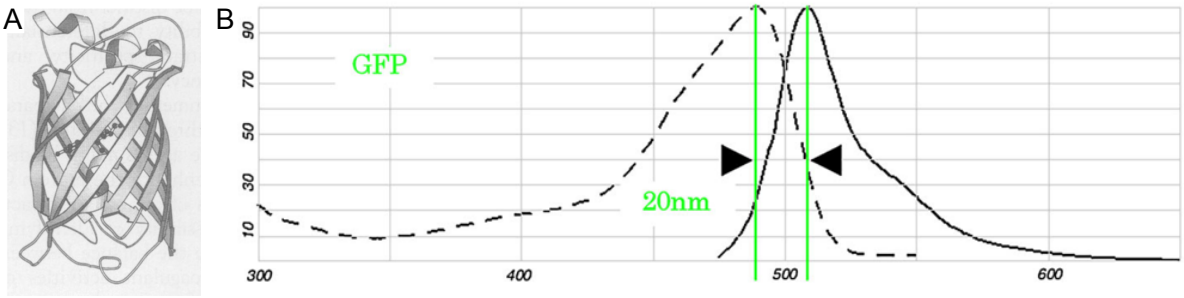

Figure 2.18: Tertiary protein structure of green fluorescent protein (GFP) - A: Barrel-like tertiary structure of the GFP, with the chromophore inside. B: Absorption (dashed line) and Fluorescence (solid line) spectrum of GFP. Signal intensity via wavelength (nm) is plotted. Stoke shift is shown in green. Printed with the permission of the publisher[88, 90].

Green fluorescent protein (GFP), as shown in figure 2.18A, is the most popular, isolated from *Aequorea victoria* and has a molecular weight of 27 kDa[91]. When excited with blue light this protein fluoresces green. GFP can be fused to other proteins as a fusion protein. When the protein of interested is expressed, the fused GFP is expressed, too. The fluorescence of the GFP allows the spatial and temporal distribution of the desired protein in living cells to be directly observed and analysed.

Eukaryotic cells show reduced auto fluorescence at longer wavelengths and are less sensitive to longer wavelength. The tropical coral *Anthozoa* expresses fluorescence proteins emitting in red and far-red. DsRed from *Discosoma spec.* was very promising, but the limitations of this probe were quickly revealed, including a green intermediate formed during protein maturation, poor brightness and obligatory tetramerisation, which led to poor localisation and often affected the function of fusion proteins[91]. Fischer et al.[92] were able to design a monomeric DsRed, named mRFPmars, and showed that it can be used for co-localization studies in *D.d.*.

Actin filaments regulate crucial processes such as cell motility, chemotaxis, phagocytosis, cytokinesis and cell adhesion. It is therefore very important to make the dynamics of F-actin in living cells visible. In the past it was very common to inject fluorescent labelled G-actin[93], which is technically very demanding and influences the polymerisation kinetics directly. Another option was to add a small amounts of fluorescently

labelled phalloidin[94], which bind to F-actin and stabilizes the compound, however thereby abolishing cellular dynamics.

An alternative is to express a fluorophore labelled fusion protein. G-actin-GFP has the disadvantage that $50 - 70\%$ of unbound G-actin is present in the cytoplasm[95], which results in an enormous background signal. For this reason, actin-binding domains (ABD) from various actin binding proteins (ABP) are preferentially utilized to create indirect probes for actin filaments.

In *D.d.* filamin, α-Actinin and LimE are common ABP, which are fused to a fluorescent protein and expressed in living cells. Filamin, also known as ABP120, is an orthogonal cross-linker and structurally homologous to human filamin[96]. α-Actinin is an anti-parallel cross-linker, which is homologous to mammalian non-muscle α-Actinin[97]. Pang et al.[98] showed that both ABDs of filamin and α-Actinin are localized to F-actin in nonpolarized cells. For polarized cells Washington et al.[85] found differences. During chemotaxis, filamin is localised on the back of polarised cells. In contrast, α-Actinin is enriched in new pseudopods and at the front of polarised cells, but is not detectable in the peripheral cortex.

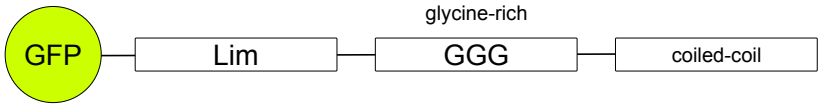

Figure 2.19: GFP-LimE fusion protein - Schematic shows full length of LimE. The positions of the domain boundaries are shown. GFP is C-terminal bound. Image based on [99].

The LIM domain was initially identified in three developmentally regulated transcription factors, lin-11, Isl-1, and mec-3 from which the acronym LIM has been derived[100]. The domain consists of a double-zinc finger motif, which stabilizes a peptide loop. *D.d.* possess three cytoskeleton-associated LIM proteins. LIMB is not associated to the actin cytoskelton[101]. LIMC and LIMD have the disadvantage of directly interacting with F-actin[102]. LimE, also known as DdLimE[99] or DdLim[103], has a LIM domain at its N-terminal region, followed by a glycine-rich segment, completed by a coil-coil domain at the C-terminus[103]. LimE, as shown in figure 2.19, is associated with Rac1A in a GTP-dependent manner, so its localization in the cytoskeleton is thought to be mediated by GTPase-dependent signal transduction pathways[103]. Rac1A is a direct activator of the SCAR complex, which may explain the affinity of LimE to the actin cytoskeleton[104]. A comparison of the LimE-GFP fluorescence profile with a phalloidin staining showed that the overlay is about 97%[105].

The coiled-coil domain of LimE is dispensable from actin binding[99]. Measurements have shown that LimE without this coiled-coil domain (LimEΔcoil) shows a lower cytoplasmic background signal, without changing the actin pattern[106].

These probes consist of large domains, compete with their endogenous counterparts and are limited to cells that can be transfected[107] and can also be used in other organisms, for example *Physarum*. Abp140-GFP labels actin fibres in *Saccharomyces cerevisiae*[108]. Riedl et al.[107] could prove that the first 17 amino acids of Abp140

were sufficient to mediate actin localization in comparison to the full-length protein. It is only conserved in close relatives of *Saccharomyces cerevisiae.*[107] The C-terminal GFP tagged version of these peptide is known as Lifeact-GFP. Lemieux et al.[95] has shown, that lifeact-GFP can be used in *D.d.* and labels F-actin in all parts of the cell with little cytoplasmic background.

However, one should not ignore the fact that fluorophores can also influence the protein sterically and kinetically.

2.6 Endocytosis in *D.d.*

Endocytosis is the uptake of particles (mainly bacteria) or liquids from the environment of a cell. Phagocytosis is driven by the activation of cell surface receptors, which bind to bacterial surface components. *D.d.* does not differ between gram-positive and gram-negative bacteria. After engulfment, phagosomes rapidly mature to generate an internal antimicrobial environment, for example via pH changes. After killing, the bacteria are digested and nutrients are extracted to support cell growth, while indigestible material is subsequently expelled via exocytosis. Nutrients can also be taken up as liquid from the environment by macropinocytosis, if an uptake across the plasma membrane into the cytosol is not possible, like in *D.d.*[109]. The originally isolated wildtype NC4 is not able to feed only on liquid media. The axenic strains all originally delineate from the isolated parental strain NC4[18] and were identified upon minimal medium optimization in different labs[20, 110]. Next to macroendocytosis (phagocytosis, macropinocytosis) microendocytosis/micropinocytosis are possible and can be divided in clathrin-mediated and clathrin-independent endocytosis.

Clathrin-mediated endocytosis (CME) is primarily responsible for the uptake of plasma membranes and their constituents (transmembrane proteins like receptors, adhesion proteins, glycocalyx). *D.d.* is able to turn over its entire plasma membrane within 10 min[112] by microendocytosis, while the amount of macropinocytosis is estimated to be 10-fold less[113]. In general, clathrin is a hexamer consisting of three light (Clc) and three heavy chains (Chc), named after their molecular weight difference (Clc: $\approx 30\ kDa$; Chc: $\approx 190\ kDa$)[114]. The three-legged triskelions assemble on the cytoplasmic surface of the plasma membrane to form complex flat polygonal grids, as shown in the schematic of figure 2.20 in step I. The presence of WASp (step II) is taken as an indicator for the beginning of CME[115]. These planar grids can persist there for several seconds[7, 116, 117], until it begins to bend as individual triskelions connect with each other. This requires initiators such as WASp, which start the actin polymerisation, as shown in step III. The Arp2/3 complex creates the network-like structure of the actin around the engulfment[117]. The beginning curvature of the grid pulls the adjacent membrane into a coated pit. When this structure separates by membrane scission, a spherical coated vesicle is released into the cytoplasm. Once the vesicle has detached itself from the plasma membrane, it quickly loses its protein shell, as shown in step VI, and fuses with the endosomes[114].

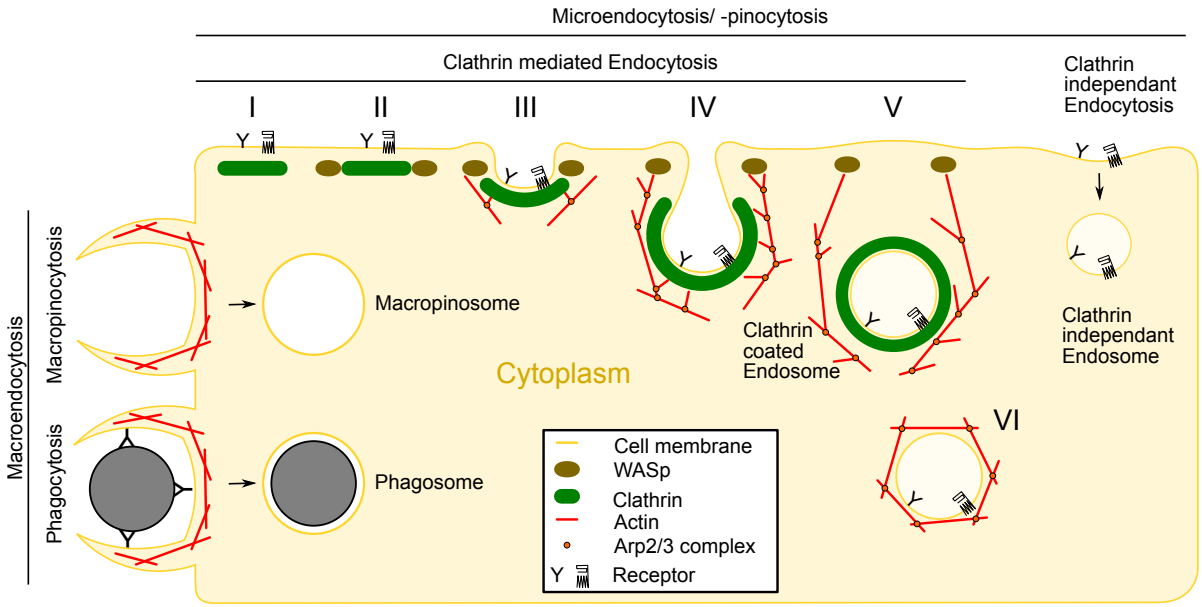

Figure 2.20: Endocytic pathways in *D.d.* - Endocytic pathways of *D.d.* is divided in two types. Macroendocytosis is an actin driven process. The uptake of fluid is named macropinoytosis. The binding and active uptake of particles (bacteria, yeast, latex bead) is named phagocytosis. Microendocytoosis/-pinocytosis, is the uptake of membrane constituents (receptors, adhesion proteins, glycocalyx). The most common one is the clathrin mediated endocytosis (CME), where I) clathrin-coated structure appears at the cell membrane II) WASp initiates the actin polymerisation III/IV) the actin network, forces by Arp2/3 start engulfment of the membrane V) clathrin coated endosome are taken up VI) endosome loses the clathrin coating. In addition there is the possibility of membrane uptake, clathrin-independent. The underlying mechanism is still unknown. Image based on [8, 111].

ChcA is essential for the grid formation[118]. However, inactivation of ChcA cause only a slightly reduced membrane turnover[112], a decreased pinocytosis and growth rate[119], as well as a aberrant cytokinesis[6].

Since a Clc binds directly to a Chc, Clc influences the interaction of the triskelions (blocking or exposing contact points, regulating clathrin assembly). In addition, the Clc interacts directly with the clathrin uncoating ATPase (hsc70)[114]. The inactivation of ClcA causes defects in development, cytokinesis and osmoregulation. They continue to form dynamic punctuate structures, but the association of clathrin with the intracellular membrane is reduced[120].

3 Materials & Methods

3.1 Cell culture and preparation

D.d. was cultured on petri dishes with HL5 medium (ForMedium^{TM}, UK) at 22 °C. For the experiments, cells were washed twice with phosphate buffer (PB, 2 mM KH_2PO_4 + 14.7 mM $Na_2HPO_4 \cdot H_2O$ at pH 6 (both Merck, Germany)) and resuspended in an aliquot of $2.5 \cdot 10^5$ cells in 1 ml PB. The cells were used immediately afterwards, to be at an early developmental stage to avoid development effects on adhesion and migration[121], only to a maximum of 3 h after starvation initiation, named vegetative cells. To induce development, the vegetative cells were pulsed for 5 hours on a shaker (100 RPM; MaxQ200, ThermoFischer, Germany) with drops of 50 nM cAMP added every 6 minutes.

Table 3.1: Calculation of the ionic strength of the phosphate buffer.

KH_2PO_4:	$\frac{1}{2} * \left((1_{K^+})^2 * c + (-1_{H_2PO^-})^2 * c\right)$	$= \underline{c}$
NaH_2PO_4:	$\frac{1}{2} * \left((1_{Na^+})^2 * c + (-1_{H_2PO^-})^2 * c\right)$	$= \underline{c}$
Buffer:	2 mM KH_2PO_4 + 14.7 mM $NaH_2PO_4 \cdot H_2O$	$= \underline{\underline{16.7\ mM}}$

For most of the assays, the cells have to be removed from a culture dish, mainly physically or chemically. In cell culture with higher eukaryotic cells, it is very common to use proteolytic enzymes (e.g. trypsin and collagenase) to remove the cells. Therefore the enzyme cleaves parts of the adhesive proteins, mainly integrin, to remove the cell. Studies of Schubert et al.[122] have shown that the cells need 10 to 60 min to recover. An intelligent alternative are temperature-sensitive culture dishes[123]. *D.d.* has the advantage to be removable from the substrate with the normal flow of a pipette (low mechanical stress) at room temperature.

In order to significantly influence the adhesiveness of *D.d.* with enzymes, glycolytic degradation of the cell exterior was done with an α-Mannosidase (αM) treatment. This involves cleaving the glycan part of glycoproteins, which has a characteristic terminal α-D-mannosyl residue[62]. For this purpose, the aliquot was incubated with 5 μl αM (stock solution, Sigma-Aldrich, Germany) for 30 min. Afterwards the cells were transfered back to PB.

To inhibit actin branching, CK666 (Sigma-Aldrich) was used, since a k.o. of Arp2/3 is lethal for *D.d.* cells[124]. The Arp2/3 complex is a seven-subunit assembly, which has to flip in an activated filament-like conformation. CK666 acts as an allosteric effector and stabilizes the inactive state of the Arp2/3 complex[77]. A concentration of 10 μM

for $5 \cdot 10^5$ $cells/ml$[125] was used. After an incubation period of 30 min the sample (AX2) was washed twice with PB. After a regeneration time of 30 min the experiment was started.

Ca^{2+} is an ubiquitous cation and is dissolved in the soluble environment of *D.d.* and regulates most aspects of cell motility. Extracellular Ca^{2+} and K^+ induces the cortical localisation of myosin II[126]. Hydrolases (including myosin) use a divalent metal co-factor (typically Mg^{2+}) to coordinate purine nucleotide hydrolysis[127]. Ca^{2+} can enter the cell through calcium channels and use important signal transduction mechanisms (often via the binding protein calmodulin) to mediate a variety of cellular actions[128]. To determine the electrostatic interactions for cell adhesion, the ion concentration in the buffer (ionic strength (IS): 16 mM, table 3.1) was increased stepwise within the osmoregulatory regime. Two kinds of ions were used: monovalent potassium and divalent magnesium. For this purpose 5 mM KCl[126] (potassium chloride, Sigma Aldrich, Germany; IS: 21 mM) was added to the running experiment. After a regeneration time of 5 min the experiment was continued. Again, 15 mM were added (IS: 26 mM) and the measurement performed. This procedure was adopted for $MgCl_2$ (magnesium chloride, Sigma-Aldrich, Germany)[126]: the concentration was increased from 0 to 5 mM (IS: 31 mM) to 20 mM (IS: 76 mM).

3.2 Preparation of the model substrates

There are two ways to influence the adhesion between cells and substrate: I) manipulating the cell or II) modifying the substrate.

The latter was done by fabricating a model substrate based on silicon wafer. In this experiment wafers with different heights of silicon dioxide were used: native 1.7 nm SiO_2-layer (N-wafer) and thermally grown 150 nm SiO_2-layer (T-wafer). Theses substrates have different Van der Waals characteristics. Since each interface contributes to the total V.d.W. force with its own Hamaker constant and properties as long as the thickness of the added layer is not bigger than the decay length of the V.d.W. force of the previous layer. Furthermore their substrate properties are very well described (isoelectric point, total surface energy, Lifshitz-van der Waals interaction energy, Lewis acid-base components,

Table 3.2: Overview of the substrate properties of N- and T-wafer as well as the influence of the silanization with OTS. Surface energy (γ) and roughness (rms) have already been published by Kreis[129]†(Ethanol-cleaned). The isoelectric point (IEP) has already been published Loskill et al.[130]‡(Ethanol-cleaned).

Substrate	$N\text{-}SiO_2$	$T\text{-}SiO_2$	OTS
γ^{tot} $(mJ/m^2)^\dagger$	35 ± 4	37 ± 3	23 ± 1
γ^{LW} $(mJ/m^2)^\dagger$	32 ± 1	32 ± 1	23 ± 1
γ^{AB} $(mJ/m^2)^\dagger$	3 ± 3	5 ± 3	≤ 0.2
rms $(nm)^\ddagger$	0.17	0.19	0.16
IEP‡	3	3	≤ 4

and RMS roughness) by Kreis[129] and Loskill et al.[130], summarized in table 3.2.

Another possibility to modify the substrate is to coat the surface. In this case a functionalization with octadecyltrichlorosilicane (OTS) was applied to change the hydrophobicity of the substrate, making hydrophilic wafers hydrophobic. An established protocol from Lessel et al.[131] was used for wafer preparation and surface characterisation. To get a very homogenous coating, the wafer was cleaned with piranha solution (50% H_2SO_4 and 50% H_2O_2; Merck, Germany) and stored in wafer boxes.

To verify the quality of the fabricated substrates, the advancing and receding contact angle (Dataphysics OCA 50, Germany) of ultra pure water (18.2 MΩ·cm, 0.055 $\mu S/cm$, NANOpure Diamond, Barnstead) was measured, as shown in figure 3.1 and table 3.2.

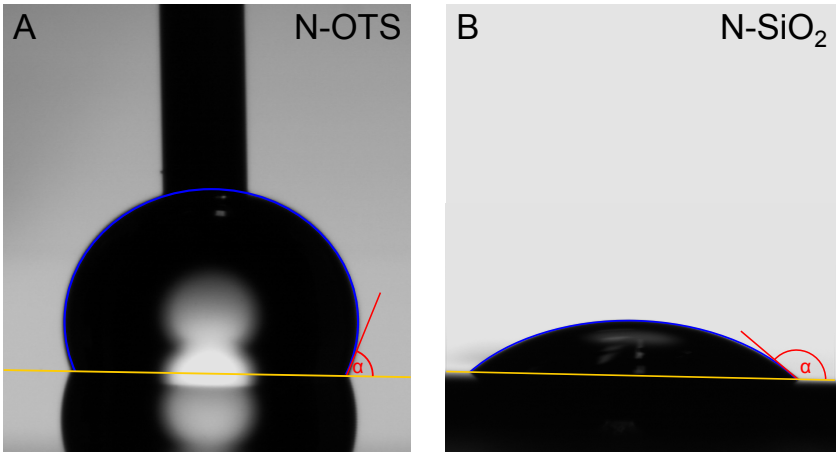

Figure 3.1: Water contact angle measurement - Hydrophobicity differences illustrated, exemplary shown for the N-wafer, by water contact angle measurements. With(A) and without(B) silanization (after piranha cleaning). Slightly modified with the permission of the publisher[41]. In addition the wafer surface (yellow), the contour of the droplet (blue) and the angle (red) between wafer and droplet.

The substrates were used for both AFM-based step analysis and sdCLSM-based flatness detection of cell. Therefore small pieces of 5 mm x 5 mm were cleaned in a ethanol-containing (ethanol absolute, p.A, ACS, Ph.Eur, USP, Chemsolute, Germany) ultra sound bath (Ultrasonic cleaner, VWR, Germany) for 5 min, dried with N_2 and fixed on a glass substrate (AFM: ø 35 mm x 1 mm, Asylum Research, UK; Optical experiments: μ-Dish, 35 mm high glass bottom, Ibidi, Germany) with two-component adhesive (JPK biocompatible glue, Germany).

3.3 Measuring cell adhesion via atomic force microscopy

3.3.1 Atomic force microscopy

Atomic force microscopy (AFM) is a scanning probe microscopy technique and an advancement of the scanning tunnel microscope further developed to measure insulating and biological samples. AFM is typically used as an imaging tool for nanometer structures, force spectroscopy or to measure bond dynamics like the lifetime and kinetic ratios. The main part of the setup is the cantilever, which is mounted on an angle of $\approx 10°$[132] on the cantilever holder on the head of the AFM. An infrared laser is reflected on the back of the cantilever, usually possessing a reflecting coating like gold, and enters a four-quadrant photodiode, that can detect the x-y movement of the cantilever. The movement in y direction is illustrated in figure 3.2. Torsion of the cantilever leads to movement in x direction. Movement in both x-y- and z-direction can be performed in a nanometer range with the assistance of piezoelectric elements and a PID feedback loop. For imaging, a fine tip at the front of the cantilever is necessary. The movement in x-y direction changes the deflection, which is converted into a three-dimensional image, based on Hooke's law

$$F = -k_c x, \tag{3.1}$$

where F is the force applied to the sample and x is the deflection of the cantilever, the reason why AFM can be used as a tool for force spectroscopy[133]. The spring constant k_c is calculated, mainly from thermal noise spectrum of the cantilever deflection by integration over the first resonance peak[134]. From the slope of the FD curve on a stiff substrate the deflection of the cantilever can be determined for a defined voltage difference of the detector, sensitivity S. Using sensitivity and the spring constant the actual voltage difference to the resulting force $F(\Delta U)$ can be determined and the set point afterwards converted into a force regime.

3.3.2 Experimental conditions and data analysis of AFM-based Single cell force spectroscopy

For the measurements of cell-substrate interaction a large number of setups are available (optical tweezer, micropipette, AFM). In this work AFM-based single cell force spectroscopy (SCFS) was used. The application ranges from single molecule unfolding[135], cell-cell[136] to tissue-tissue[137] measurements. In the following experiments a tipless cantilever was chosen. Instead of a fine tip, a single cell was used as a probe, as shown in figure 3.2. There are a variety of protocols for fixing cells (Poly-D/L-lysine[136, 138], ECM proteins[139], CellTak[140], Concavadin A-Strepravidin[141]). Adhesion promoters must be strong enough to prevent the cell from separating from the cantilever on contact with the substrate. These substances can theoretically trigger signal cascades. The advantage of this technique is that defined forces (from pico- to nanonewton) can be applied in a label-free manner without hydrodynamic effects, provided that the speed of the cantilever is not too fast.

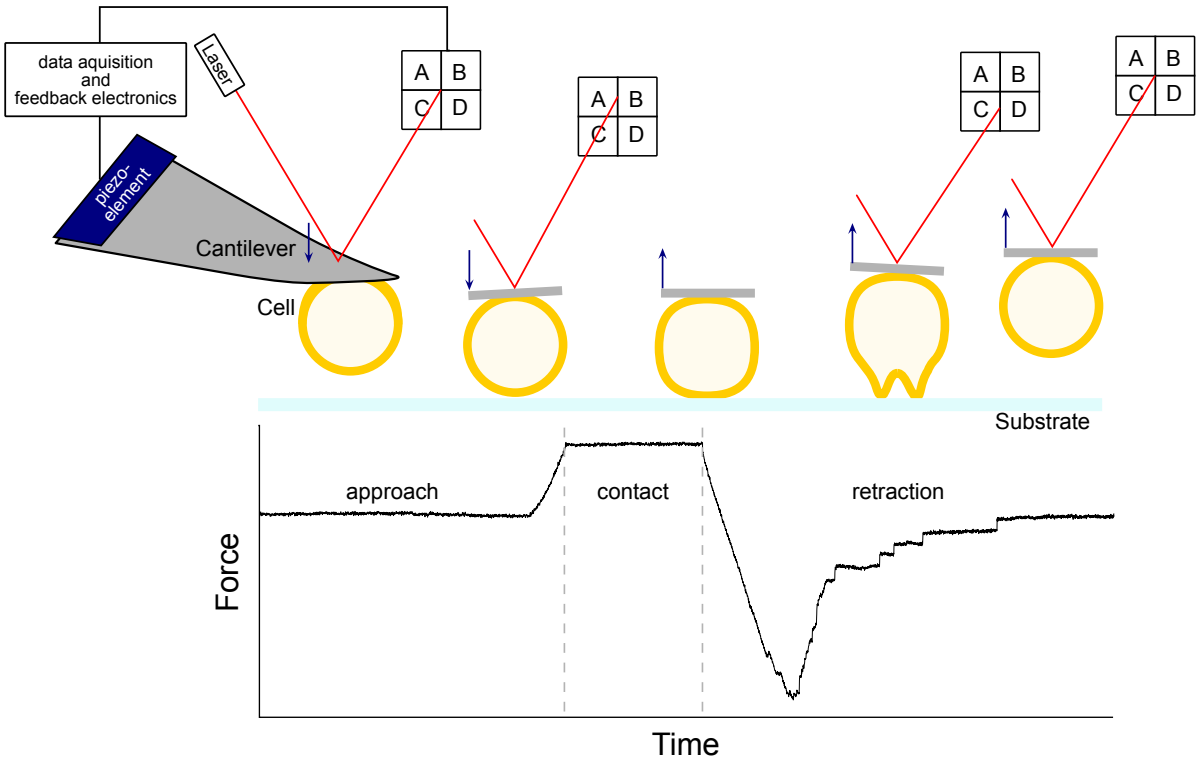

Figure 3.2: Sketch of a AFM-based SCFS cycle - Single cell (yellow) attached to the cantilever (grey), connected to piezo-element (blue) and four-quadrant photodiode (white square). Laser (red) moved on photodiode up and down during measurement cycle. Compression of the cell and membrane changes are illustrated. Force plotted over time during approach, contact time and retraction.

The Asylum MPF-3D Bio (Oxford Instruments, UK), with a 40 μm piezo-controlled z-range to capture the whole detachment process of *D.d.*, was used. Tipless cantilevers (Arrow TL2-50, Nano World, Switzerland), with the following properties were chosen: resonance frequency f_0=6 kHz in liquid and mean spring constant k=0.03 N/m. The cantilever was calibrated before attaching a single cell to the cantilever tip. *D.d.* is very sticky, therefore the immobilization has to be very strong without restricting movement and without being metabolised by *D.d.*. To attach a single cell to the tip of the cantilever, it is common to use Corning® Cell-Tak™ for immobilizing[121, 137], which is a polyphenolic adhesive protein mixture. For this purpose Cell-Tak™ has to be diluted 1:30 with 1 mM $NaCO_3$. For the preparation a cantilever holder out of polytetrafluoroethylene was designed, as shown in figure 3.3, where the cantilever can be placed vertical and the volume for the functionalization is minimized to 100 $\mu l/cantilever$. After an incubation period of 30 min, the cantilever was rinsed with ultra pure H_2O and dried over night. The cell were picked from the substrate by optical feedback (Microscope: IX71, Olympus Japan; objective: 40x LUCPlanFLN, 0.6 Ph2, Japan) as shown in figure 3.4B. After a resting time of 2 min the cell has established a stable adhesion and the experiment can be started (parameters are already established for *D.d.*[121]),

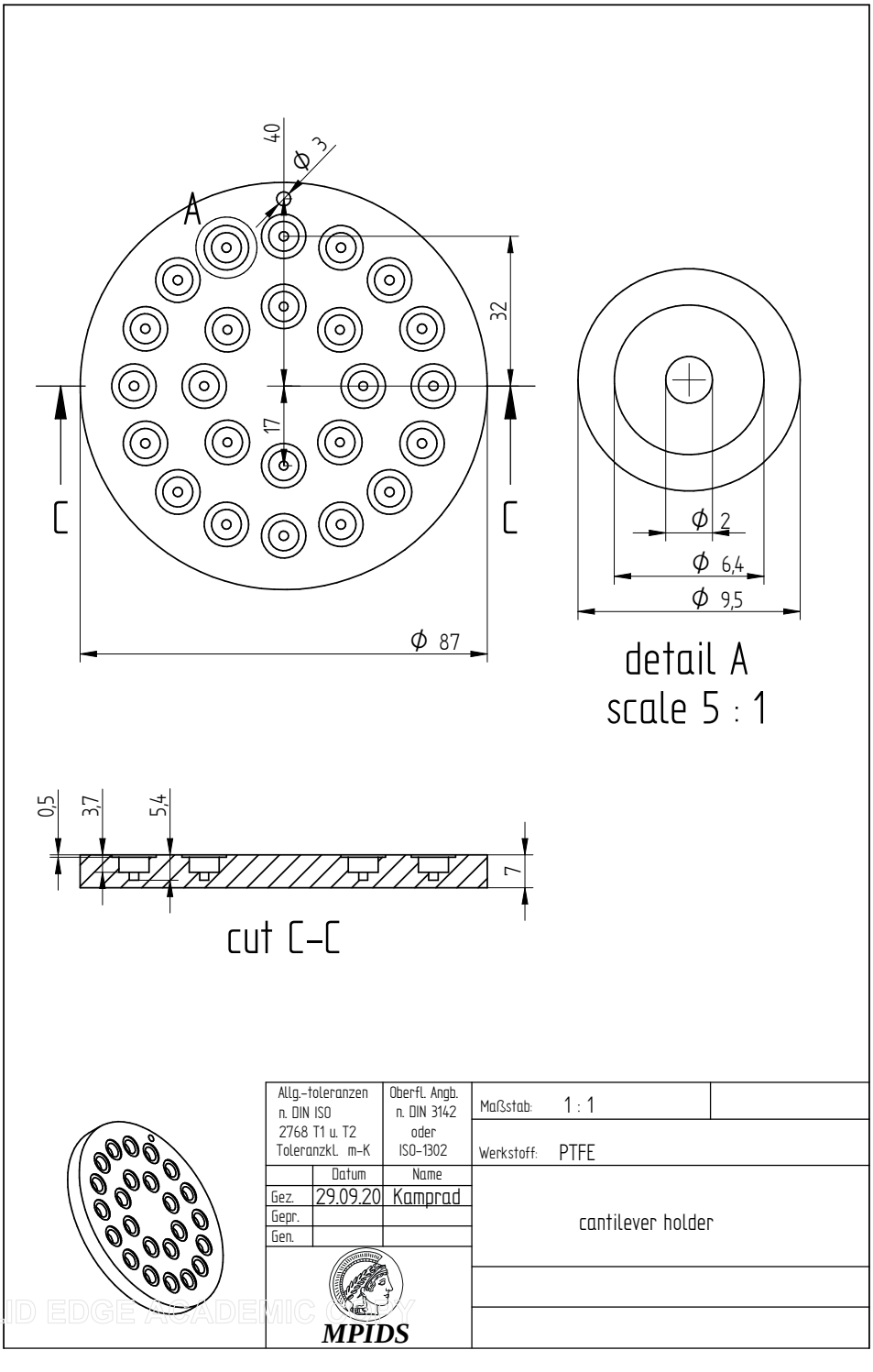

Figure 3.3: technical drawing of a cantilever holder - Holder for 24 Cantilever. Cavities have a volume of 100 μl. Cantilever can be placed vertically.

as shown in figure 3.2. The cantilever moves towards the substrate with a velocity of 2.5 $\mu m/s$ until a constant force of 0.5 nN is reached. After a contact time of 30 s, the cell is retraced with the same speed (2.5 $\mu m/s$). The result is a characteristic force-distance curve (FD). The cycle is repeated up to five times per cell to avoid adaptation, with a regeneration time of 30 s between each cycle.

The retrace of the FD curves were analysed with a custom Matlab script. Typical (global) parameters are the maximal adhesion force (F_{max}, minimum of the FD curve) and the adhesion work (W_{adh}, integral between the baseline and FD curve). Furthermore, vertical jumps within the FD curve, named steps, were analysed. Besides the number of steps per curve (N_{Step}), the step force (F_{Step}), the length between two consecutive steps (l_{Step}), and the complete length until the last step (total detachment of the cell, $l_{Pulling}$) were measured[41]. An overview is shown in figure 3.4A.

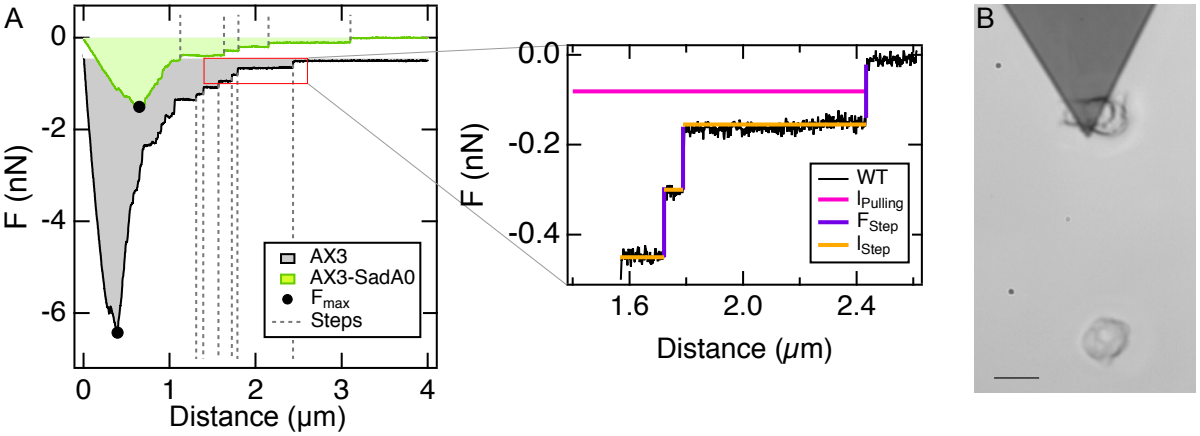

Figure 3.4: AFM-based Single cell force spectroscopy - A: exemplary force-distance curve of AX3 (black, Offset -0.5nN) and SadA0 in AX3 (green) cells. Global parameter like maximum of the adhesion force (F_{max}, black dot), adhesion work (W_{adh}, coloured area of the FD curve) as well as the detected steps (grey doted line) are marked. Zoom-in of the red box shows the step analysis: pulling length ($l_{pulling}$), step length (l_{Step}) and step force (F_{Step}). B: Image (Bright field) of an immobilized cell (AX3-SadA0) in front of a tipless cantilever with a second out-of focus cell on the substrate. Scale bar 5 μm.

For measurements of *D.d.* on uniform PEG-gels: glass substrates (⌀ 35 mm x 1 mm, Soda Lime Float, PG&O, USA) were coated half with PEG-gel, as described in detail in [43]. Both vegetative and developed cells were measured, preferably picked from the glass side to prevent adaptation to PEG. In this study the two axenic *D.d.* strains AX2 and AX4 were used. In addition, GFP-tagged LimE (ΔcoilLimE-GFP) were used in an AX4 background. Furthermore, wildtype AX4 cells were also transformed with GFP-tagged LimE (ΔcoilLimE-GFP) and RFP-tagged coronin (LimE-GFP/corA-RFP)[142].

The following individual transformations were used for the wildtype AX2 cells: GFP-tagged MyoII (MyoII-GFP) or GFP-tagged LimE (ΔcoilLimE-GFP). In addition, wild-type AX2 cells were transformed with GFP-tagged LimE (ΔcoilLimE-GFP) and RFP-tagged αTubulin (LimE-GFP/Tub-RFP). In addition the double transformation GFP-

tagged MyoII and RFP-tagged LimE (MyoII-GFP/LimE-RFP) were used. At least 5 cell and 13 FD curves were measured for each setup.

For the last project, besides vegetative axenic wildtypes (AX2, AX3, DH1), the following knock-outs of key actin binding proteins were used: wildtype AX3 wit SadA deletion, wildtype AX2 with a ScarA deletion, wildtype AX2 with a TalA deletion, wildtype AX2 with a ForA deletion, wildtype DH1 with a TalB deletion, as well as the application of the inhibitor CK666 in AX2 to reduce Arp2/3-mediated actin branching.

Before the measurements could start, cells were seeded in a concentration of $3 \cdot 10^3$ $cells/cm^2$ on glass slides ($\varnothing$ 35 mm x 1 mm, Soda Lime Float, PG&O, USA). After a sedimentation time of 20 min the experiment was started. At least 6 cell and 20 FD curves were measured for each setup.

In addition AFM (CellHesion 200, JPK Instruments, Germany) was combined with a TIRFM (IX81, Olympus, Japan; objective: 10x UPlanFL N/0.30/Ph1, ∞/-/FN26.5 with additional 1.6x magnification, Olympus, Japan; Camera: Orca Flash 2.8 C11440, Hamamatsu, Japan). To reduce bleaching, a delay of 25 s in the start of recording has been incorporated into the recording routine (t_c=190 ms, t_{exp} = 50 ms, 400 images), which will be described in detail in section 3.6.1. The standard AFM-routine was adjusted regarding the retrace velocity, which was set to 0.25 $\mu m/s$. Both systems were started synchronized. For the measurements *D.d.* wildtype AX2 with a GFP-tagged actin binding domain LimE was used.

3.4 Confocal microscopy

3.4.1 Resolution limit by Abbé

The microscopic image of a fluorescent microsphere (figure 3.5A/C) is shown in figure 3.5B/D, the image of the point source is much larger than the original. Beside a central point, diffraction rings of many orders can be observed, which result from the constructive interferences of diffracted light. This effect was described for the first time by Airy[143], which is why it is called Airy pattern. Since light from the point source is scattered by diffraction, this pattern is generally referred to as point-spread function (PSF).

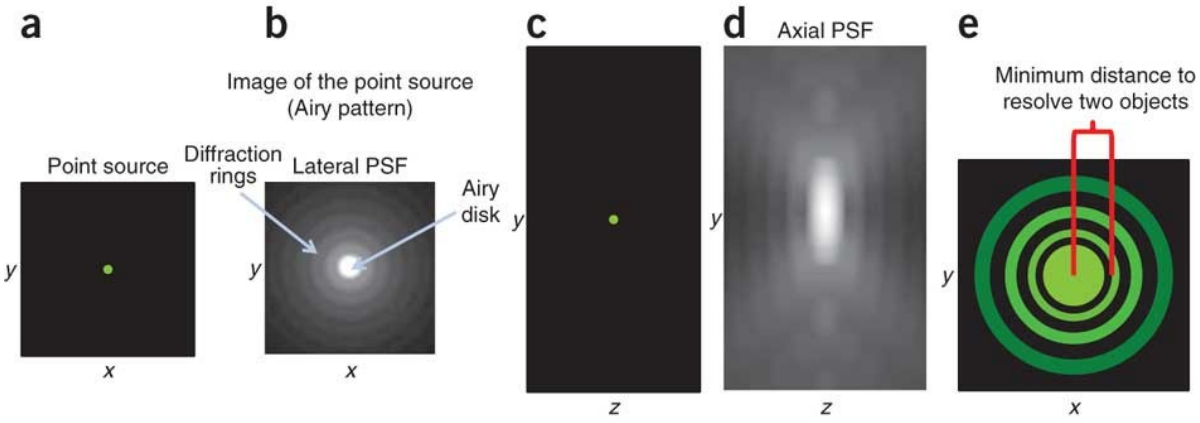

Figure 3.5: Point source in microscopy - Schematic illustration (a-d) of a 100 nm point source in the xy plane (a) and the yz plane (c), as well as the theoretical PSF in the xy plane (b) and the yz plane (d). Details on PSF can be found in [144]. The minimum distance to resolve two objects is shown in red in (e). Printed with the permission of the publisher[144].

Resolution is defined as the ability to distinguish two nearby objects as different objects. Fluorescence microscopy is also limited by the system resolution. Optical resolution has a limit, which is approximately described by equation 3.2. Features beyond this limit simply cannot be resolved, which is known as Abbés diffraction limit

$$\xi \approx \frac{1.22\lambda}{2n\ sin\alpha}, \tag{3.2}$$

where radius of the focal spot ξ, the refractive index n for the liquid between the immersion-lenses and the objective-lenses (of aperture angle, α) is added by the knowledge that the wavelength λ in the medium is scaled by the refractive index (λ/n)[88].

The border was adopted as a rule of nature. As early as the beginning of the 1950s, it could be shown that the resolving power of imaging systems can be extended beyond the diffraction limit by filtering the pupil plane[145]. This idea was further developed with confocal microscopy. There, a laser passes through a pinhole and excites the fluorophores in the sample. The pinhole reduces the out-of-focus signal by blocking non-focal emission light.

This is followed by the development of total internal reflection fluorescence microscopy (figure 2.16B), which will be detailed described in chapter 3.6.1, and Stimulated emission depletion microscopy (STED).

3.4.2 Confocal laser scanning microscopy and the combination with AFM

In conventional microscopy, the entire tissue is simultaneously illuminated with high background noise, which impairs the image quality. In confocal microscopy, the focus is only on a small spot within the tissue, as shown in the subfigure of figure 3.6A, which cannot be smaller than the wavelength of the light itself, about 0.5 μm. With the same lens, the reflected light is projected, unlike in conventional microscopy, and is not viewed directly. Light outside the focal plane (the scattered light) is blocked by a pinhole. Usually a photomultiplier is used to detect the confocal light. This makes it possible to image the sample "point by point", which is time consuming, but provides a good spatial resolution ($\approx 200\ nm$).

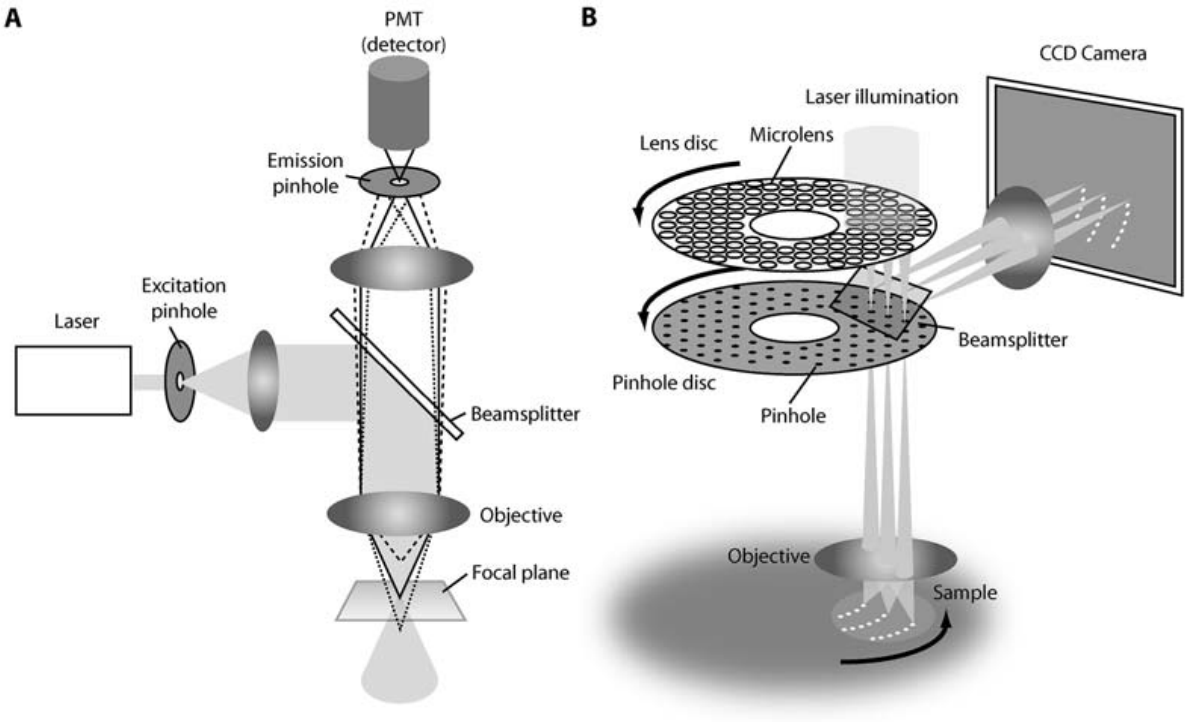

Figure 3.6: Setup of a spinning disk CLSM - A: Schematic drawing of a single beam scanning confocal microscope B: Schematic drawing of a multi-beam scanning confocal microscope (Yokogawa CSU 10). Printed with the permission of the publisher[146].

To visualize the *D.d.* cell shape during force-clamp experiments, AFM was combined with Confocal Laser Scanning Microscope (CLSM: IX83 with FV1200, Olympus, Japan; Camera: XM10, Olympus, Japan; objective: 60x/1.35O ∞/0.17/FM26.5, Olympus,

Japan). To detect the cell contour, AX2 with GFP tagged carA-1 was used, which is a major cAMP receptor within the cell membrane and already present in vegetative cells[147]. In this case, the SCFS routine was slightly modified and a force clamp mode was used to gradually detach the cell from the surface (0.2 nN, 2.5 $\mu m/s$, 50 s). Optical reconstruction of the 3D-stacked cell during force-clamp was done with *Imaris* (Bitplane, Switzerland) and the data analysis with *ImageJ*.

3.4.3 Cell flatness via spinning disk confocal laser scanning microscopy

The basic principle of a spinning disk confocal laser scanning microscope (SDclsm) is that of a classical confocal laser scanning microscope, as described in the section before. Instead of a single pinhole, a whole disc with pinholes is used, as shown in figure 3.6B. The Yokogawa CSU-X uses a second disc in addition, where microlenses are placed. As the discs rotate synchronized, an array of focused laser beams scans the sample, which increases the temporal resolution. In addition bleaching is lower. Instead of a photomultiplier, a CCD camera is used, which reduces the spatial resolution ($\approx 400\ nm$) compared to the classic confocal microscope.

To measure the flatness of a cell the entire cell body volume has to be visualized. For this purpose the cytoplasm of AX2 was GFP-tagged with HG1694, which labels free GFP in the cytoplasm of the cell[148]. In the case of AX3, the cell cortex was visualized with GFP-tagged LimE. Cells were seeded in a concentration of $3 \cdot 10^3\ cells/cm^2$ on the model substrates. After a sedimentation time of 30 min, a spinning disk confocal microscope (SD; Microscope: IX83, Olympus, Japan; SD-Unit: CSU-X1, Yokogawa, Japan; Camera: iXon Ultra EMCCD dual cam setup, Andor, UK; Objective: 100x LUMPlanFI/1.00w, $\infty/0$, Olympus, Japan) was used, to visualize the entire cell body, by piezo-driven z-stack, set to 0.5 μm step size. The cell contour was captured with a custom Matlab code.

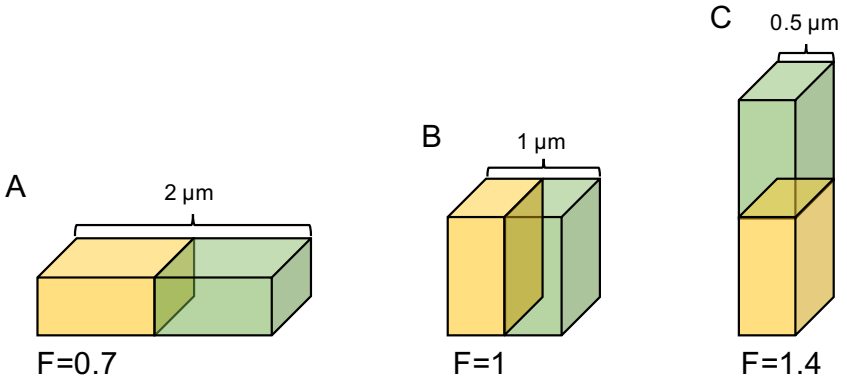

Figure 3.7: Characterisation of the spreading behaviour by the flatness factor F - If the $\sqrt{contact\ area}$ and $\sqrt[3]{volume}$ is equal to one, $F = 1$. If the volume remains the same and the contact area doubles, $F < 1$. If the contact area halves, with the same volume, $F > 1$.

The flatness factor F, was calculated as the square root of the contact area over the cube root of the voxel volume of the whole object[149](figure 3.7),

$$F = \frac{\sqrt{contact\ area}}{\sqrt[3]{volume}}. \tag{3.3}$$

3.5 Relative cell contact area via reflection interference contrast microscopy

To visualize the membrane height on the ventral side of the cell, it is possible to use reflection interference contrast microscopy (RICM). This setup is perfectly suited for investigating the label-free dynamics of adhesion in aqueous solution up to 200 nm distance from the surface. It can be easily inserted into a commercially available inverted microscope (IX83+, Olympus, Japan) with a halogen lamp (560 nm, MT-20 Light Source/Filter Wheel, Olympus), as it mainly required the lambda quarter plate and a set of polarisator/analysator. The result of the measurement is a 2D matrix of intensity, which can be converted to the corresponding substrate-object distance based on the multiple interfaces with different refractive indices interfering. The detailed light path is shown in figure 3.8A. The interface of the sample reflects the light (figure 3.8B) based on the differences in the refractive index n.

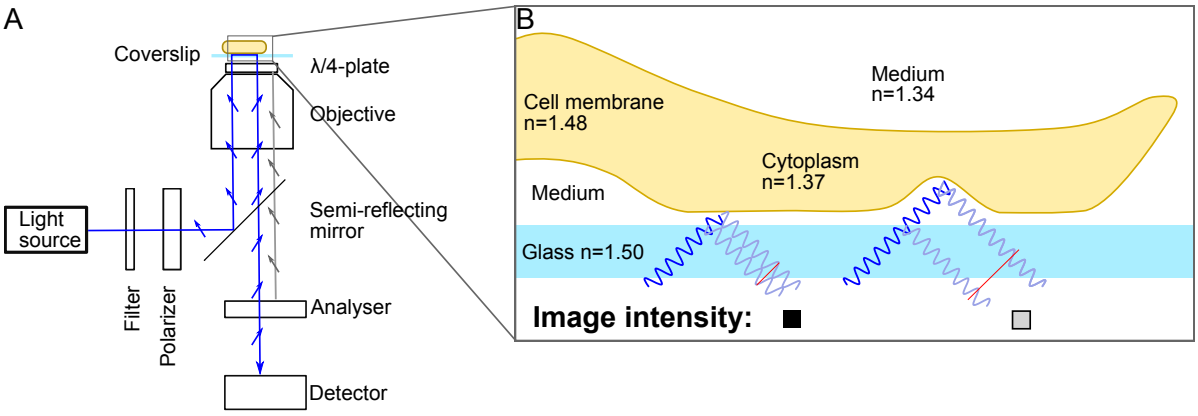

Figure 3.8: Setup of reflection interference contrast microscopy - A: Setup of RICM. Monochromatic light is released from the filter, becomes polarized and will be reflected by the mirror. Light has to pass the $\lambda/4$-plate, becomes circular polarized and crosses afterwards the objective to hit the multilayered object, where it reflected several times and interference occurs. Reflected light is circular polarized in the opposite handedness from the incoming beam. After passing to the $\lambda/4$-plate again, the light is linear polarized with an orientation of 90°. Stray light (grey) cannot pass the analyser. B: Zoom-in to a single cell on a coverslip. Refractive indices (n) of the different media are shown. Phase shift of the reflected light at the cell membrane to the interface of the coverslip is shown in red. Objected further away from the coverslip show reduced intensity.

Differences in membrane height shift the signal and reduce the effect of interference. This become visible in a reduction of signal intensity.

For the experiment, cells in a concentration of $3 \cdot 10^3$ $cells/cm^2$ were placed on glass bottom μ-Dish. After a sedimentation time of 20 min the experiment started. First, a RICM image was recorded, afterwards the z-piezo moved the objective $\approx$3.7 μm into the central cellular area to take the bright field image. RICM shows the contact area of the cell, which was tracked with *ImageJ* (background subtraction, adjust threshold). The projected bright field area was manually tracked, also using *ImageJ*. The relative contact area is calculated as the quotient of contact area to projected bright field area[150, 151], as shown at the bottom of figure 3.9. At least 20 cells per category were measured.

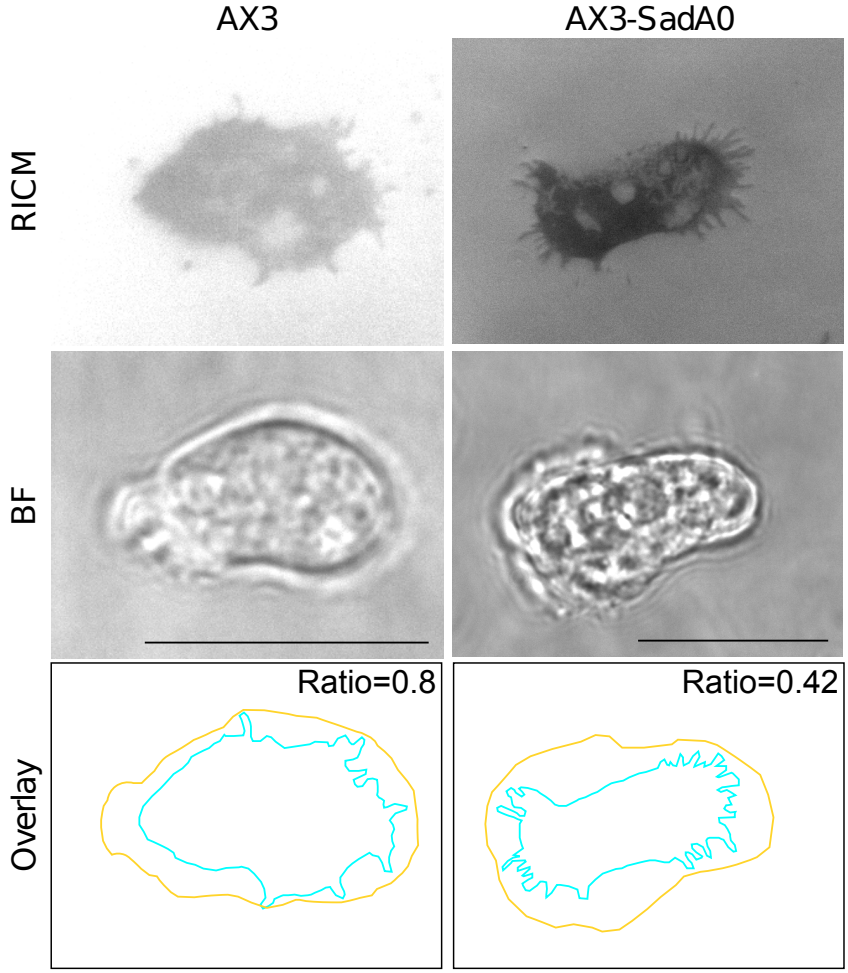

Figure 3.9: Evaluation of the adhesion with reflection interference contrast microscopy - Contact area (by RICM) and projected bright field area of wildtype AX3 compared to SadA0. Scale bar 13.5 μm. Additional overlay of contact area (cyan) and projected bright field area (yellow), with the corresponding ratio (quotient of contact area and projected bright field area).

3.6 Actin foci studies by total internal reflection fluorescence microscopy

3.6.1 Total internal reflection fluorescence microscopy

To analyse fluorescent fusion protein dynamics at the ventral side of the cell, Total internal reflection fluorescence microscopy (TIRFM; Microscope: IX83+ cellTIRF-4Line, Olympus, Japan) was used. Instead of illuminating the entire cell, only the lower 250 nm (starting from the coverslip) are illuminated, as shown in figure 2.16B. The advantage of the method is that the signal-to-noise ratio is improved. This is possible by overcoming the diffraction limit. Instead of directing the laser directly to the sample, as is usual with epifluorescence and creating the typical point spread function, the laser is guided to the slide at an total reflection angle θ, as shown in figure 3.10.

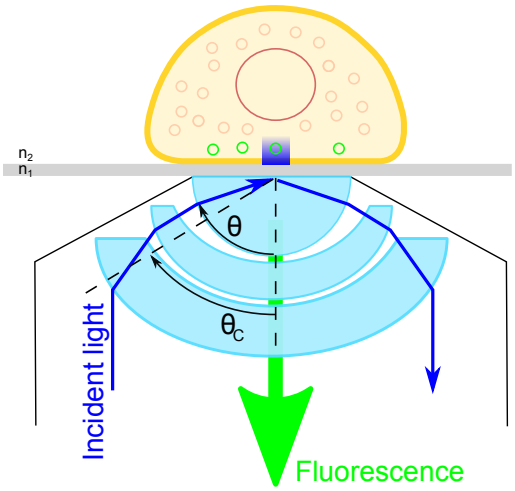

Figure 3.10: Total internal reflection fluorescence microscopy setup - Incident light (blue) will be broken by several lenses. The light reflects at the coverslip (grey) in an angle θ, which is bigger then the critical angle θ_c. Total reflection sends the light back. At the interface of the coverslip an evanescent field appears. The laser intensity decreases exponentially with the penetration depth, given in equation 3.4. Fluorescence proteins near the surface (< 250 nm) can be illuminated (green) and detected, while more remote ones in the bulk (pink) cannot, thus increasing the signal-to-noise ratio.

The following additional conditions have to be fulfilled to use the effect of total reflection, e.g. creation of a standing wave at the interface between sample and substrate. The two media must have different refractive indices n. Medium 1 is the coverslip, as shown in table 3.3, n_1=1.523. Medium 2 is the biological sample, where the refractive index can only be estimated, $n_2 \approx 1.3$[152]. They behave as follows: I) $n_1 > n_2$ II) θ has to be larger than the critical angle θ_c, which be calculated by $sin(\theta_c) = n_2/n_1$. Fresnel's equations show that in the case of total internal reflection, the light is totally reflected. An electrical component of light that crosses the boundary creates a evanescent field in

the second medium, which decreases exponentially with the perpendicular distance from the interface:

$$I = I_0 e^{-z/d}, \tag{3.4}$$

where I is the field intensity at the distance z (near the surface), d is the decay constant of the field and I_0 the intensity at the interface (z=0). An evanescent wave is usually most intense within a third of its wavelength[152]. This kind of light source can be used to illuminate fluorescence proteins inside the cell, as shown in figure 2.16B.

Table 3.3: Substrate properties of ibidi μ-Dish^{35mm,high} Glass Bottom[153].

Refractive index	1.523
Diameter dish	35 mm
Bottom	Glass coverslip No. 1.5H, $170 \pm 5\mu m$
Material	Schott borosilicate glass, D 263M

The main components of the setup are two of three laser beams (*cell, CMR-LAS, 150 mW) with 488 nm and 561 nm wavelength to illuminate fluorescent proteins emitting green (GFP) and red (RFP). In addition, a special objective (100x UApo N, 1.49 Oil, Olympus, Japan) is required to focus the light on the back of the objective and diffract it to create TIRF-conditions ($\theta \leq \theta_c$), as shown in figure 3.10. A petri dish with glass bottom (μ-Dish, Ibidi, Germany) has to be used. The substrate properties of the μ-Dish are shown in table 3.3. The light is collected by the same objective and directed to the camera (ORCA-Flash4.0, 65 nm/px, Hamamatsu, Japan).

3.6.2 Experimental procedure for TIRFM

Cells were seeded on a μ-Dish in a concentration of $3 \cdot 10^3$ $cells/cm^2$. After a sedimentation time of 20 min the experiment was started. To get a very high temporal resolution short term ($\mathcal{S}$, figure 3.11) experiments were done. Data acquisition of $\mathcal{S}$-experiments was done with a cycle time (t_c) of 150 ms between each frame and an exposure time (t_{exp}) of 50 ms. 400 frames were recorded within a minute.

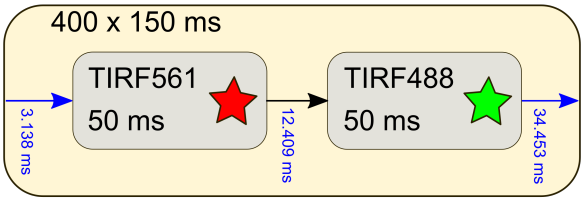

Figure 3.11: Experimental setup of short ($\mathcal{S}$)-experiments conditions - Within a cycle one TIRFM images with a laser of 561 nm was illuminated for 50 ms, after 12.409 ms a further TIRFM images with a laser of 488 nm was illuminated for 50 ms. After 34.453 ms the cycle was repeated. Within 1 minute, 400 images of every channel were created.

Therefore LimE and LimEΔcoil was characterised with a mRFPmars-tag in *D.d.* wildtype AX2. In addition GFP-tagged LimE in AX2 were analysed with the $\mathcal{S}$ procedure. Details of the experiment are shown in table 3.4.

Table 3.4: Overview of used actin label and fluorescence proteins (FP) - All measurements were done in WT AX2 in $\mathcal{S}$-term experiments. Number of measured cells is named.

Actin label	Vector name	FP	WT	Procedure	# cells
LimE	pAL16 pDM115	mRFPmars	AX2	$\mathcal{S}$	18
LimEΔcoil	LimEdcoil(340-12)	mRFPmars	AX2	$\mathcal{S}$	18
LimE	127-45 pDEXH(B12)	GFP	AX2	$\mathcal{S}$	20

These characterization of actin foci (LimE-GFP) was also performed for *D.d.* cells with ABPs, where adhesion mediator proteins were deleted. In addition the influence of the wildtype on actin foci distribution was analysed. Mainly long term experiments ($\mathcal{L}$) were done, with t_c=450 ms and t_{exp}=150 ms. 400 frames were recorded within three minutes. All experimental conditions are shown in table 3.5.

Table 3.5: Overview of used cells for actin foci studies with LimE-GFP - Wildtype and corresponding k.o. for measurements with LimE-GFP. In addition the kind of experiments and the number of measured cells is named.

WT	k.o.	Experiment	# cells
AX2		$\mathcal{L}$	16
	TalA0	$\mathcal{L}$	19
	ForA0	$\mathcal{L}$	20
AX3		$\mathcal{S}$	24
	SadA0	$\mathcal{S}$	19
Ref.DH1		$\mathcal{S}$	20
	TalB0	$\mathcal{L}$	35

To reduce branching of actin filaments, the inhibitor CK666 was used in AX2 with GFP-tagged LimE to visualize actin (22 cells measured). *D.d.* possesses several formins. Within this work, the Mouse Diaphanous (mDia1)-like formin A (ForA) was knocked out (ForA0), which is known to be involved in the actin cortex organisation at the rear of *D.d.* migrating cells[37]. In case of DH1 TalB0 rescued by TalB0 GFP-tagged TaB together with mRFPmars-tagged LimE was used as a reference for DH1, which is named Ref.DH1.

In addition co-localization studies of actin (LimEdcoil(340-12)) and clathrin (ClcA-GFP) where done in $\mathcal{L}$- (figure 3.12, 29 cells measured) experiments configurations.

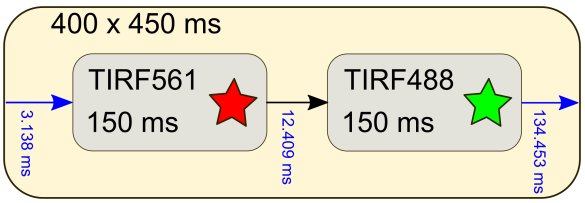

Figure 3.12: Experimental setup of long ($\mathcal{L}$)-experiments conditions - Within a cycle one TIRFM images with a laser of 561 nm was illuminated for 150 ms, after 12.409 ms a further TIRFM images with a laser of 488 nm was illuminated for 150 ms. After 134.453 ms the cycle was repeated. Within 3 minute, 400 images of every channel were created.

3.6.3 Data analysis of TIRFM experiments

Images generated by TIRFM were analysed with a custom *Matlab* code, based on [105]. The images of the timeseries (3.13A) were binary thresholded by K-means clustering[154], which groups the image into three classes. One is the background and the rest is defined as foreground (cell including foci), as shown in figure 3.13B.

In addition, newly appearing foci were isolated by a second segmentation step, as shown in figure 3.13C/D. Therefore foci were highlighted, the background of the cell was smoothed and divided by the whole cell. To filter the noise the following parameters were added: I) Objects smaller than 10 px and darker than 1.5 times (value can vary from 1.2 to 1.9 depending on the cell type and experimental setup) the background were removed. II) Objects had to remain in focus for at least 3 s to be considered for the analysis. All added filtering effects can be seen in figure 3.13E/F.

In a next step the foci were isolated and analysed separately. A summary is shown in figure 6.4. To analyse the signal, the background had to be subtracted and the signal intensity normalized (mean of the background signal was set to zero and the maximum of the signal to one). Furthermore, the time point (t_{max}) at I_{max} was set to zero. At I_{50} t_{before} and t_{after} were determined. The lifetime at half intensity (lt_{50}) is calculated from the sum of $|t_{before}|$ and t_{after}, as shown in figure 3.15.

For co-localization studies the second (green) channel was processed in the same way. In addition, a signal-to-noise analysis was performed to verify the quality signal of the second channel, as shown in figure 3.14. Therefore the standard deviation of both the signal and the noise was calculated. A qualitative signal has to have signal-to-noise ratio higher two. The results were used to calculate the coincidence of both signals. The time points t_{before}, t_{max} and t_{after} were determined and the timeshifts (dt) to the corresponding LimE-signal were calculated. A summary of the analysed parameter is shown in figure 3.15.

For distribution analysis of actin foci, the cells were tracked as described before. Parameters such as the number of foci per min (N_{foci}), the lifetime (lt_{50}), the positional shift of the focus ($l_d(lt_{50})$) as well as the velocity ($V_f = l_d/lt_{50}$), were determined. In addition the distance of the nearest neighbour/focus (nn) of all foci within the image stack was calculated. Blinking foci were removed.

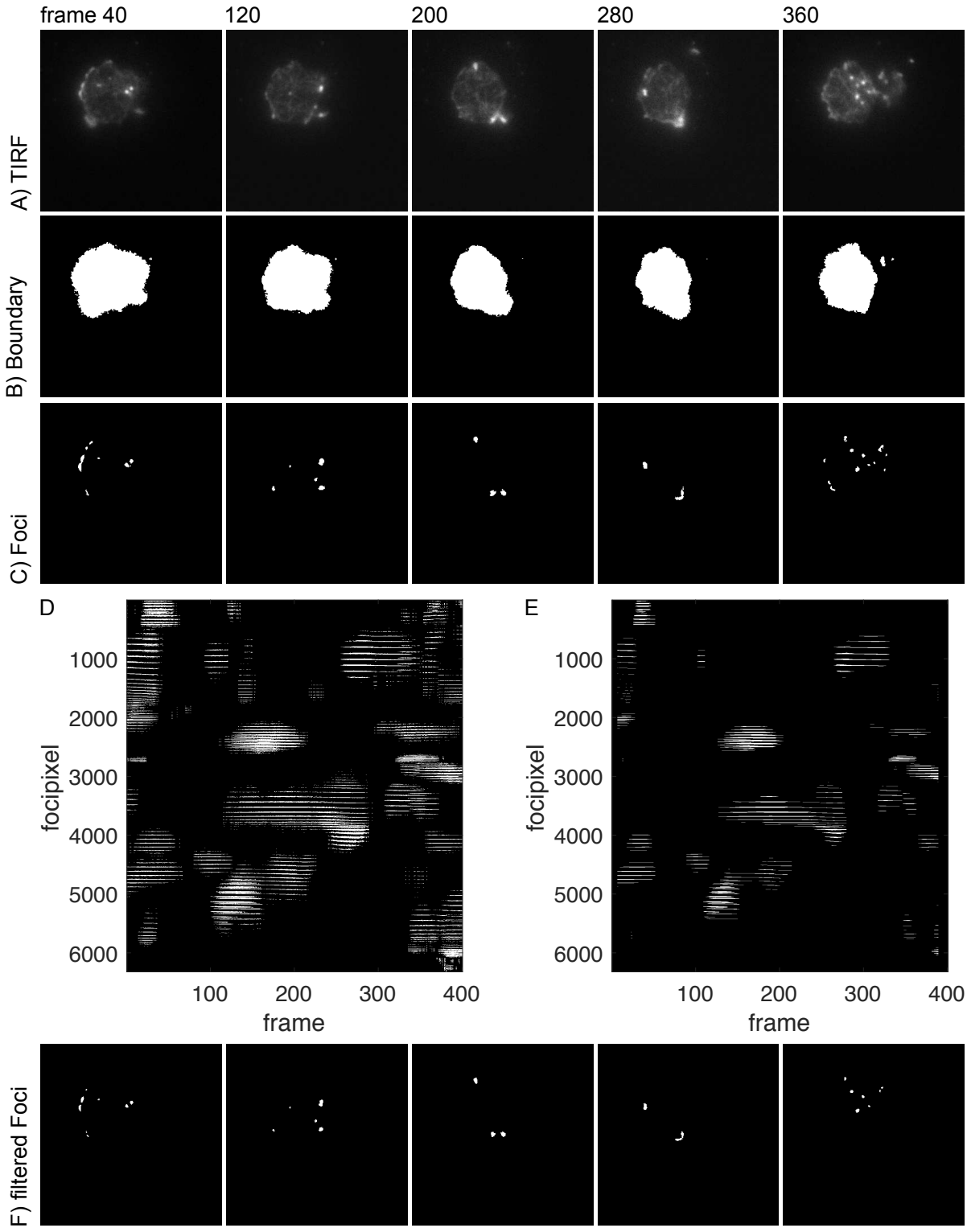

Figure 3.13: Procedure of TIRFM analysis - Exemplary AX3 cell with GFP-tagged LimE of an $\mathcal{S}$-experiment, frame number 40, 120, 200, 280 and 360 are shown. Image size 322x322 px (21x21 μm) A: TIRFM image of the cell. B: Tracked cell is shown in white. C: Tracked foci are shown in white. D: Pixel of the tracked foci (C) are show over the whole observation time of 400 frames. E: Pixel of the tracked foci after adding the filter criteria over the whole observation time of 400 frames. F: Foci after filtering at the five exemplary time points.

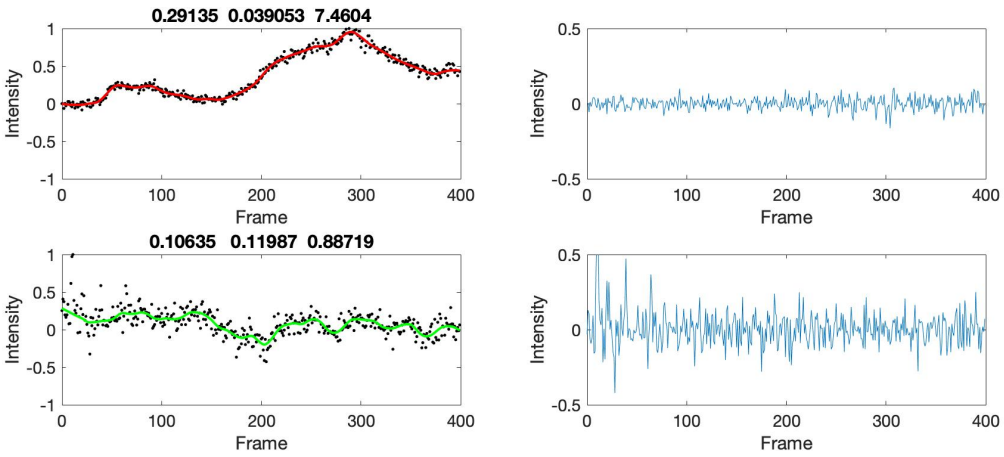

Figure 3.14: Characterisation of the signal - Analysis of the signal-to-noise ratio from co-localization studies. Exemplary tracking of AX2 with mRFPmars-tagged LimEΔcoil (top row) and GFP-tagged ClcA (bottom row) in an $\mathcal{S}$-experiment. Signal-to-noise studies check the signal quality. Standard deviation of the actin (0.29) and clathrin (0.10) signal as well as the noise of the actin (0.04) and clathrin (0.12) signal were calculated. A qualitative signal has to have a signal-to-noise ratio higher two, in the shown example the actin-signal has a SNR of 7.5 and the Clathrin-signal of 0.9, which would be analysed. The noise is shown in blue.

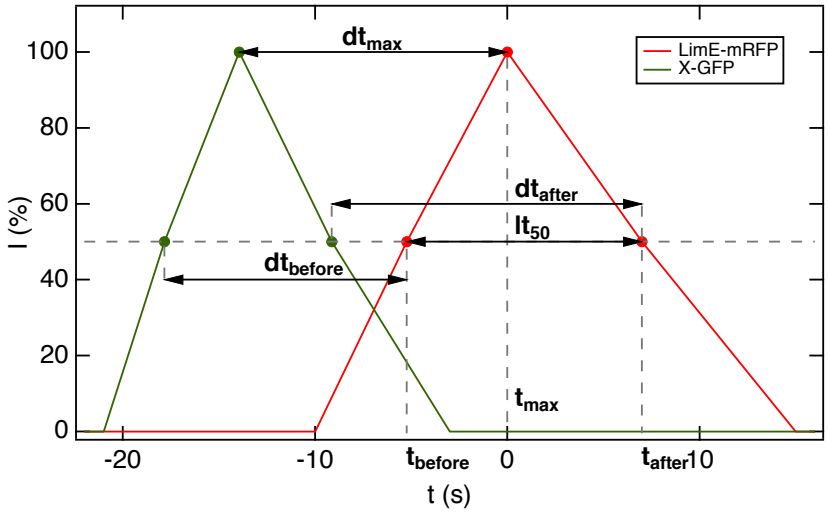

Figure 3.15: Sketch of the analysis of the intensity profile from TIRFM measurements - The maximum of the LimE signal (I=100) was set to zero (t_{max}). At I=50 t_{before} and t_{after} were calculated. The lifetime at half intensity (lt_{50}) is the sum of $|t_{before}|$ and t_{after}. For the co-localization studies the timeshift (dt) between the channels was calculated at the three main points (dt_{before}, dt_{max}, dt_{after}).

As key actin binding proteins influence actin pattern, quantification of the distribution of actin foci needs a reference system. In comparison to migrating cells, vegetative cells have neither a clear directionality nor polarity, which makes it impossible to segment the cell contour with left/right and front/rear. Therefore, the centre of mass (COM) for the time point (t_n) when a focus (F_n) appears and the focus distance (l_n) to the COM could be calculated. Furthermore, the minimum distance to the boundary was determined (R_{max}), which corresponds to the radius of the largest cell-centred circle. R_{max} was used to normalize l_n in an area-independent manner, so called l_{norm}.

To validate the software the Fiji Plugin *Manual Tracing* was used for exemplary cells of each category. The time point and position of the appearing and disappearing foci was tracked manually. The number of foci, the lifetime (lt) of each focus as well as the positional shift (l_d) and velocity (V_f) could be analysed. The whole set of TalB0 cells were only tracked manually.

3.7 Statistics analysis

For the statistical evaluation a two sample test routine was created in Matlab, which analyses the distribution of the data. In general Wilcoxon rank sum test was recommended. [*] refers to a p-value of <0.1, [**] p <0.05, and [***] for p <0.01.

Visualization occurred mainly in form of box plots. The box shows 50% of the data. The edge of the box shows the quartiles: value where $\leq$ 25% respectively $\leq$ 75% of the data are located. The black line inside the box, median, divides the box at the value where $\leq$ 50% of the data are located. A whisker is attached to each side of the box and ends where $\leq$ 9% respectively $\leq$ 91% of the data are located, outliers are not shown. In addition, all data points without outliers are shown as coloured dots.

Additionally, violin plots were used, which show the data as dots and the Gaussian kernel density distribution as a black line (Bandwidth Method: Silverman).

The Gaussian kernel density estimation (kde) was used for the polar plots, too. The bandwidth is determined purely data driven by the *MATLAB* program kde [155] using the data. The resulting probability density function (PDF) is given by the sum of the individual kernels.

4 Cell-substrate adhesion of *D.d.* on micro-patterns depends on axenic strain, developmental state and fluorescent markers

Dictyostelium discoideum (*D.d.*) is a social amoeba living in the soil feeding on bacteria. *D.d.* as well as neutrophils follow the chemical gradient of the chemoattractant folic acid secreted by the bacteria to hunt them efficiently, a process known as chemotaxis. In contrast to neutrophils, the habitat of *D.d.* is very heterogeneous and its adhesion principle is very unspecific, so that *D.d.* adheres to almost all surfaces. To study adhesion and directional movement of *D.d.*, the freedom of movement must be restricted. High molecular polyethylene glycol (PEG) gel strips were analysed to determine whether it is one of the substances limiting adhesion and thus migration of *D.d.*. Karmakar [43] could show that uniform developed *D.d.* wildtype AX2 cells are able to move to a cAMP filled pipette on PEG gels (figure 4.1 left:A) at a similar speed ($14\pm3\ \mu m/s$) as developed AX2 wildtype cells on glass. This could not be confirmed for AX4 (figure 4.1 left:B). These experiments were repeated on narrow striped (10 or 25 μm width) glass substrates with

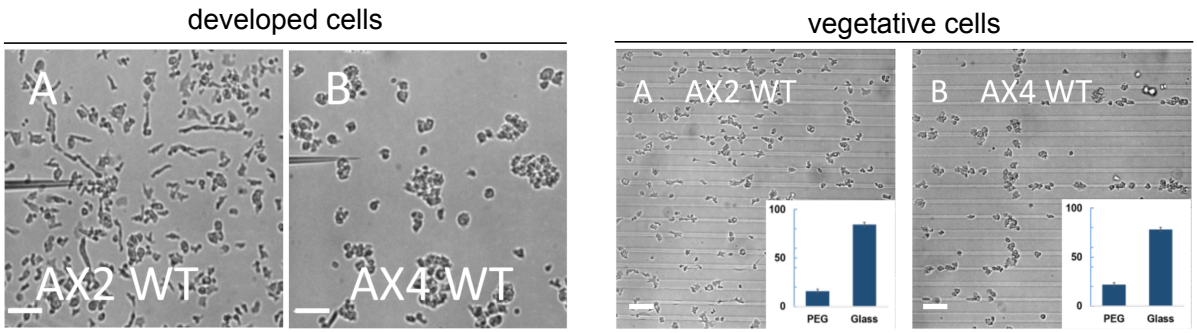

Figure 4.1: *D.d.* in different developmental stages on PEG - Left: Developed WT cells on a uniform PEG-gel surface. Micrographs of AX2 (A) and AX4 (B) exposed to a gradient of chemoattractant cAMP leaking from a pipette. AX2 cells adhere to the surface and migrate toward the leaky pipette, while the AX4 cells remain in clumps and cannot migrate (scale bar: 50 μm). Right: Vegetative cells on micro-patterned substrates- Micrographs of WT AX2 (A) and AX4 (B) cells, 10 *min* after plating. Insets: relative coverage of cells on PEG-gel and glass stripes. For both strains, there is a major bias towards the adhesion to glass vs. PEG-gel. (scale bar: 50 μm). Images from [43] and slightly modified.

intermediary stripes made of PEG (height 1.5 μm). With this new technique of micro patterning, the proportion of PEG and glass adherent developed cells could be quantified in terms of area coverage. Furthermore, vegetative cells on striped substrates were also assessed optically. It could be shown that vegetative AX4 cell are able to adhere and migrate on PEG gel (figure 4.1 right:A). Vegetative AX2 cells show similar properties (figure 4.1 right:B). Karmakar et al.[43] could thus show that the cell migration and adhesion properties of *D.d.* cells can be influenced by PEG, but found that the axenic strain or certain fluorescent labels influence this behaviour.

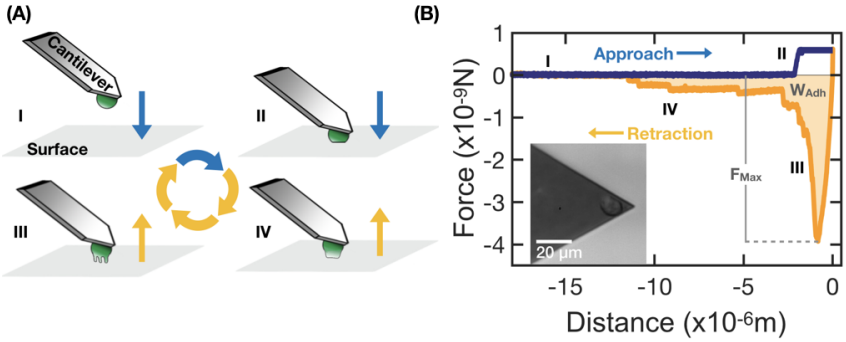

Figure 4.2: Schematic setup for Single Cell Force Spectroscopy (SCFS) - A) SCFS measurement with repetitive cycle of approach and retraction of a cantilever-attached *D.d.* (Inset of B) cell to a substrate of choice, resulting in force-distance (FD) curves (B). These FD curves can be used to determine F_{max} and W_{adh}. For further details, see Material & Methods.[43]

Therefore, as shown in the following chapter, adhesion was quantified. In addition to the micro-pattern assay, AFM-based single cell force spectroscopy (SCFS) measurements were performed. There, all three aspects are considered mainly for vegetative cells, which are also published as part of [43]. Cell detachment experiments (figure 4.2A) with resulting force-distance (FD) curves were determined and the following parameter from the retraction part analysed: maximal adhesion force (F_{max}) and adhesion work (W_{adh}), as highlighted in figure 4.2B.

4.1 Influence of the axenic strain

SCFS measurements on developed and vegetative wildtype AX2 and AX4 were performed on both glass and PEG gels. At least 18 cells with 98 curves were measured for each setup. As an example, force-distance curves from the vegetative case are shown in figure 4.3. The cells were always picked from the glass substrate to avoid adaptation to the PEG. The following values refer to the median.

The results of the maximum adhesion force for developed cells are shown in figure 4.4. F_{max} of *D.d.* wildtype AX2 show no significant differences on glass and PEG (Glass: 1.6 nN; PEG: 0.5 nN), in contrast to the wildtype AX4 (Glass: 3.6 nN; PEG: 0.3 nN).

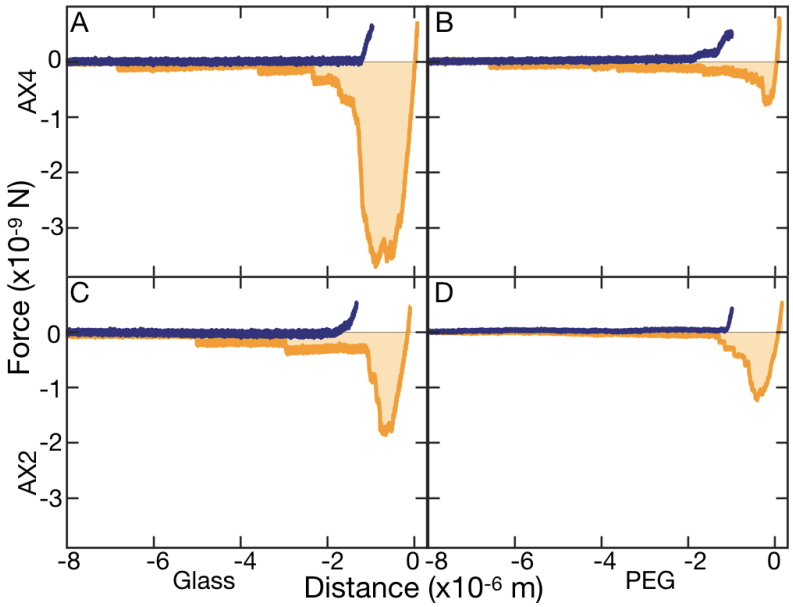

Figure 4.3: Representative Force-Distance (FD) curves from SCFS experiments - on vegetative AX2 and AX4 cells on glass (A) and PEG-gel (B) surfaces. Approach is shown in blue and retraction in orange. Image from [43].

Developed WT AX4 cells show a significantly (p <0.001) higher F_{max} on glass than AX2.

The results of the SCFS experiments with vegetative WT cells are shown in figure 4.5. Vegetative AX2 cells show an F_{max} of 3 nN on glass, which is significantly (p <0.001) higher than in developed cells, but shows a significant (p <0.001) reduction on PEG (0.2 nN). Vegetative AX4 cells show a similar but less significant effect (Glass: 2.1 nN; PEG: 1.4 nN; p=0.006). Thus the different behaviour regarding PEG vs glass between the axenic wildtypes is only detectable for the developed cells.

Furthermore, the F_{max} of vegetative to developed cells is reduced on glass and for AX4 increased on PEG. The results of the SCFS assay agree with the results of the bulk assay of vegetative cells on micro-patterned substrates, as shown in figure 4.1.

Adhesion work (W_{adh}) of vegetative *D.d.*, as shown in figure 4.6 shows a slightly different trend than the adhesion force for vegetative cells. AX2 has a W_{adh} of 4.0 fJ on glass, which decreases significantly (p <0.001) on PEG (0.4 fJ). AX4 however show no significant (p=0.187) differences between W_{adh} on PEG (1.3 fJ) and glass (1.3 fJ). This hints at a compensation for the reduced F_{max}, which could be the increase in step numbers.

In summary, the adhesion force from SCFS experiments show strong similarities to the results of the bulk assay, in contrast to the adhesion work, especially with AX4.

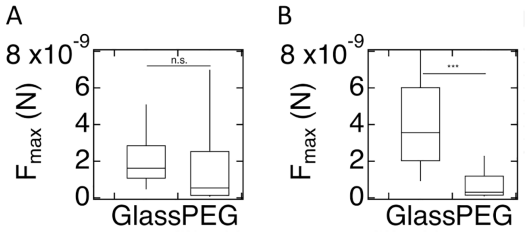

Figure 4.4: Maximum adhesion force for developed cells - F_{max} for AX2 (A) and AX4 (B) cells on glass and PEG-gel surfaces. Image from [43].

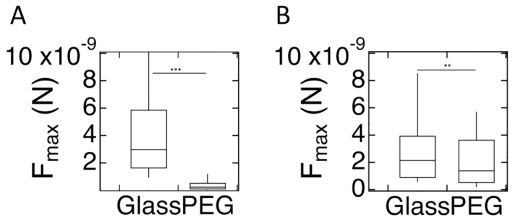

Figure 4.5: Maximal adhesion force for vegetative WT cells - F_{max} for AX2 (A) and AX4 (B) cells on glass and PEG-gel surfaces. Image from [43].

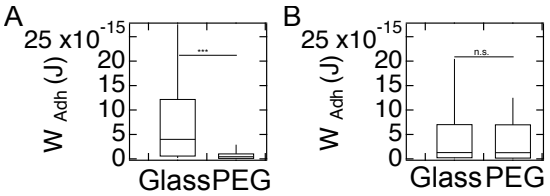

Figure 4.6: Adhesion work for vegetative WT cells - W_{adh} for AX2 (A) and AX4 (B) cells on glass and PEG-gel surfaces. Image from [43].

4.2 Influence of fluorescent markers

With fluorescent cytoskeleton markers it is possible to measure dynamics of cellular proteins of interest, for example to determine the front and back of the migrating cells in micro-patterns. The actin binding domain (ABD) LimE can be used to visualise protrusions on the front of the cell, so-called pseudopodia. Myosin II (MyoII) is suitable to observe myosin-based retraction at the back of the cell, but also lateral pseudopod activity upon splitting. Coronin (Cor) has two different functions at the front and back of the cell. At the leading edge, coronin can promote the growth of actin filaments and inhibit de-polymerisation. In the rear part of the cell, coronin allows cofilin to be recruited to break down actin filaments[156].

These three cytoskeletal markers were genetically fused with fluorophores (GFP or RFP). Both single- and double-labelled cells have been prepared. Therefore the wild-

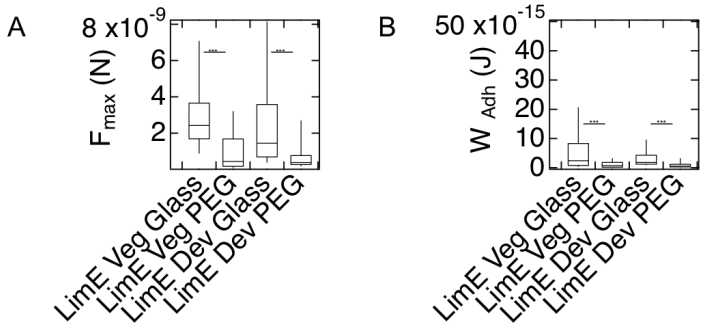

Figure 4.7: SCFS parameter of AX4 with an actin label - F_{max} (A) and W_{adh} (B) for vegetative and developed fluorescently labelled AX4 cells on glass and PEG. Image from [43] and slightly modified.

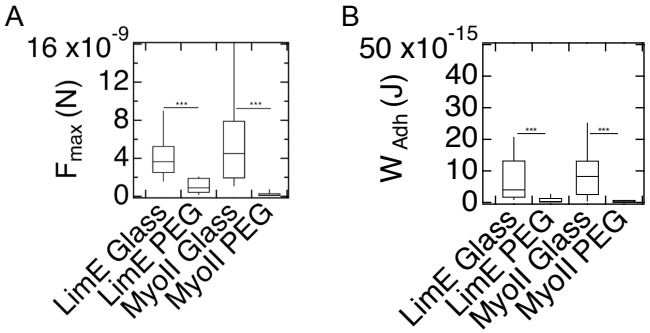

Figure 4.8: Adhesion properties for vegetative AX2 cells with cytoskeletal single labelling - F_{max} (A) and W_{adh} (B) for vegetative AX2 expressing LimE-GFP or MyoII-GFP on glass and PEG. Image from [43] and slightly modified.

types AX2 and AX4 were used. At least 5 cells with 11 curves were measured with each setup.

The ABD of AX4 was labelled with LimE, as shown in figure 4.7A. In all cases the adhesion force of glass to PEG decreases significantly. Only developed AX4 cells on glass labelled with LimE increase the adhesive strength on glass compared to the wildtype (veg.AX4: 2.1 nN, veg.AX4 with LimE: 2.4 nN, p=0.18; dev.AX4: 3.6 nN, dev.AX4 with LimE: 1.5 nN, p <0.001). The labelling of the ABD leads to an decreased adhesive force on PEG for vegetative cells compared to the wildtype (veg.AX4: 1.4 nN, veg.AX4 with LimE: 0.4 nN, p <0.001; dev.AX4: 0.3 nN, dev.AX4 with LimE: 0.3 nN, p=0.31). Thus the trend for the substrate effect and therefore also the development were not influenced but the absolute adhesion was increased by labelling.

Similar results were found for the adhesion work, as shown in figure 4.7B. W_{adh} decreases for both vegetative (Glass: 2.4 fJ, PEG: 0.7 fJ) and developed (Glass: 1.8 fJ; PEG: 0.5 fJ) cells significantly from glass to PEG by labelling the ABD with LimE.

The ABD of vegetative AX2 cells was also labelled with LimE, as shown in figure 4.8. F_{max} decreased significantly from glass to PEG for LimE-labelled AX2. Compared

to the wildtype (AX2: 3 nN; AX2 with LimE: 3.6 nN) on glass, does the adhesion force increase significantly (p <0.001). A similar trend can be observed for PEG, the labelling of the ABD shows a significantly (p <0.001) increased adhesive strength on PEG compared to the wildtype (AX2: 0.2 nN; AX2 with LimE: 0.9 nN).

Labelling of myosin in AX2 significantly (p <0.001) increases adhesion strength compared to wildtype AX2 (AX2: 3 nN; AX2 with MyoII: 4.5 nN) on glass. This trend could not be observed on PEG (AX2: 0.2 nN; AX2 with MyoII: 0.1 nN). F_{max} increased significantly from glass to PEG by labelling myosin. Therefore labelling actin or myosin also increases adhesion in AX2 cells on glass, albeit leaving the difference between glass and PEG unaffected.

The adhesion work show a similar trend as F_{max}. W_{adh} decreased significantly from glass to PEG for labelled LimE (Glass: 4.0 fJ; PEG: 0.3 fJ) as well as labelled MyoII (Glass: 8.3 fJ; PEG: 0.3 fJ).

Thus the reason for the adhesion influence might be influence on cytoskeletal mechanics like cortical tension, as biopolymers as well as motor proteins show an effect.

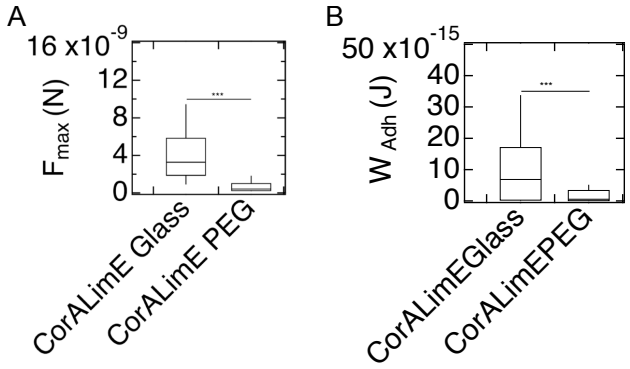

Figure 4.9: Adhesion properties for vegetative AX4 cells with cytoskeletal double labelling - F_{max} (A) and W_{adh} (B) for vegetative AX4 expressing LimE-GFP and CorA-RFP on glass and PEG. Image from [43] and slightly modified.

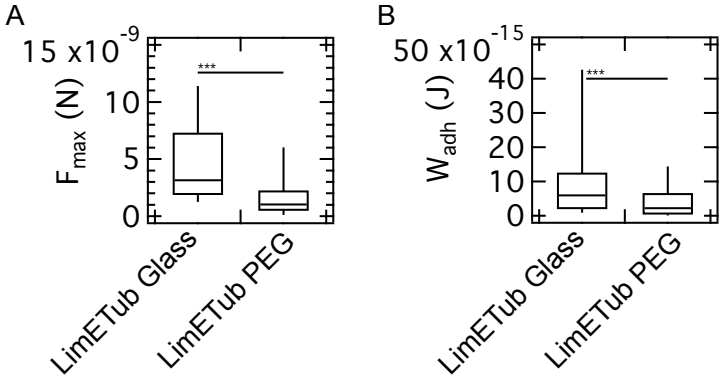

Figure 4.10: SCFS parameter of vegetative AX2 with double label - F_{max} (A) and W_{adh} (B) for vegetative AX2 cells on glass and PEG, expressing LimE-GFP and αTubulin-RFP.

Additionally a double label with tagged LimE and coronin was used in AX4, as shown in figure 4.9. Compared to AX4 with labelled LimE (2.4 nN) the additional coronin label significantly (p <0.001) increases the adhesion force (3.3 nN) on glass. An additional label does not change the adhesion strength on PEG (AX4 with LimE: 0.4 nN; AX4 with LimE and CorA: 0.4 nN). F_{max} as well as W_{adh} (Glass: 6.8 fJ; PEG: 0.5 fJ) decreased significantly from glass to PEG.

Additionally a double label with tagged LimE and αTubulin was used in AX2, as shown in figure 4.10. A second label shows no further increase in adhesion strength (AX2 with LimE: 3.6 nN; AX2 with LimE and Tub: 3.2 nN) on glass, but still significant (p <0.001) higher than the corresponding wildtype (AX2: 3 nN). However, the work of adhesion shows an increase with an increasing number of labels (AX2: 3 fJ; AX2 with LimE: 4.0 fJ; AX2 with LimE and Tub: 6.0 fJ). On PEG, an significantly (p <0.001) increase in adhesion force can also be observed with an increasing number of labels (AX2: 0.2 nN; AX2 with LimE: 0.9 nN; AX2 with LimE and Tub: 1.0 nN). In addition, an increase in adhesion work from single to double label can be measured (AX2 with LimE: 0.3 fJ; AX2 with LimE and Tub: 2.0 fJ). F_{max} and W_{adh} increased significantly from glass to PEG.

In summary, it can be said that there is a significant reduction in the adhesion properties from glass to PEG, regardless of the type of cytoskeletal protein labelled, the number of labels and the developmental stage of the cells. However, the increase in adhesion necessitates a more thorough study of cortical and adhesion mechanics as well as their dependence on substrate. As helpful as such labels are, they can affect the dynamics and mechanics of the cell.

5 Adhesion strategies of *Dictyostelium discoideum*- a force spectroscopy study

How does *D.d.* adhere to the surface without specific ligands in such a heterogeneous environment like the soil? To answer the question, I) model substrates were used to assess strength of Van der Waals (V.d.W.) as well as repulsive forces II) electrolyte concentrations were changed to reduce but quantify electrostatic interactions and III) the cell exterior was modified by deletion of the adhesive transmembrane protein SadA and a glycolytic degradation of parts of the glycocalyx by α-Mannosidase. Adhesion properties were measured by atomic force microscopy based single cell force spectroscopy (AFM-based SCFS). In addition, cell spreading has been analysed initially by TIRFM, then by CLSM and finally by sdCLSM for the extraction of the cellular behaviour, like the flatness. This section is based on the data published by Kamprad et al.[41]

5.1 Visualization of *D.d.* detachment by TIRFM-SCFS

To observe the adhesion properties of *D.d.* the process of detachment was initially observed by combining total internal reflection fluorescence microscopy (TIRFM) with AFM-based SCFS, an example is shown in figure 5.1.

Therefore the cell contour of a *D.d.* wildtype AX2 with a mRFPmars-tagged actin binding domain LimE was tracked with a custom made Matlab code (figure 5.1A) to determine the contact area (figure 5.1B). While the retraction part of the time-resolved force (FT) curve was recorded in parallel, as shown in figure 5.1C.

The contact area nicely shows that the cell during surface contact upon dwell time is mobile, which can be shown by the fluctuation in the contact area between -77.8 s and -53.6 s. After starting the retraction at -53.6 s, the contact area decreases in a linear manner. When reaching F_{max} at -48.7 s, the contact area is reduced to 35% of its original value (A(-53.6 s)= 21.670 px; A(-48.7 s) 7.511 px). In the FT curve, between -48.7 s and -40.0 s a small amount of jumps (black arrow) can be detected. At t=40.0 s the contact area reaches to zero, while at -40.1 s and -38.1 s two steps (red arrow) can still be detected in FT curve. Actin foci, as shown by white arrows in figure 5.1A could be only detected until -56 s optically, although their number matches with the tether numbers. This possibly is related to the xy resolution limit of the TIRFM (following Abbés law), which does not allow following the actin foci size below 250 nm diameter extension. Furthermore, the number of jumps and enclosed contact area patches match

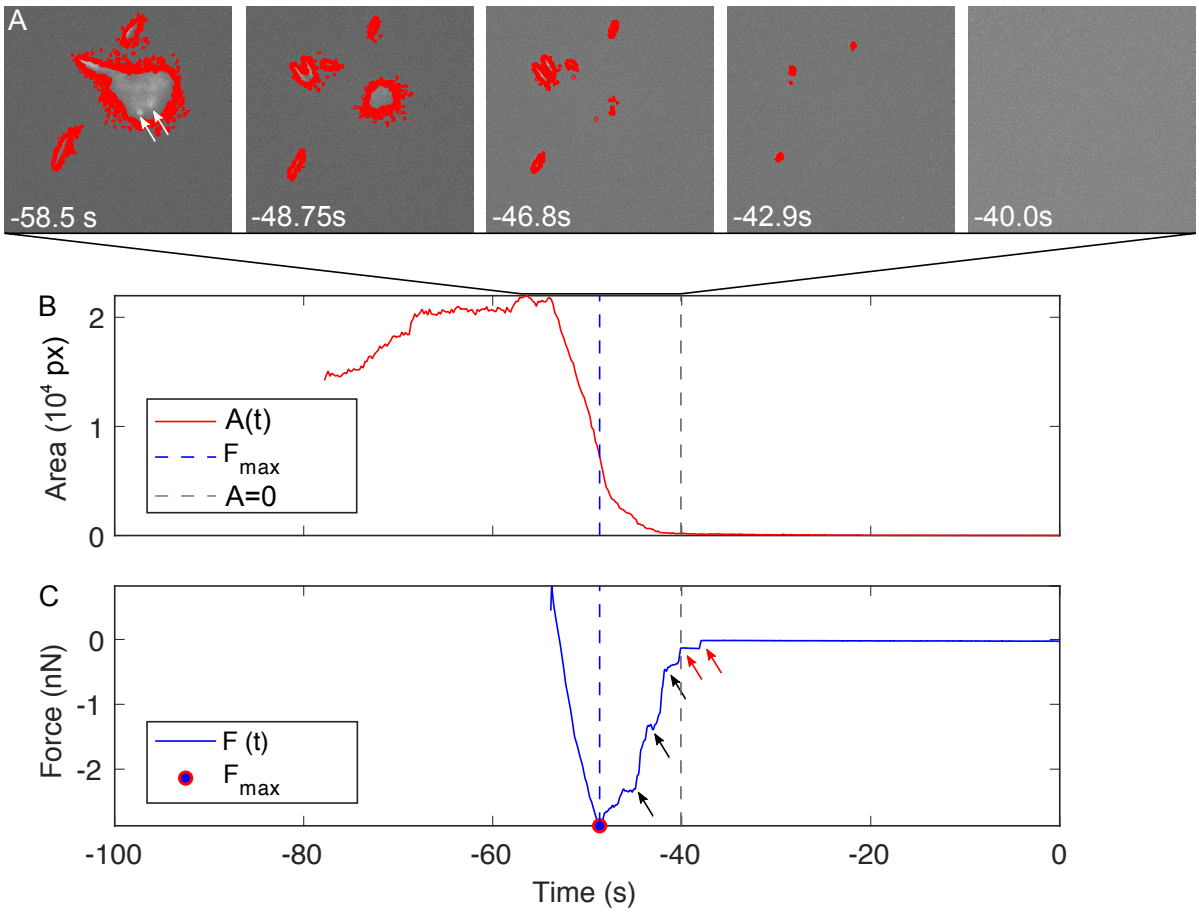

Figure 5.1: Combination of TIRFM and AFM-based SCFS - A: As example a TIRFM images of a *D.d.* wildtype AX2 of the time series with a GFP-tagged LimE actin binding domain. Cell contour is marked in red. Actin foci are marked with white arrows. Image size: 490x490px. B: Contact area (red) of the *D.d.* wildtype AX2 from A. In addition the time point of F_{max} from B is shown in blue. C: FT curve of *D.d.* wildtype AX2 from A. Jumps (black arrow) and steps (red arrow) are highlighted.

in the regime of the non-linear area decrease (-45 to -40 s, black arrows). For both step categories the actual rupture event can however occur beyond the surface distance of 250 nm which represents the maximal depth TIRFM can detect. Therefore xy but also z resolution limits the direct comparison of rupture events with TIRFM optics in a time resolved manner. In the future, an AFM combination with super-resolved optics could be an alternative.

Therefore, the environment was subsequently changed under controlled conditions (model substrates, change of ionic strength, reduction of adhesive components), so that conclusions can be drawn about the cell from the FD curve.

5.2 Influence of underlying substrates on adhesion: hydrophobicity and V.d.W. forces

As outlined in figure 5.2A, the detachment properties of the wildtype AX2 were analysed on two different model substrates: I) N-wafer with a thin/native SiO_2-layer (N-SiO_2) and II) T-wafer with a thick/thermally grown SiO_2-layer (T-SiO_2). For SCFS experiments at least 14 cells with 50 FD curves per category were measured. For flatness experiments at least 39 cells per category were measured.

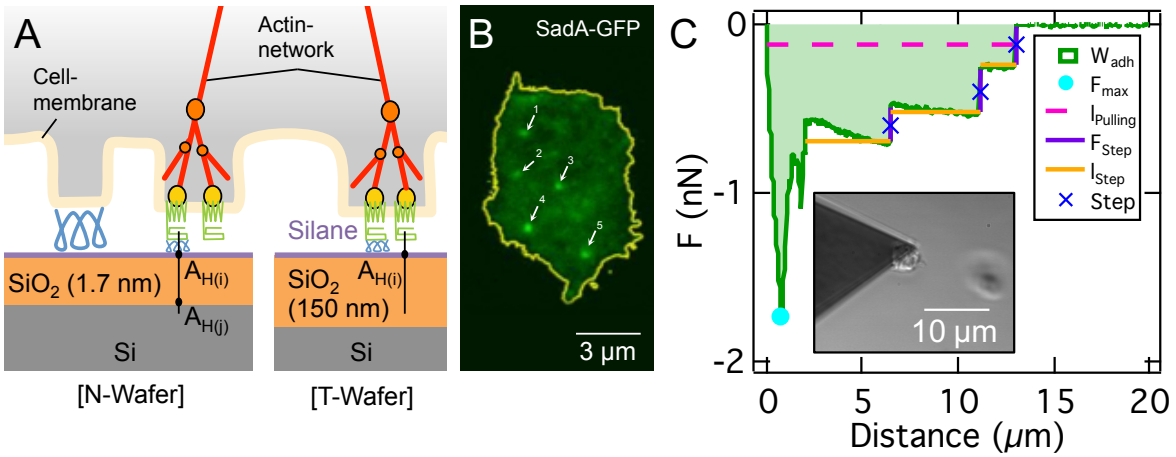

Figure 5.2: Fundamental methods of V.d.W. forces in *D.d.* adhesion - A: Sketch of an adhering *D.d.* cell on various model substrates. Actin network (red) with adhesion mediator proteins (actin nucleating proteins (yellow), actin branching proteins (orange), transmembrane proteins (green) like SadA and glycoproteins (blue)) is illustrated. As example a cell is shown on top of two different Si-wafers (left: N-wafer, right: T-wafer) with a silane surface modification (purple). B: TIRFM-image of a *D.d.* cell with SadA fused to GFP. Cell contour (yellow) as well as SadA cluster (white arrows) are highlighted. C: Comprehensive step analysis of a characteristic retrace part of a FD curve (*D.d.* wildtype AX3 cell on T-OTS): maximal adhesion force (F_{max}), adhesion work (W_{adh}), pulling length ($l_{Pulling}$), step force (F_{Step}), step length (l_{Step}) and number of steps. Subfigure: Bright-field image of an immobilized *D.d.* cell attached to a cantilever with a second out of focus cell on the substrate. Reprinted and modified with the permission of the publisher[41].

The general adhesion parameter, adhesion force F_{max} (figure 5.3A) and adhesion work W_{adh} (figure 5.3C), were extracted from the retraction part of the FD curve, as described in section 3.3.2. Both parameters show a significant decrease of the adhesion strength from N-SiO_2 (5.4 nN, 10.0 fJ) to T-SiO_2 (3.7 nN, 5.9 fJ).

In addition, these two model substrates were coated with a hydrophobic silane (OTS), thus named N-OTS and T-OTS, to change the hydrophobic properties of the substrate, which was verified via water contact angle measurements. Table 5.1 shows the change in water contact angle measurements from Piranha-cleaned wafer to the OTS-coating. Silanized wafers with different SiO_2 layers show a decrease from N- (3.1 nN) to the

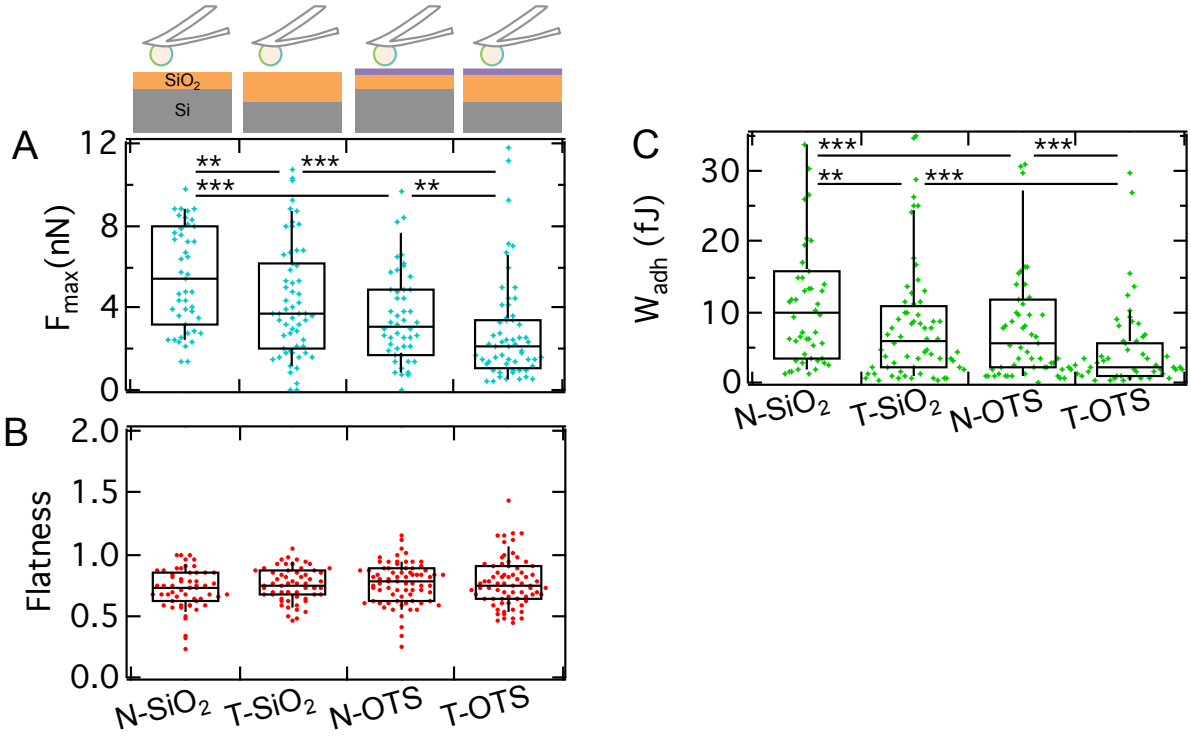

Figure 5.3: Adhesion strength of WT AX2 depending on the underlying substrate - Two different model substrates (Si): with thin (N-SiO_2) or thick (T-SiO_2) SiO_2 layer were used. Furthermore the hydrophilic substrates were silanized with OTS to become hydrophobic (N-OTS, T-OTS). A: The maximal adhesion force (F_{max}) decreases from N- to T-wafer both with and without silanization. B: The flatness is not influenced by any substrate changes. C: The adhesion work (W_{adh}) is reduced by the thickness of the SiO_2-layer as well the silanization as also F_{max}. Printed with the permission of the publisher [41].

T-wafer (2.1 nN). The adhesion strength is also influenced by the silanization, 5.4 nN (N-SiO_2) to 3.1 nN (N-OTS) and 3.7 nN (T-SiO_2) to 2.1 nN (T-OTS). In the past, the wildtype AX2 has been already measured on glass (AX2: 7.7 nN[150]), which is comparable to T-SiO_2 and shows similar adhesion forces. The measurements include more than 14 cells and 50 FD curves per category.

This clearly shows that long ranged V.d.W. forces contribute to the adhesion force and work of *D.d.* and the maximal adhesion forces are strongly enhanced on hydrophilic surfaces.

On the same model surfaces, the flatness factor of single *D.d.* cells (minimum 50 cells/category) was determined in order to assess the spreading behaviour and thus relate contact area changes to the observed modifications of the adhesion force. In addition, the flatness of AX2 was measured on customized glass surfaces (Flatness = 0.88, μ-dish) as a control, with a similar result as previously published [151]. The measurements show that model surfaces (Flatness $\approx$ 0.74) have no influence on the flatness of the cell so that cortical actomyosin-based forces maintain homeostasis. However, the flatness is slightly

Table 5.1: Overview of the substrate properties of N-, T-wafer and the silanization of the wafer. Advancing (α_{adv}) and receding (α_{rec}) contact angle of H_2O, as well as hysteresis based contact angle measurement ($\Delta\alpha$) (Piranha cleaned); complete wetting (CW). Parts of the table already published in [41]. Data from the literature[157] are in parentheses.

Substrate	*N-SiO₂*	*T-SiO₂*	*OTS*
α_{adv}	CW (5°)	CW (7°)	$113 \pm 3°$ (111°)
α_{rec}	CW (CW)	CW (CW)	$100 \pm 2°$ (103°)

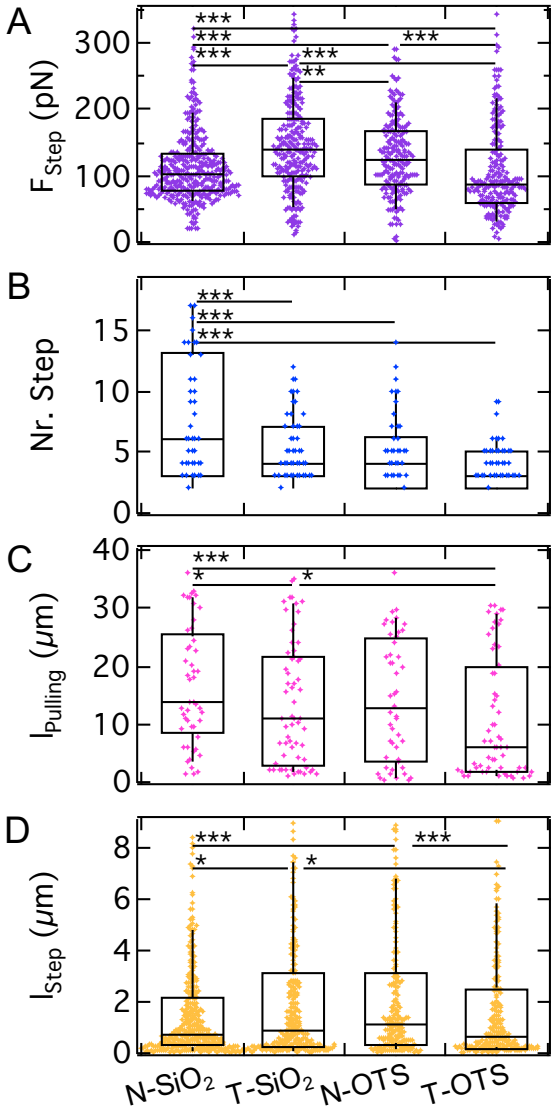

Figure 5.4: Step analysis of WT AX2 on model substrates - A: Step force (F_{Step}) shows no clear trend. B: Number of steps (N_{Step}) significantly decreases from N-SiO_2 to T-SiO_2 as well as for the silanized substrates. C: Pulling length ($l_{Pulling}$) decreases from the N to the T-wafer independent of the silanization. D: Step length (l_{Step}) show similar trend then F_{Step}. Printed with the permission of the publisher [41].

reduced compared to an untreated glass surface and thus the spreading behaviour slightly reduced.

Since the general adhesion parameter showed such a clear trend, it was interesting to analyse the influence of V.d.W. and hydrophobicity on steps of the FD curve as well. The results of the step analysis are shown in figure 5.4. Opposed to F_{max}, the step force F_{Step} increases from N-SiO_2 to T-SiO_2 (100 to 140 pN), but decreases from N- to T-OTS (120 to 90 pN). The number of steps decreases in the same degree as F_{max}, from N- to T-SiO_2 (6 to 4) and from N- to T-OTS (4 to 3). Only 5% of the curves of all substrates show no steps. The pulling length decreases from N- to T-wafer independently of the silanization (untreated: 14 to 11 μm; OTS-treated: 13 to 6 μm). The length of the steps (l_{Step}) shows a similar trend as F_{Step}, a increase from N- to T-SiO_2 (0.7 to 0.9 μm) and an decrease from N- to T-OTS (1.1 to 0.7 μm).

In summary, it could be shown, that the step properties show no clear trend except for the number of steps, which show weak similarities with the surface properties and thus the general adhesion parameters.

With equation 2.6 it was possible to calculate the adhesion energy density w from the radius of the cell and the critical adhesion force, as summarized in table 7.2 of the discussion. For the substrate N-SiO_2 a w of 0.34 $mN\ m^{-1}$ could be calculated, which decreases to 0.26 $mN\ m^{-1}$ for T-SiO_2, to 0.20 $mN\ m^{-1}$ on N-OTS, to 0.13 $mN\ m^{-1}$ on T-OTS. This nicely shows that V.d.W. forces contribute as expected to w.

5.3 Cell-substrate adhesion depends on ionic strength of the environment

D.d. lives is the soil, which is a rather heterogeneous substrate with many interfaces of eventually diverging V.d.W. forces or hydrophobic strength. The amoeba compensates for this quite well, as already seen in the previous section. In addition, the soil is porous and stores aqueous solution of different saline conditions. The phosphate buffer (PB) has a pH of 6, which means that the used model substrate T-SiO_2 (similar properties to glass) would be negatively charged[130] as well as the cell surface under these experimental conditions. Here, the ionic strength (IS) of PB was modified to evaluate the strength of electrostatic interactions upon *D.d.* adhesion. As reference, AX3 wildtype cells were measured in conventional K^+- and Mg^{2+}-free PB, which has a IS of 16 mM. Potassium and magnesium have little influence on initial *D.d.* adhesion and cell migration[126], Potassium can replace calcium, but magnesium cannot. Magnesium is a cofactor in ATP synthesis and potassium is relevant for transmembrane pumps. Both are therefore suited for electrostatic measurements, in addition they vary in their valence. The change in ion concentration was limited to the osmoregulatory regime of *D.d.* to avoid changes in volume and thus contact area, which might influence adhesion.

For osmoregulatory experiments, as described in chapter 3.1, the adding of more solute to increase the ionic strength was done without moving neither the AFM-head during SCFS experiments nor the sample in flatness experiment. For SCFS experiments at

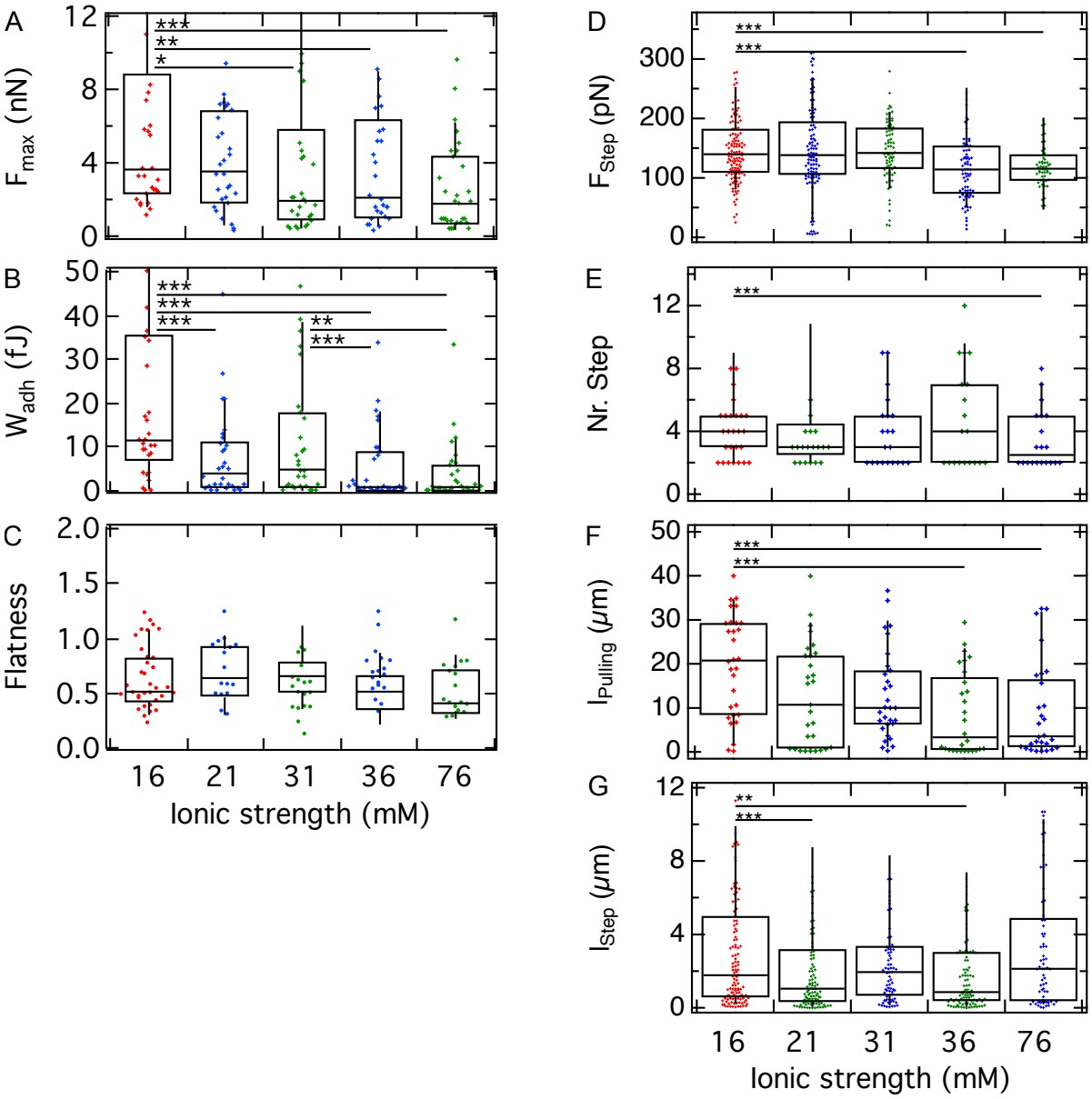

Figure 5.5: Influence of ionic strength (IS) on adhesion force spreading and step spectroscopy of AX3 *D.d.* wildtype cells measured on T-SiO_2 - A: Maximal adhesion force (F_{max}) decreases with increasing ion strength. B: Adhesion work (W_{adh}) decreases with increasing ion strength independent. C: Flatness is independent of the ion strength and valence of the ions. D-F: Significant decrease of step parameter (step force (F_{Step}), number of steps, pulling length ($l_{Pulling}$)) from buffer (16 mM) to the strongest ionic strength and thus electrostatic interaction, 76.2 mM Mg^{2+}. G: Step length (l_{Step}) decreases by treating with KCl. Slightly modified with the permission of the publisher [41].

least 6 cells with 18 FD curves per category were measured. To determine the spreading behaviour, at least 15 cells were analysed for each setup.

The maximal adhesion force F_{max} of AX3 on T-SiO_2, as shown in figure 5.5A, in PB (IS: 16 mM) is 3.7 nN. The accumulation of K^+ (5 mM KCl, IS: 21 mM; 3.5 nN) in PB shows no significant differences. A further increase in the ionic strength to 36 mM (20 mM KCl) decreases F_{max} significantly to 2.1 nN. The divalent Mg^{2+} reduces the adhesion strength by adding 5 mM $MgCl_2$ (IS: 31 mM; 1.9 nN). Advanced enrichment (20 mM $MgCl_2$, IS: 76 mM) shows no further decrease. In addition, the adhesion work W_{adh} (figure 5.5B) was analysed, which shows similar trend as F_{max}, the differences between the categories are much stronger. W_{adh} of the K^+ and Mg^{2+}-free buffer is 10 fJ and decreases after enrichment to 5 mM KCl significantly to 3.9 fJ. Advanced enrichment (20 mM KCl, W_{adh}=1.0 fJ) reduces W_{adh} even further. The effect of adding Mg^{2+} is weaker but similar (5 mM $MgCl_2$: 5.0 fJ; 20 mM $MgCl_2$: 1.0 fJ) and significant as opposed to F_{max}.

The spreading behaviour, figure 5.5C, is neither significantly influenced by the ionic strength nor the valence of the ions, so we can exclude osmotic swelling or changes in spreading morphology as a source for F_{max} reduction.

The step analysis (figure 5.5D-G) show a significant decrease of the step force (F_{Step}) at ionic strength higher than 36 mM (16 mM: 140 pN; 36 mM: 114 pN; 76 mM: 116 pN). The number of steps does not change significantly (16 mM:), with the exception of the enrichment to 20 mM $MgCl_2$. The evaluated force curves show on average three to four steps independent of the ionic strength or valence of the ions, with the exception of IS=76 mM, where the number of steps per FD curve is slightly reduced to 2.5. It is noticeable, however, that the number of curves without steps increases from 3% (IS: 16 mM) to about 30% independent of strength or valence of the ions (16 mM: 23.3%; 31 mM: 36.4% 36 mM: 38.7%; 76 mM: 33.3%). The pulling length decreases with increasing ionic strength, independent of the valence of the ions, from 20.7 μm (IS: 16 mM) to 3.5 μm (IS> 36 mM).

The step analysis showed the strongest changes at the highest concentration of Mg^{2+}, with the exception of the step length (PB: 1.8 μm), which is not affected by Mg^{2+} but significantly by K^+ (5 mM KCl: 1.0 μm; 20 mM KCl: 0.9 μm).

AX3 in PB on T-SiO_2 has an adhesion energy density of 0.24 $mN\ m^{-1}$, which decreases slightly by the enrichment to 5 mM KCl (0.22 $mN\ m^{-1}$) and stronger by the enrichment to 20 mM KCl. In the case of Mg^{2+}, w decreased to 0.12 $mN\ m^{-1}$ independent of the added concentration.

The change in ionic strength examined here seems to have an effect on the organisation of the SadA cluster, while much stronger changes are expected for the aqueous soil solution, which could then also have a stronger influence on the adhesive force, but possibly also be based on osmosis.

5.4 Influence of cell specific adhesion protein cluster and the glycocalyx on *D.d.* adhesion

Besides the aspects based on the DLVO theory described in the two previous chapters, the cells also actively contribute to cell-substrate adhesion. Therefore specific adhesion molecules are necessary. The amoeba *D.d.* uses the transmembrane protein SadA to bind on surfaces and aggregate into adhesion clusters, as shown in figure 5.2A/B. Next to adhesion[58] is SadA also important for the connection to the cytoskeleton[59] to allow force transition. In addition, *D.d.* has glycoproteins integrated in the cell membrane, where the big glycolytic head groups can interact with the environment (e.g. by steric repulsion), thus comparable to the glycocalyx of mammalian cells; the ECM only exist in the multicellular stage of the life cycle. These head groups are rich in $1' - 5'$-linked mannose, which can be easily degraded enzymatically with α-Mannosidase (αM). Glycolytic enzyme treatment of the whole cell can significantly reduce cell-substrate adhesion.[62, 121]

The following conditions were analysed: I) *D.d.* wildtype AX3 cells as reference II) protein deletion of SadA in AX3 (SadA0) III) glycolysis of AX3 with αM-treatment (AX3+αM) IV) combination of SadA0 cells and αM-treatment (SadA0+αM). All measurements were made on the least adhesive substrate T-OTS to reduce both specific as well as unspecific adhesion even further to a minimum. For SCFS experiments at least 11 cells with 57 FD curves per category were measured. For flatness experiments at least 29 cells per category were measured.

The maximal adhesion force (F_{max}; AX3: 2.5 nN) can be reduced both by glycolysis (1.4 nN) and by the deletion of SadA (0.7 nN), the latter being more efficient (figure 5.6A). F_{max} decreased even significantly more when SadA0 cells are glycolysed (0.5 nN). The adhesion work (W_{adh}, figure 5.6B) follows the same trend as F_{max}. AX3 has a W_{adh} of 3.8 fJ, which will be decreased by both the αM-treatment (1.5 fJ) and the deletion of SadA (0.8 fJ). The combination of those methods reduces W_{adh} even further (AX3+SadA0+αM: 0.3 fJ), which is more significant for the W_{adh} than F_{max}. However only F_{max} captures the differences between glycolytic treated wildtype and deletion of SadA.

Surprisingly, the spreading behaviour of αM-treated cell increased slightly compared to the WT AX3 (figure 5.6C), while SadA0 reduces spreading behaviour as expected. The αM-treatment of SadA0 leads to no further changes of the flatness factor. If the parameters contributing to the flatness, volume and contact area, are considered separately, as shown in figure 5.6D/E, the following can be observed: Glycolysis promotes a volume reduction at constant contact area. While the deletion of SadA causes an increase in volume and a reduction in contact area. Fey et al.[58] observed on SadA0 cells an increased amount of multinucleated cells, which show an increased cell surface area of 175 μm^2 (fixed, flattened cells). This corresponds to a radius of 9 μm. To exclude multinucleated cells, we followed the cell radius. The cell radius increases from WT to SadA0 only from 5.9 to 7.3 μm (after αM-treatment: WT 5.0 μm, SadA0 7.0 μm).

Besides evaluating F_{max}, we again performed step spectroscopy related to the SadA

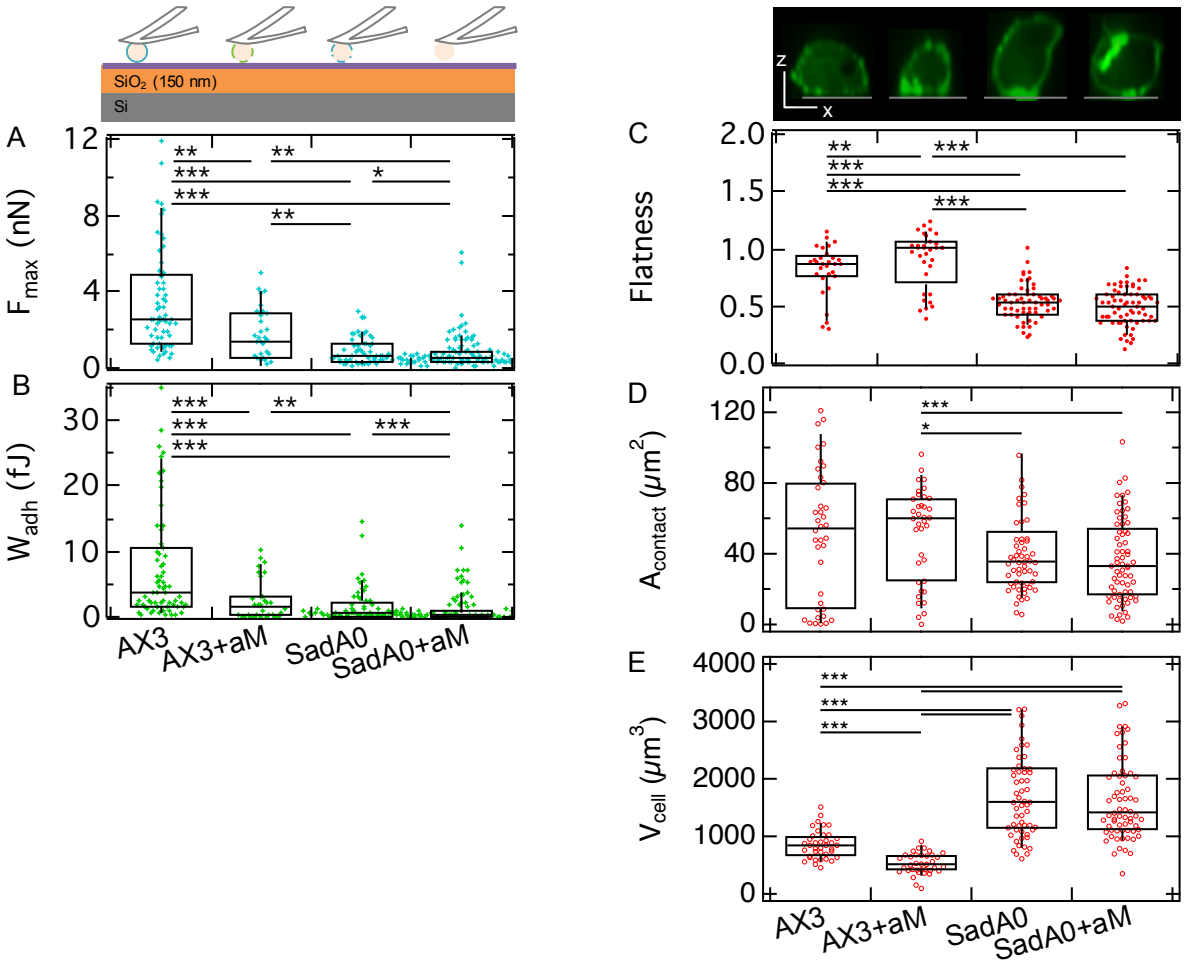

Figure 5.6: Adhesion strength depending on the cell exterior of WT AX3 - For the SCFS measurements the least adhesive substrate T-OTS was used, as shown in the sketch on top of A. Furthermore AX3 was used I) as reference II) αM-treated III) with a k.o. of SadA IV) in combination of SadA0 and αM-treatment. A: The maximal adhesion force (F_{max}) decreases in the following order: AX3, AX3+αM, SadA0, SadA0+αM. B: The adhesion work (W_{adh}) decreases in the same order such as F_{max}. C: A cross-section of the used cell is shown. To visualize the cortex GFP-tagged LimE was used (scale bar: $5\mu m$, substrate: grey line). The flatness increased with the αM-treatment and decreases with the deletion of SadA. The combination of SadA0+αM shows a decreased flatness. D: Contact area ($A_{contact}$), contributing to the flatness, decreases with the deleting of SadA. E: The cell volume (V_{cell}), contributing to the flatness, decreases with the treatment of αM and increases with the deletion of SadA. A-C: Printed with the permission of the publisher [41].

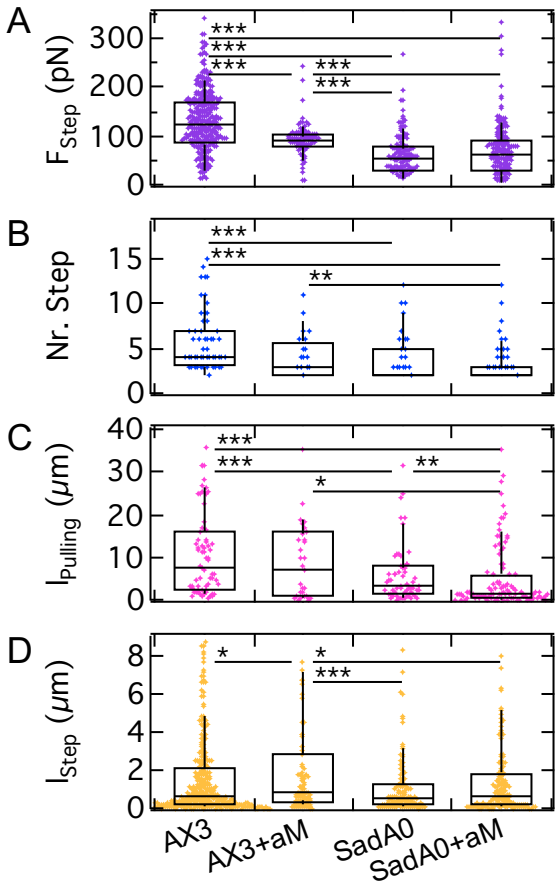

Figure 5.7: Step analysis of WT AX3 on T-SiO$_2$ - AX3 was used I) as reference II) αM-treated III) with a deletion of SadA IV) in combination of SadA0 and αM-treatment. A-C: Step force (F_{Step}), Number of steps (N_{Step}) and the pulling length ($l_{Pulling}$) decreases from AX3 to SadA0 cells. αM-treatment does not show such a clear trend. D: Step length (l_{Step}) shows no clear trend for any modification. Printed with the permission of the publisher [41].

cluster, small spots of close contact of the cell, which still adhere to the substrate after the de-adhesion force minimum has been overcome. These contact points are released stochastically until the cell is completely detached. In the following, these rupture events are examined in more detail, see figure 5.7A-D. The αM-treatment reduced the step force (F_{Step}) from 120 to 90 pN. The deletion of SadA affects F_{Step} by a factor of two (50 pN). The number of steps decreases from 4 (AX3) to 2 (SadA0+αM). The amount of curves without steps increases from AX3 (4%), to AX3+αM (23%), to SadA0 (33%), to SadA0+αM (46%). The pulling length ($l_{Pulling}$) is not affected by glycolysis (7.3 to 6.8 μm), while the deletion of SadA (3.09 μm) and SadA0 cells with the αM-treatment (1.63 μm) decreases it significantly. The step length does vary a lot without a clear trend for any of these modifications (between 520 and 860 nm). In summary the step force follows the trend of F_{max} and W_{adh}, while l_{step} is the least sensitive parameter to glycolysis and SadA deletion.

The adhesion energy of AX3 on T-OTS is already small (0.13 $mN\ m^{-1}$) and decreased by adding αM slightly (0.09 $mN\ m^{-1}$). SadA0 (0.03 $mN\ m^{-1}$) and SadA0+αM (0.02 $mN\ m^{-1}$) show the smallest values of w.

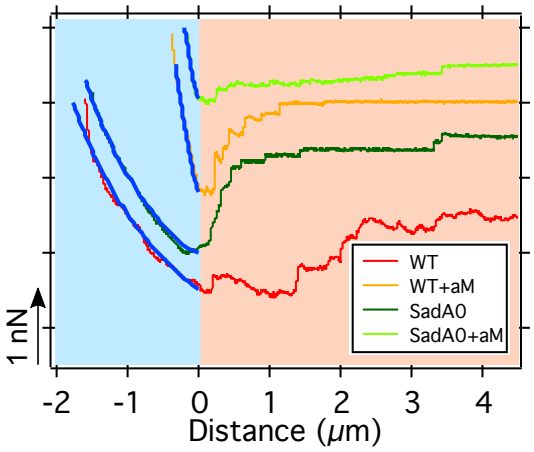

Figure 5.8: Influence of cell specific adhesion structures of FD curves - Experimental FD curves of the WT AX3 (red) and AX3 SadA0 (dark green) on T-OTS are shown. In addition both cell types with a α-Mannosidase (αM) treatment (orange, light green). In addition computational FD curves of the four categories are shown as an overlay (dark blue). The figure is divided at the minimum of the FD curve into a continuum (light blue) part and a stochastic (light orange) part, which is dominated by rupture events. There is a good agreement of experimental and computational data until the critical adhesion force is reached. Printed with the permission of the publisher [41].

A summary of the retraction part of the FD curves from the four categories is shown in figure 5.8. As example next to FD curves, computational FD curves were plotted until the critical adhesion force is reached, which are used to determine w based on F_{crit} and the radius of the cell. Details of the used parameter are shown in [41].

In combination we find, that the effect of SadA deletion dominates over glycocalyx degradation but might indicate heavy glycolysation of SadA. It is similar to patterns found for latrunculin treated cells missing the actin cytoskeleton[121]. Therefore the minimal adhesion implies we were able to identify two major molecular components mediating substrate adhesion, but cells are still able to adhere even without both.

6 Actin foci dynamics and adhesion cluster mechanics of *Dictyostelium discoideum*

As shown in the previous section, the transmembrane protein SadA is of central relevance for *D.d.* adhesion. This section will analyse the influence of the deletion of key actin binding proteins linking SadA to the cytoskeleton on adhesion properties with RICM as well as AFM-based SCFS, especially focused on the step analysis to describe SadA cluster mechanics under deletion influence.

Furthermore, it will be studied whether SadA deletion influences actin foci, dynamic structures of freshly polymerised actin at the ventral side of the cell. Actin foci dynamics are characterized with actin fused to different fluorophores using TIRFM, in addition to quantifying the influence of the axenic background.

The link between actin foci and SadA is studied by deletion experiments of key actin binding proteins relevant to adhesion as well as endocytosis signalling. The following key actin binding proteins were deleted: The actin anchoring proteins TalA and TalB, actin polymerization initiator and bundling protein ForA, actin nucleation-promoting factor ScarA, as well as actin branching protein Arp2/3.

Finally a connection of actin foci to clathrin mediated endocytosis is examined in co-localization studies. Furthermore TIRFM and RICM are combined to visualize membrane movement at positions of actin foci.

6.1 Influence of key actin binding proteins on relative contact and cluster mechanics of *D.d.*

In this set of experiments two techniques to measure the adhesion properties of cells are used: I) The relative contact area determination, through the ratio of RICM-based contact area to the projected bright field area II) AFM-based SCFS including step spectroscopy.

Figure 6.1A-C shows the relative contact of all measured WTs as well as of cells with the deletion of key actin binding proteins and the inhibition of the Arp2/3 complex with CK666. In addition the median of all measured parameter is given in brackets in the text below. AX3 with the deletion of SadA (0.4) as well as AX2 with the deletion of TalA (0.22) show a strong decrease of the relative contacts in comparison to their corresponding WT (AX3: 0.81; AX2: 0.56). Noticeable, the relative contact of wildtypes

AX2 and AX3 differ strongly. In comparison the treatment with CK666 (0.61), the deletion of ForA (0.71) and the deletion of ScarA (0.68) show a gradual increase in the relative contact, in reference to AX2. The deletion of TalB evokes no difference in relative contact to the corresponding wildtype DH1. Only strong changes in the adhesion properties can be captured by this method.

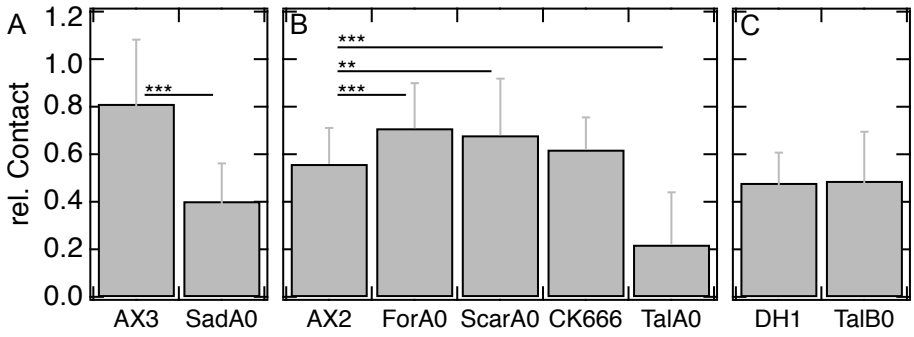

Figure 6.1: Relative contact of WT *D.d.* and cells with deletion of key actin binding proteins - A: SadA0 cells show a strong decrease of the relative contact in comparison to AX3. B: ForA0, ScarA0 and CK666 cells show a gradual increase in the relative contact. In contrast, TalA0 cells show a decrease (data partially published in [150]). C: TalB0 show no significant differences to their corresponding WT.

In addition, AFM-based SCFS was employed to measure global adhesion properties as well as step properties. Tarantola et al.[121] have previously optimised the SCFS parameters in terms of contact force, contact time and pulling speed under the following aspects: For AX3, a contact time of 30 s and a contact force of 0.5 nN, F_{max} was found to be almost constant for pulling speeds from 0.1 to 4 $\mu m/s$, where upon it increased stepwise. No hydrodynamic drag is observed and cells remain attached to the cantilever in a minimally invasive manner, while allowing the formation of new foci. An optimum pulling speed of 2.5 $\mu m/s$ was determined. The influence of pulling speed on step analyses will be quantified in the following. Wildtype AX3 as well as SadA deleted AX3 cells were measured with pulling speeds of 0.5, 1, 2 and 2.5 $\mu m/s$ at a contact time of 30 s (contact force 0.5 nN). Next to the general parameters F_{max} and W_{adh}, a step analysis was carried out, as shown in figure 6.2. Significance tests were only made within the category for AX3 or SadA0 cell, with exception of 2.5 $\mu m/s$ (as shown in figure 6.3) and only with the next higher speed.

Regarding F_{max}, neither AX3 nor SadA0 cells significantly differ depending on the pulling speed, with F_{max} being almost constant over the whole range of applied velocities with one exception: Differences between the AX3 and SadA0 become significant with a pulling speed of 2.5 $\mu m/s$ (AX3 5.9 nN, SadA0: 1.4 nN).

W_{adh} of AX3 increased with increasing pulling speed up to 9.4 fJ at 2.5 $\mu m/s$, while SadA0 cells show a decreasing trend (W_{adh} ranging from 6 to 0.5 fJ). F_{max} and W_{adh} of AX3 and SadA0 cells at a contact time of 0 s is small ($\approx 0.2\ nN$, $\approx 0.1\ fJ$), and a step analysis is not possible due to missing steps.

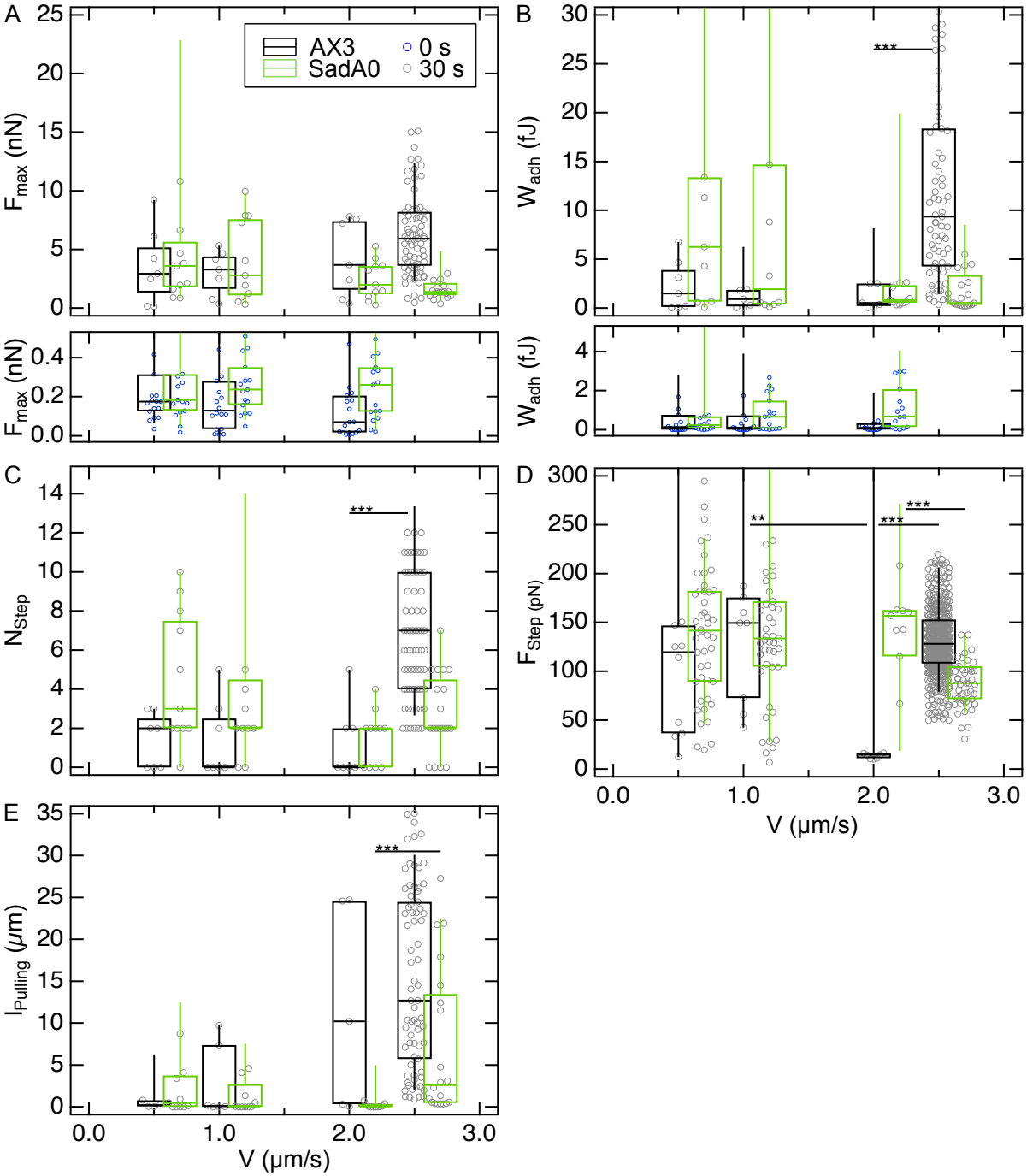

Figure 6.2: Pulling speed-dependent adhesion properties - Adhesion properties of vegetative WT AX3 (black) and AX3 SadA0 (green, offset of 0.2 $\mu m/s$) are measured mainly at a contact time of 30 s (grey dots; blue dots for contact time of 0 s) at different pulling velocities (V) on glass: maximal adhesion force (A), adhesion work (B), number of steps per FD curve (C), step force (D) as well as the pulling length (E).

In the case of AX3 the number of steps increased with increasing pulling speed up to 7 per FD curve, where in comparison SadA0 cells show the number of steps decrease in a range of 5 to 0 with increasing pulling speed.

The step force is not influenced by the pulling speed in the case of AX3 ($\approx 120\ pN$), with the exception of the measurement of 2 $\mu m/s$. In contrast, SadA0 cells show a reduction in step force with increasing pulling speed up to 88 pN at 2.5 $\mu m/s$. The pulling length shows no significant differences between the neighbouring velocity categories, with the exception of SadA0 increasing from 2 to 2.5 $\mu m/s$. The difference between AX3 (13 μm) and SadA0 (3 μm) is significant, too. Based on these results, the established parameters were maintained.

In addition to the SCFS measurements of wildtype AX3 and the deletion of SadA in AX3 cells, adhesion of other wildtypes (AX2, DH1) and inhibited or deleted key actin binding proteins (Arp2/3, TalA, TalB) were quantified. Most results (with the exception of TalB0) can be seen in the figure 6.3. All median values of the measurements are shown in table 6.1 and given in brackets in the following text.

The three axenic wildtypes (AX3, AX2, DH1) show similar adhesion properties, as shown in figure 6.3: F_{max} ranges from 5.3 to 5.9 nN, W_{adh} from 8.9 to 10.9 fJ, N_{Step} from 5 to 8 steps per FD curve, F_{Step} from 113 to 128 pN and l_{Step} from 0.55 to 0.76 μm. AX3 cells show a reduction in the $l_{Pulling}$ (12.7 μm) by one third in comparison to AX2 (19.1 μm) and DH1 (17.6 μm). The global parameter F_{max} is strongly reduced to 20-40% for SadA0 (1.4 nN) and TalA0 (1.7 nN) and to 60-70% for CK666 (3.8 nN), ForA0 (3.1 nN) and TalB0 (3.7 nN). The global parameter W_{adh} is reduced strongly to 10-30% for SadA0 (0.5 fJ), CK666 (3.0 fJ) and TalA0 (1.7 fJ) and to 60-80% for ScarA0 (9.0 fJ), ForA0 (6.6 fJ) and TalB0 (7.5 fJ).

WT cells show no (AX3, DH1) or a low amount (AX2: 6%) of FD curves without steps. In comparison 16% of FD curves for cells treated with CK666, 20% of SadA0 and 30% of TalA0 show no steps. The number of measured steps per FD curve is strongly reduced to 30% by SadA0 (2), CK666 (2.5) and TalA0 (2). The step force is slightly reduced to 70-90% in all cases (SadA0: 88 pN; ScarA0: 109 pN; CK666: 85 pN; TalA0: 84 pN; ForA0: 110 pN; TalB0: 101 pN). SadA0 show no significant differences in the step length in comparison to the corresponding wildtype AX3. Steps of TalA0 (0.93 μm) and TalB0 (1.18 μm) cells are significant longer (60%). CK666 inhibition reduces the step length by 30% (0.41 μm). The pulling length is strongly reduced to 10-20% by SadA0 (2.6 μm), CK666 (4.0 μm) and TalA0 (2.5 μm) and slightly (70%) by ScarA0 (13.6 μm) and ForA0 (13.8 μm).

In summary, SadA0 and TalA0 cells show a strong reduction of the most categories, with the exception of the step length. The inhibition with CK666 is similar but slightly less strong than the TalA deletion. WT cells show similar properties in all categories, with the exception of the pulling length of AX3. This mostly corresponds to the trend found for F_{max} and W_{adh}, but besides TalA, surprisingly not to the relative contact for AX2 and DH1.

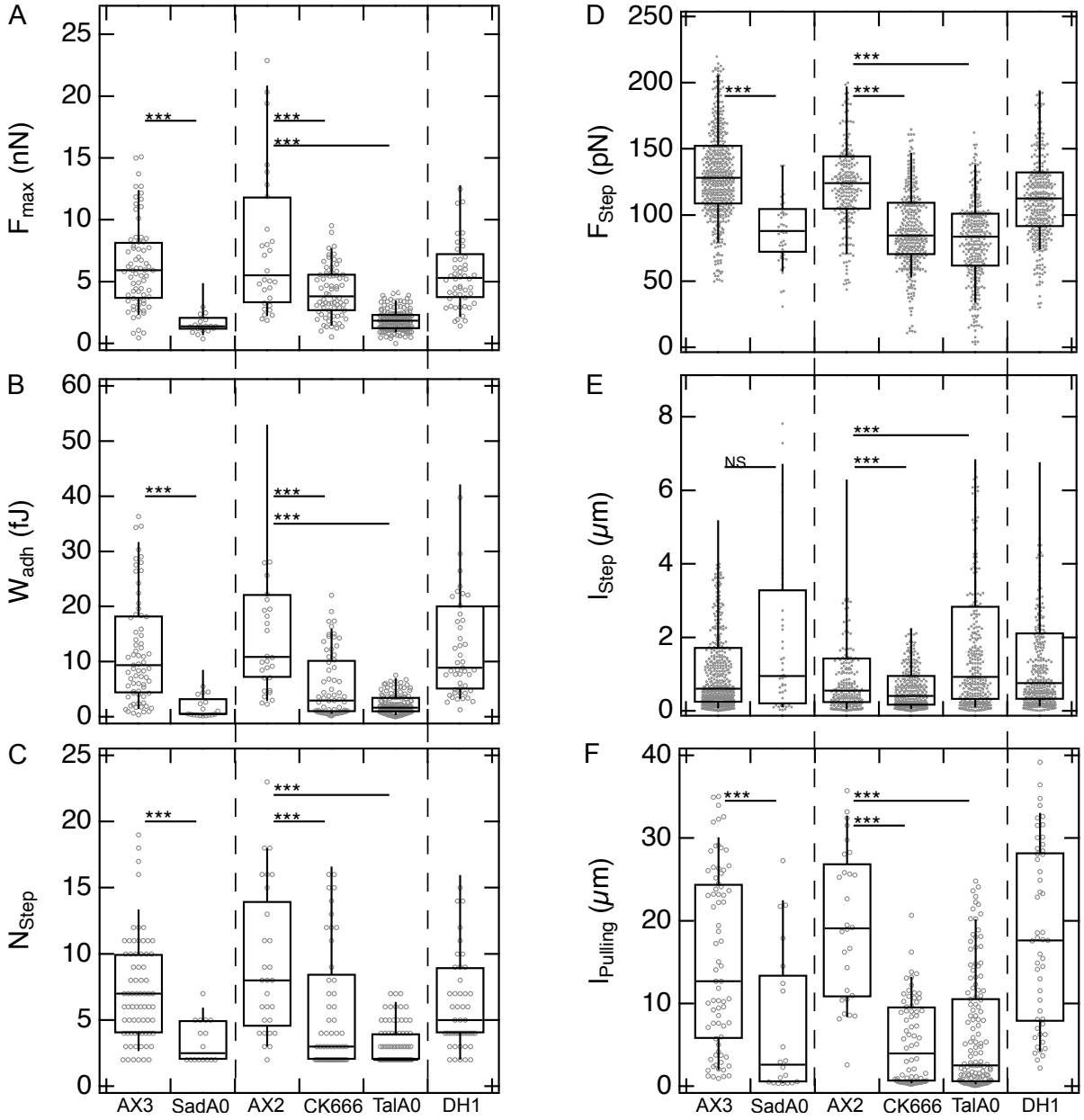

Figure 6.3: Analysis of adhesion properties of *D.d.* and corresponding key actin binding proteins - Adhesion force (A), -work (B), the number of steps (C), the step force (D) and the pulling length (F) show the same decreasing trend. E: Step length increases for TalA0 and decreases for the inhibition with CK666 in comparison to AX2.

Table 6.1: Influence of key actin binding protein deletion on cell-substrate adhesion of *D.d.* - Step analysis of FD curves with inhibited/deleted key actin binding proteins and the corresponding axenic background. Wildtype (AX3, AX2, DH1) parameters are comparable. SadA0, CK666 and TalA0 affect the number of steps strongly (N_{Step}), the step force (F_{Step} in pN) and the pulling length (l_{Pulling} in μm). The step length (l_{Step} in μm) increases with the deletion of TalA and TalB. Furthermore the general parameter maximal adhesion force (F_{max} in nN) and -work (W_{adh} in fJ) are shown, both show similarities with F_{Step}. ‡ already published in [150].

Parameter	**AX3**	SadA0	**AX2**	ScarA0	CK666	TalA0	ForA0	**DH1**	TalB0
N_{Step}	7	2^{***}	8	6^{NS}	2.5^{***}	2^{***}	6^{NS}	5	5^{NS}
F_{Step}	128	88^{***}	124	109^{***}	85^{***}	84^{***}	110^{***}	113	101^{***}
l_{Step}	0.61	0.95^{NS}	0.55	0.54^{NS}	0.41^{***}	0.93^{***}	0.65^{NS}	0.76	1.18^{***}
l_{Pulling}	12.7	2.6^{***}	19.1	13.6^{**}	4.0^{***}	2.5^{***}	13.8^{**}	17.6	18^{NS}
F_{max}	5.9	1.4^{***}	5.5	5.2^{NS}	3.8^{***}	$2.0^{***‡}$	3.1^{***}	5.3	3.7^{***}
W_{adh}	9.4	0.5^{***}	10.9	9.0^{*}	3.0^{***}	1.7^{***}	6.6^{***}	8.9	7.5^{*}

6.2 Characterization of actin foci in AX2

To characterize actin foci dynamics, time series of actin fluorescence labelled *D.d.* cell were recorded. Therefore, as shown in figure 6.4A, next to the boundary of the cell, the foci contour was detected. The temporal evolution of the intensity profile for a single focus is shown in figure 6.4B. An example of a time trace is shown in figure 6.4C. The following parameter have been analysed and determined: time of maximum signal

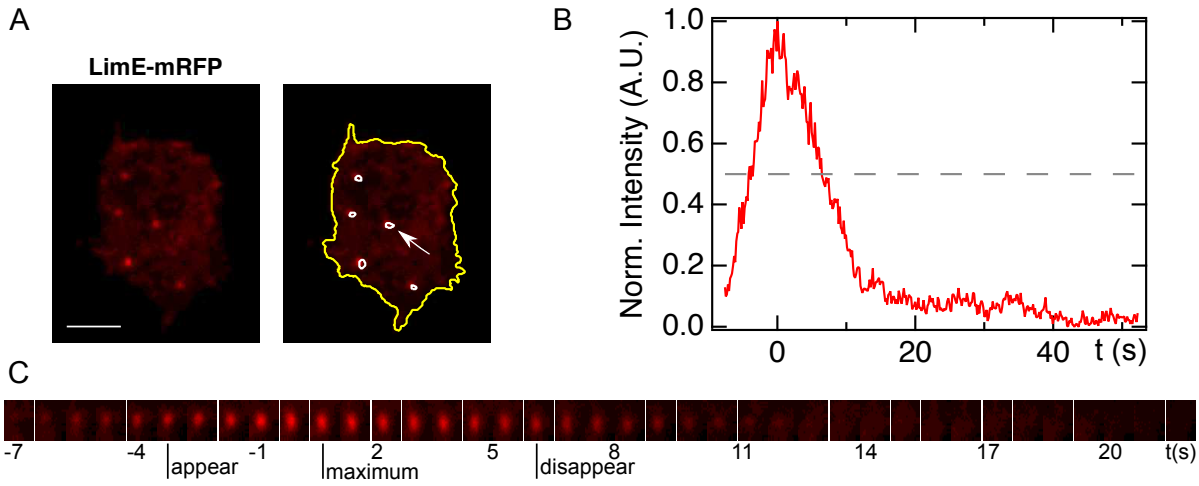

Figure 6.4: Actin foci detection based on TIRFM - A: TIRFM image of a *D.d.* wildtype AX3 with a mRFPmars-tagged LimE (corresponding to -3 s in B/C). Right image shows additionally tracked boundary (yellow) and contour of the actin foci (white). Scale bar 3 μm. B: Intensity profile of an actin focus (white arrow of A). I_{50} is marked with a dashed line. C: Time series of actin focus (white arrow in A). Appearance and disappearance time at half intensity as well as the maximum intensity are marked.

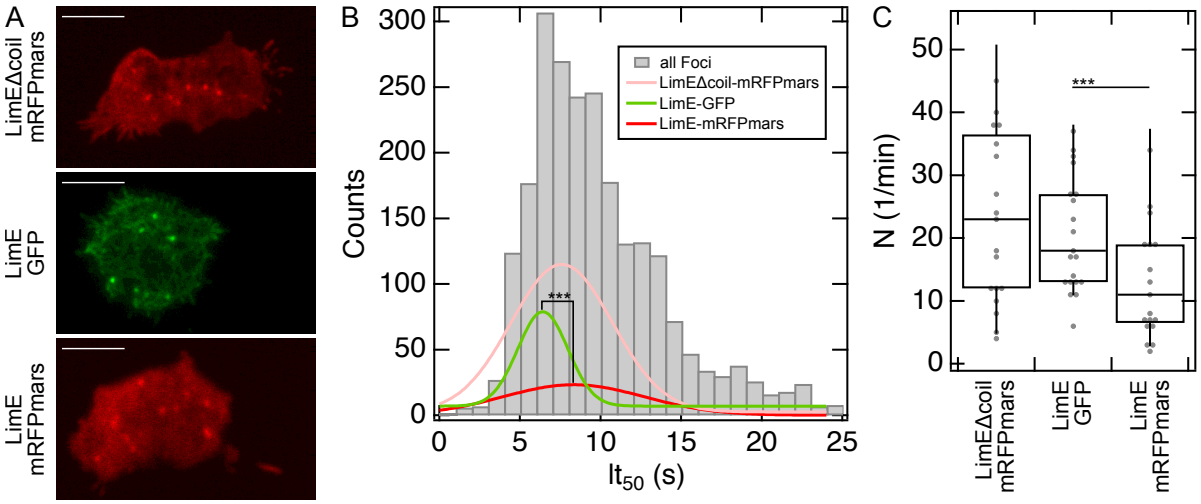

Figure 6.5: Characterisation of the actin bindings domain LimE and LimEΔcoil as well as fluorophores - $\mathcal{S}$-experiments of LimE and LimEΔcoil with two different fluorophores. A: As example a TIRFM images of LimEΔcoil-mRFPmars, LimE-GFP and LimE-mRFPmars. Scale bar: 2.5 μm. B: Histogram of the half lifetime (lt_{50}) of all used actin binding domains, merged. Sub-populations are Gauss-fitted (LimEΔcoil: 7.6 s; LimE-GFP: 6.4 s, LimE-mRFPmars: 8.4 s). C: Number of actin foci per minute. The ratio depends on the actin binding domain and fluorophore (LimEΔcoil-mRFPmars: 23; LimE-GFP: 18, LimE-mRFPmars: 11 $Foci/min$).

intensity (t_{max}), the appearance (t_{before}) and disappearance (t_{after}) time at half of the maximum signal intensity, and the resulting half lifetime (lt_{50}).

These parameters were extracted from a first set of $\mathcal{S}$-experiments with t_c=150 ms, t_{exp}=50 ms and t_{total}= 60s; for both mRFPmars- and GFP-tagged LimE as well as LimEΔcoil-mRFPmars in *D.d.* wildtype AX2, as shown in figure 6.5, where at least 17 cells were measured. The following values refer to the median.

The half lifetime of actin foci is surprisingly slightly affected by the fluorophore (LimE-GFP: 6.4 s; LimE-mRFPmars: 8.4 s). In comparison the amount of detectable foci is more affected by the ABD (LimEΔ: 23 min^{-1}; LimE: 11 min^{-1}). Appearance and disappearance times of the three labels are shown in figure 6.6. The ratio of $|t_{before}|/t_{after}$ between the signals is similar (LimE-mRFPmars: 0.75; LimE-GFP: 0.73; LimEΔcoil-mRFPmars: 0.83), showing the nonsymmetric temporal evolution, with shorter appearance times. The ratio of mRFPmars-tagged LimEΔcoil is slightly shifted to higher values.

Next, actin foci with GFP-tagged LimE were measured in $\mathcal{S}$- as well as in $\mathcal{L}$-experiment (t_c = 450 ms, t_{exp} = 150 ms, t_{total}=180 s) configuration, as compared in table 6.2. Therefore at least 17 cells were measured for each setup. This set of experiments showed that the amount of foci detected within $\mathcal{S}$ or $\mathcal{L}$ configuration does not change significantly (p=0.3) and the ratio of $|t_{before}|/t_{after}$ is similar ($\approx$ 0.75).

The cells vary a bit in size ($\mathcal{S}$: 122 μm^2; $\mathcal{L}$: 107 μm^2), why the distance (l) from the focus to COM differs a bit ($\mathcal{S}$: 4.5 μm; $\mathcal{L}$: 4.0 μm). A normalization of l is useful and

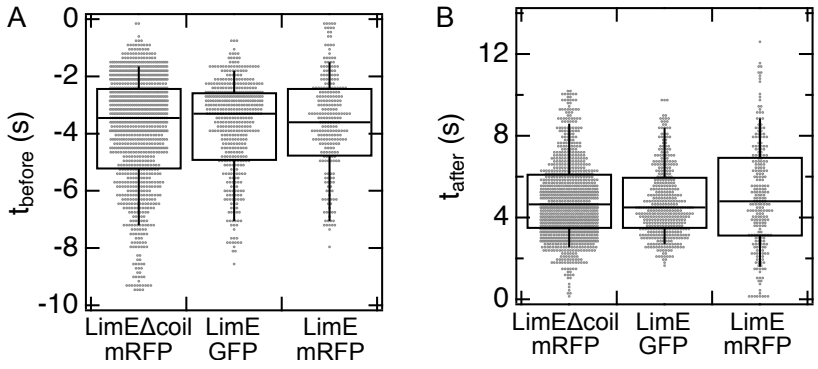

Figure 6.6: Dynamics of the actin signal - A: Time of the LimE-signal appearance, normalized to the maximum of the corresponding LimE-signal. No significant differences between the categories ($p > 0.1$). B: Time of the LimE-signal disappearance, in reference to the intensity maximum of the corresponding LimE-signal. No significant differences between the categories ($p > 0.1$)

will be fully described in the next chapter. 0.15 foci per minute appear per μm^2, thus these parameter are all independent of $\mathcal{S}$ or $\mathcal{L}$ experiment configuration as expected.

In addition the distance to the nearest foci, so called nearest neighbour (nn), was determined. nn shows significant ($p<0.01$) differences between $\mathcal{S}$ (0.8 μm) and $\mathcal{L}$ (0.5 μm) experiment conditions. As expected, the parameter nn is time dependent.

Table 6.2: Characterization of actin foci in AX2 - Analysis of the dynamic properties of actin foci in *D.d.* wildtype AX2. Actin visualized with GFP-tagged LimE as actin binding domain. Comparison of short ($\mathcal{S}$) and long ($\mathcal{L}$) term experiments for the following analysed parameter: Number of foci per minute (N_{Foci}), focus distance to the COM (l), normalized foci length (l_{norm}), distance to the nearest neighbour (nn).

Setup	N_{Foci}	l	l_{norm}	nn
Unit	$1/min$	μm		μm
$\mathcal{S}$	18.0	4.5	0.99	0.8
$\mathcal{L}$	16.7	4.0	1.06	0.5

6.3 Predicted actin foci distribution for various foci patterns in the contact zone

As already shown in the previous section, we have already shown, that the distance of a focus to the centre of mass (COM) is the best normalization for a parameter sensitive to random cell areas and -shapes. Therefore the contour of a idealised spherical cell, a circle, was used to hypothetically distribute foci-like spots in the contact zone and predict the influence of shape parameter on the foci distance distribution. As shown

in figure 6.7, experimental foci distances of AX2 are not equally distributed and show asymmetric tails.

In a first scenario (figure 6.8A), in a circle with R equal to 1, 10 circular sub-areas were added at relative incremental radial distance of 0.1 intervals and 90 foci-like points were equally distributed on each circle. As shown in figure 6.8E, the length is equal distributed from 0.1 to 1 and the distance to the nearest neighbour ranges from 0.007-0.07.

In a second scenario (figure 6.8B), in a circle with R=1, 10 circular sub-areas were added at 0.1 intervals and foci-like points were equally distributed on each circle with a distance to the nearest neighbour of 0.1. The distribution of the focal length shows a tail from 0.1 to 1. As expected the nearest neighbour distance is 0.1.

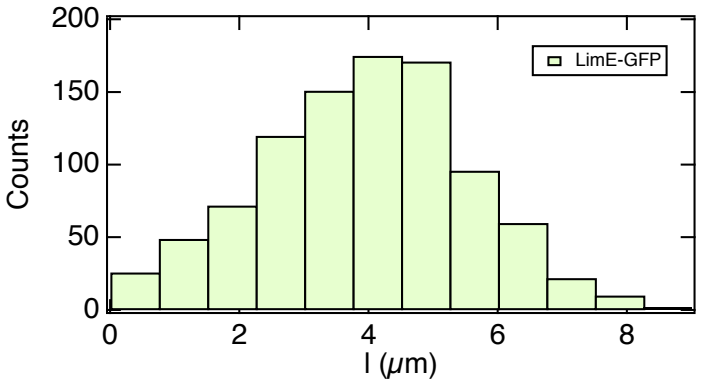

Figure 6.7: Distribution of foci distance - Histogram of the foci distance (l) of AX2+LimE-GFP in $\mathcal{L}$-experiment.

In a third scenario (figure 6.8C), the shape of the idealised cell was changed from circular to square. The amount of circles increased to 14, but the distance between the circles kept fixed at 0.1. As for scenario two, foci-like points were equally distributed on each circle with a distance to the nearest neighbour of 0.1. The distribution of the foci distance has a maximum at 1, as the experiments in figure 6.7 showed, with a distribution ranging from 0.1 to 1.4. As expected the nearest neighbour distance is 0.1.

To complete the series, a fourth scenario (figure 6.8D), was implemented. There, the first scenario was extended for the square. The foci distance is equally distributed up to value of one. The distribution of the nearest neighbour is similar to the one in the first scenario.

In addition the problem that the number of foci and distance correlates with the area of and location within the cell. Figure 6.8G shows the distribution of l depending on the radius of a circle matching the contour of the cell (R_{max}). In order to compare l, it was normalized to R_{max} and will be called l_{norm}. This normalization is shown in figure 6.8H for the four hypothetical foci distribution cases in 6.8G. In addition all four cases of G/H were merged, to show the advantage of the normalization.

Applying this normalisation to the results from the previous section, the result is a l_{norm} in $\mathcal{S}$ of 0.99. In $\mathcal{L}$-experiment conditions result is a l_{norm} in $\mathcal{L}$ of 1.06 thus both very similar.

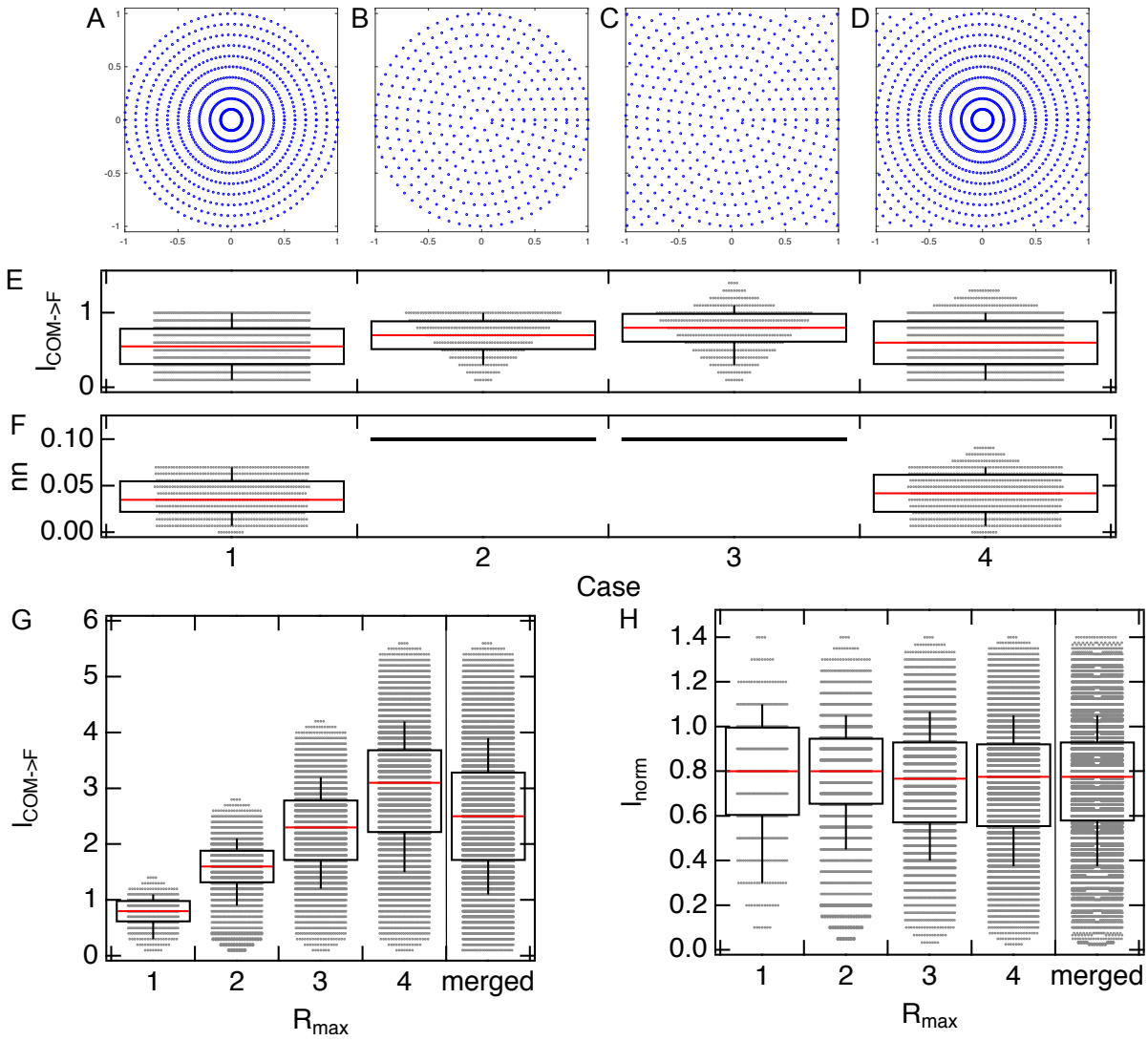

Figure 6.8: Predicted length distribution of actin foci - Model of an idealised single cell with an R=1, with an circular (A&B) or squared (C&D) shape. In addition the amount of foci per circle is equal (A&D) or limited to a certain distance (B&C, nn=0.1). Depending on the cases as shown in A-D, the foci distance (E) changes in their probability. In comparison the distance of the nearest neighbour in B&C is 0.1, as defined, and smaller for A&D. G shows the foci distance in dependence of the maximal radius R_{max}, as well as all data sets merged. For comparison the foci distance was normalized to R_{max} (H), as shown in the merged data set and the median is shown in red.

6.4 Key actin binding proteins and actin foci dynamics

6.4.1 Cumulative distribution of actin foci influenced of key actin binding proteins

In order to evaluate all foci of a category cumulatively, the probability density of all tracked foci was determined, as shown in figure 6.9. The foci were standardised to l_{norm}, so that the data can be compared with l_{norm} of figure 6.10D. Important phenomena are marked with blue arrow and categorised as following: 1) foci hotspots on $l_{norm} = 1$, 2) residence probability for $l_{norm} \geq 1.5$, 3) foci hotspots at $l_{norm} < 1$, 4) no foci close to the COM.

The foci in the wildtype AX2 are distributed over the entire range of angles and can be found both near the COM and on the periphery (l_{norm}=1-1.5). However, the majority of the foci appear on R_{max} at an angle of 30, 90, 160, 220 or 320° as marked by blue arrows; therefore the foci hotspots on $l_{norm} = 1$ (category 1) are distributed with a spacing of 50-60° each.

Inhibition of AX2 with CK666 changes the amount and local occurrence of the foci hotspots (see arrows), the probability of residence being much more homogeneously distributed over all angles and l_{norm}. Foci thus occur more often in the periphery ($l_{norm} \geq$1.5). Accumulation can be observed at 130 and 270° with an l_{norm} of 1.5 and 0.75 respectively.

The deletion of TalA in AX2 changes the local hotspot distribution, but leaves the residence probability of the foci similar to that of the wildtype. The majority of foci still appear at R_{max} with an angle of 60, 150, 240 or 330°; therefore the foci hotspots on $l_{norm} = 1$ (category 1) are distributed with a spacing of 90° each. A further accumulation can be observed at 350° with a l_{norm} of 0.75, thus category 3.

The deletion of ForA in AX2 shows two surprising influences on the regional distribution compared to the wildtype: I) the residence probability of the foci at R_{max} is significantly increased. The majority of the foci appear on R_{max} with an angle of 30, 150, 200 or 260° II) very few foci appear close to COM.

The wildtype AX3 shows similar local distribution of the foci compared to the wildtype AX2, but the residence probability of the foci at R_{max} is slightly lower and instead spread more outward until l_{norm}=2, with the majority of the foci appearing at l_{norm}=1.2. Only a few foci hotspots, such as the ones at 100 and 165°, can be observed.

The deletion of SadA shows similar local distribution of the foci compared to the wildtype AX3, but the residence probability of the foci is ubiquitously high with a slight hotspot at 80° at l_{norm}=1.5. No local accumulations are observed similar to the inhibition of CK666.

In summary, the foci are distributed over the whole ventral cell area. With the exception of TalA0, foci are observed from COM up to a l_{norm} of 1.5. The key actin binding proteins have a significant influence on the distribution of the foci hotspots and increase (TalA0, ForA0) or decrease (CK666, SadA0) local accumulations. These results match and add more detail to the KDE polar plot results shown in figure 6.9.

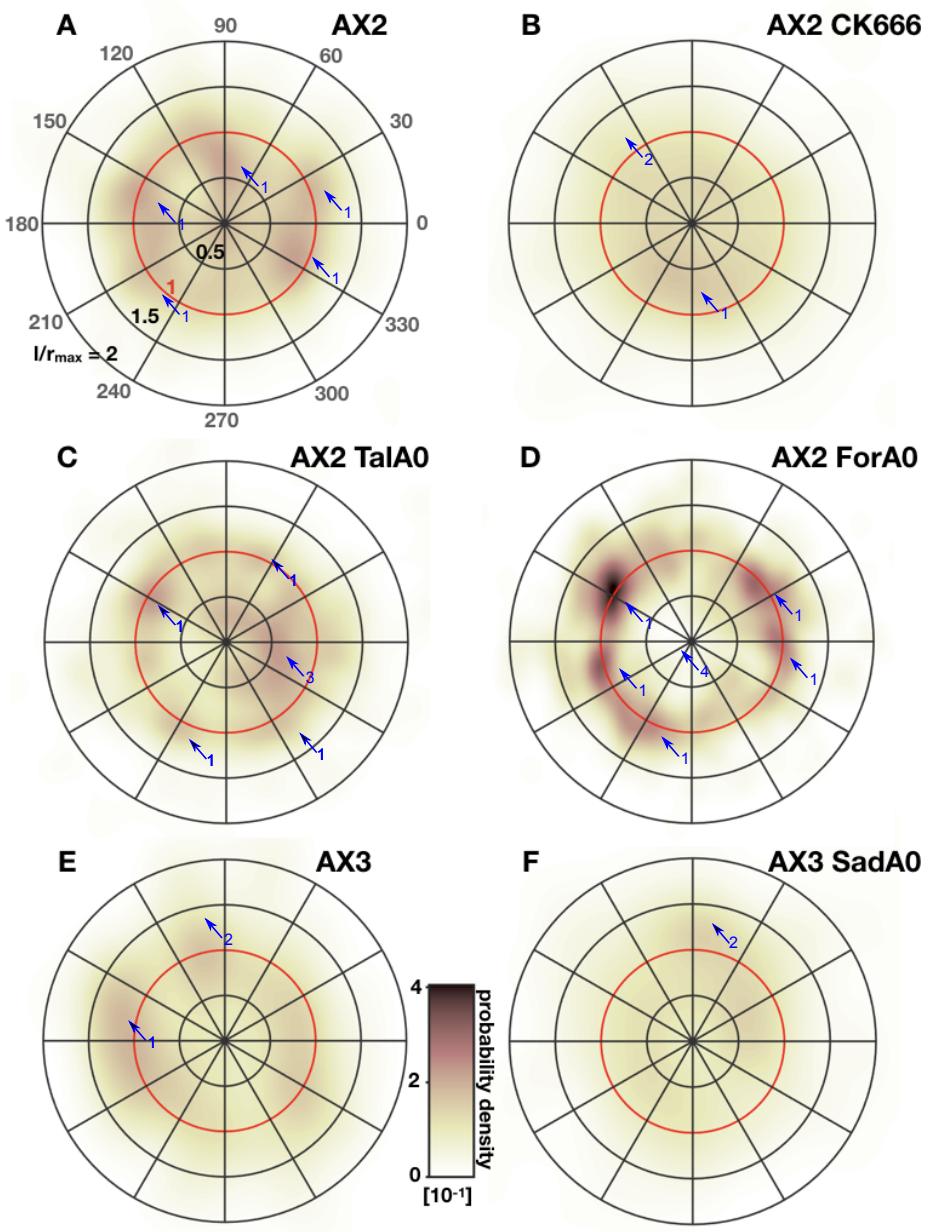

Figure 6.9: Probability density estimation of actin foci - Probability density estimation of all tracked actin foci in the wildtype AX2 (A), as well as the inhibition with CK666 (B), the deletion of TalA (C) or ForA (D). Furthermore the wildtype AX3 (E) and the influence of the deletion of SadA (F) was analysed. Foci are normalized to R_{max}. Numbering of the arrows refers to: 1) foci hotspot on $l_{norm} = 1$, 2) residence probability for $l_{norm} \geq 1.5$, 3) foci hotspots at $l_{norm} < 1$, 4) no foci close to COM.

6.4.2 Dynamics of actin foci influenced by key actin binding protein deletion/inhibition

In section 6.2, actin foci characterisation was introduced for various ABP and fluorophores in *D.d.* wildtype AX2 using TIRFM. This work will be extended in this section by further foci analysis in wildtype controls (AX3, DH1) and deletion/inhibition of key actin binding proteins (SadA0, CK666, TalA0, TalB0, ForA0), in the $\mathcal{L}$-experiment configuration for AX2. Measurements with *D.d.* wildtype AX3 and DH1 were performed in $\mathcal{S}$-experiment configuration.

AX2 and AX3 show a equal amount of foci (AX3: 17.0 min^{-1}, AX2: 16.7 min^{-1}, DH1: 15.5 min^{-1}; figure 6.10A), but the TIRFM based contact area varies strongly (AX3: 66.4 μm^2, AX2: 106.9 μm^2, DH1: 81.3 μm^2). Therefore the density of foci per area is also increased by almost a factor two for AX3 (0.26 $Foci/min\ \mu m^2$) in comparison to AX2 (0.15 $Foci/min\ \mu m^2$) and DH1 (0.19 $Foci/min\ \mu m^2$). SadA0 cells in an AX3 background show a strong increase in the amount (33.5 min^{-1}) of foci and in the contact area (95.7 μm^2) as well as in the density per area (0.35 $Foci/min\ \mu m^2$). The inhibition of Arp2/3 in AX2 with CK666 leads to a decrease in the amount of foci by a factor of 2 (8.8 min^{-1}) and in the contact area by a factor of 3 (38.1 μm^2), so that the density per area (0.23 $Foci/min\ \mu m^2$) increases in comparison to corresponding wildtype AX2. TalA0 cells in AX2 background show an equal amount of foci (16.2 min^{-1}), but the contact area increases, which decreases the density to 0.13 $Foci/min\ \mu m^2$. ForA0 cells in an AX2 background show only a slightly smaller amount of foci (15.0 min^{-1}), but the contact area decreases by 35%, which increases the foci density per area to 0.21 $Foci/min\ \mu m^2$. In conclusion the axenic strains show different contact areas and the deletion of the key actin binding proteins influence the size of the cell and the number of foci and thus the density per area, see table 6.3.

In addition the focal distance to the nearest focus/neighbour (nn) of all foci within a time stack was calculated. This value ranges from 0.4 to 0.6 μm and changes only significantly for ForA0 cells (0.4 μm), therefore it does not show similarities to the density of foci per area.

Besides spatial aspects, temporal aspects were also analysed, like the half lifetime (lt_{50}) resulting from appearance and disappearance at half maximal intensity. AX2 and AX3 show very similar foci half lifetimes of 10 s, while DH1 shows a strongly shortened half lifetime of 7.95 s. As shown in figure 6.10B, the half lifetime decreases in the case of SadA0 (9.6 s) in comparison to AX3 (10.2 s) and increases for CK666 (13.05 s) as well as TalA0 (12.13 s) in comparison to AX2 (10.35 s). ForA0 cells show no significant differences in the half lifetime. TalB0 cells showed too few foci for a statistical evaluation. Detectable foci showed a increased lifetime of 16.2 s.

Besides lt_{50}, the positional shift was also tracked and determined, l_d. Foci of cells with a deletion of SadA (92 nm) move a bit further than the corresponding foci of the wildtype AX3 (65 nm), which is comparable to the wildtype DH1 (65 nm). Foci of the wildtype AX2 show a slightly higher shift (92 nm). The inhibition of Arp2/3 and the deletion of TalA does not influence this length/scale. Foci of ForA0 cell show the highest shift with 130 nm. A further parameter was the velocity ($V_F = l_d * lt_{50}$) of foci,

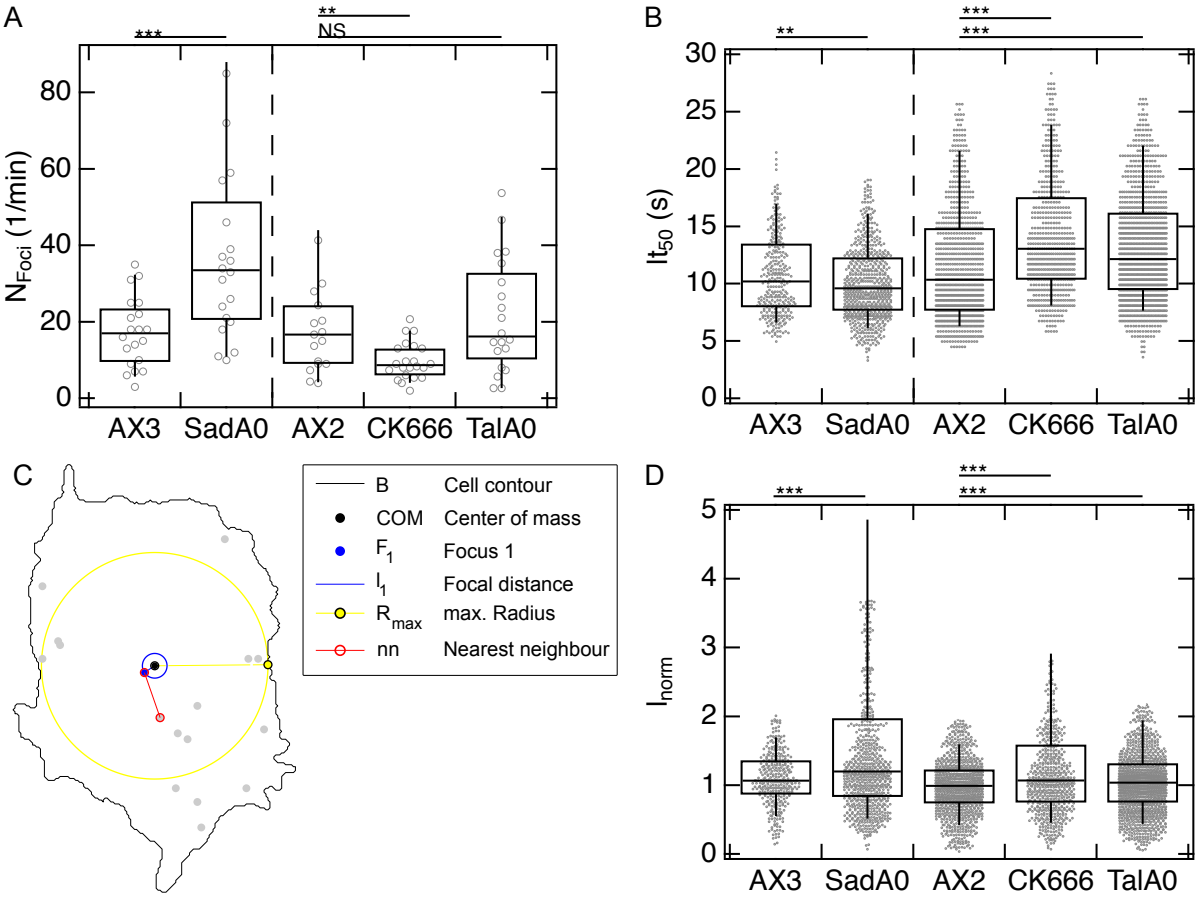

Figure 6.10: Actin foci dynamics upon manipulation of key actin binding proteins - A: The amount of foci increases significantly from SadA0 to the WT, in comparison CK666 reduces the amount of foci. B: SadA0 show a decrease in lifetime, in contrast CK666 and TalA0 show an significant increase. C: As example a TIRFM-based contour of an AX3 cell showing the assessed parameter: Boundary ($B(t_1)$) with focus 1 (F_1, blue) in comparison to the centre of mass ($COM(t_1)$, black). Further foci within the time stack are shown in grey. In addition, the length of F_1 to COM (focal distance, l) as well as the nearest neighbour (nn) shown as an example for F_1. Radius (R_{max}) of the biggest circle, which is enclosed within the cell contour, with COM as centre. D: Focal distance (l_{norm}), distribution of l normalized to R_{max}. SadA0, TalA0 and inhibition with CK666 show moderate but significant increase of foci appearing at the periphery.

which ranges for wildtype cells from 7.6 to 9 nm/s. SadA0 (10.7 nm/s) and ForA0 (10.2 nm/s) cells show a significant increase of the foci velocity, in comparison to the corresponding WT (AX3: 8.0 nm/s; AX2: 9.0 nm/s). The inhibition of Arp2/3 and the deletion of TalA does not influence the foci velocity.

An example of a AX3 cell is shown in figure 6.10C, with the first appearing foci F_1 at t_1 in blue, the centre of mass (COM) of the cell and its contour B(t_1) in black as well as the biggest centered circle with the radius R_{max} in yellow. The distance (l) between F_1 and COM was normalized to R_{max}, as described in section 6.3. With the help of this normalization it is possible to evaluate the distribution of the foci independent of the morphological changes caused by the manipulation of the key actin binding proteins. Results of l_{norm} (l/R_{max}) are shown in figure 6.10D and in table 6.3. This parameter shows that foci of SadA0 cells have a preference to appear more in the periphery (SadA0: 1.20) in comparison to the WT (AX3: 1.07). Foci of AX2 cells seem to be more localised in the inner part of the cell (AX2: 0.99), although not significantly compared to AX3. Inhibition with CK666 as well as deletion of TalA or ForA leads foci appearing more in the periphery. The inhibition with CK666 as well as SadA0 cells show a broadening of the distribution. These results match and add more detail to the KDE polar plot results shown in figure 6.9.

Table 6.3: Overview of actin foci under key actin binding protein modulation in different *D.d.* cells - TIRFM-based median of the following parameter: amount of foci within a minute (N_{Foci}), area of the cell (A_{cell}), distance to the nearest neighbour (nn), half lifetime of the foci (lt_{50}), normalized distance of the foci to centre of mass in relation to R_{max} (l_{norm}) as well as the velocity of the focus (V_f). All experiments were done in $\mathcal{L}$-experimental configuration, besides the measurements with AX3 and DH1 backgrounds where an $\mathcal{S}$-experimental configuration was used.

Parameter	**AX3**	SadA0	**AX2**	CK666	TalA0	ForA0	**Ref.DH1**
Setup	$\mathcal{S}$	$\mathcal{S}$	$\mathcal{L}$	$\mathcal{L}$	$\mathcal{L}$	$\mathcal{L}$	$\mathcal{S}$
N_{Foci} $(1/min)$	17.0	33.5^{***}	16.7	8.7^{**}	16.2^{NS}	15.0^{NS}	15.5
A_{cell} (μm^2)	66.4	95.7^{***}	106.9	38.1^{***}	120.7^{***}	69.9^{***}	81.3
nn (μm)	0.6	0.5^{NS}	0.5	0.5^{NS}	0.4^{NS}	0.4^{***}	0.4
lt_{50} (s)	10.2	9.6^{**}	10.35	13.05^{***}	12.15^{***}	10.35^{NS}	7.95
l_{norm}	1.07	1.20^{***}	0.99	1.07^{***}	1.04^{***}	1.06^{***}	1.18
$V_F(nm/s)$	8.0	10.7^{***}	9.0	8.2^{NS}	8.0^{NS}	10.2^{**}	7.6

6.4.3 Validating the tracking software

To validate the optical foci tracking routine, as an example a movies of a WT cells and deletion/inhibition of key actin binding proteins were tracked for actin foci manually (M) with the Fiji Plug-in *Manual Tracking* in addition to custom made Matlab-based Tracking, software (S), introduced in chapter 3.6.3. Each focus was tracked, in regards to locus and times of appearance and disappearance. The following parameter could be analysed: Number of foci (N_{foci}), lifetime of the focus (lt) and positional shift of the focus (l_d), as shown in table 6.4.

Table 6.4: Validating the custom-made tracking software - As an example cells of each category were used in addition to the automated tracking by the software (S), manual (M) tracking with a Fiji Plug-in was applied. The following parameters were analysed: Number of foci (N_{foci}), half lifetime (lt_{50})/ lifetime (lt) as well as the positional shift of the focus (l_d). The ratio (S/M) of the results measured in S and M are shown, strong differences highlighted.

	N_{foci} $(1/min)$			$lt_{50}(s)$	$lt(s)$		l_d (nm)		
	S	M	S/M	S	M	S/M	S	M	S/M
AX3	16	13	1.2	6.975	8.4	0.8	146	202	0.7
SadA0	26	24	1.1	13.05	13.43	1.0	131	228	**0.6**
AX2	50	47	1.1	5.85	7.65	0.8	76	176	**0.4**
CK666	25	29	0.9	16.2	12.6	**1.3**	113	76	**1.5**
TalA0	22	28	0.8	7.65	13.05	**0.6**	46	131	**0.4**
ForA0	50	41	1.2	11.25	13.5	0.8	101	176	**0.6**
Ref.DH1	13	5	**2.6**	9.15	11.25	0.8	0	45	**0.0**

The number of tracked foci with the software differs by 10-20% depending on the label, with the exception of DH1.

In the manual tracking, the first and last frame, where a focus can be seen was used to calculate the lifetime. In comparison the software tracked the foci when the intensity reaches 50% of the total intensity in comparison to the background. Foci tracked with the manual software thus are longer by 20-40% in duration. In case of SadA0 both versions of tracking almost match and slight discrepancies are found for the deletion of TalA and the inhibition with CK666, were the tracking showed a longer or shorter lifetime.

The automated software uses the centre of mass calculated from the contour of a single focus, while in comparison manual tracking only detects the centre of mass of a focus, so that the error of l_d ranges from 30-60%. In addition the timeshift from the custom made software and lt from the manual tracking, additionally contributes to overestimation of the detected positional shift.

6.5 Actin foci and clathrin-mediated endocytosis

Within this set of experiments clathrin puncta (GFP-tagged ClcA) in combination with actin foci (mRFPmars-tagged LimEΔcoil, from here onwards only named LimE) were observed in an AX2 background. Co-localization studies were performed in $\mathcal{L}$-experiment configuration; 29 cells were analysed and subsequent median values are given.

ClcA appears 10.9 s before LimE (figure 6.11B) and also disappears 12.2 s before LimE (figure 6.11D). The maxima of the two signals are shifted by 15.3 s (figure 6.11C), as summarised in figure 6.11A. Within the tracking, we can decide between 3 cases: I) clathrin puncta appear before actin foci, which is the common one II) clathrin puncta appear after actin foci III) actin foci appear independent of clathrin puncta. ClcA and LimE show a spatial coincidence of 81.2%, and 75% of all ClcA punctae show up before LimE while 25% of ClcA appearing after LimE, as summarized next to figure 6.11E. ClcA has a half lifetime of 14.2 s. There is no significant difference between ClcA appearing before or after LimE (p=0.86, figure 6.11E).

The experiments showed that LimE appearing after ClcA has a lt_{50} of 17.0 s and LimE appearing after ClcA 17.5 s, which is not significant (p=0.88, figure 6.11D). In

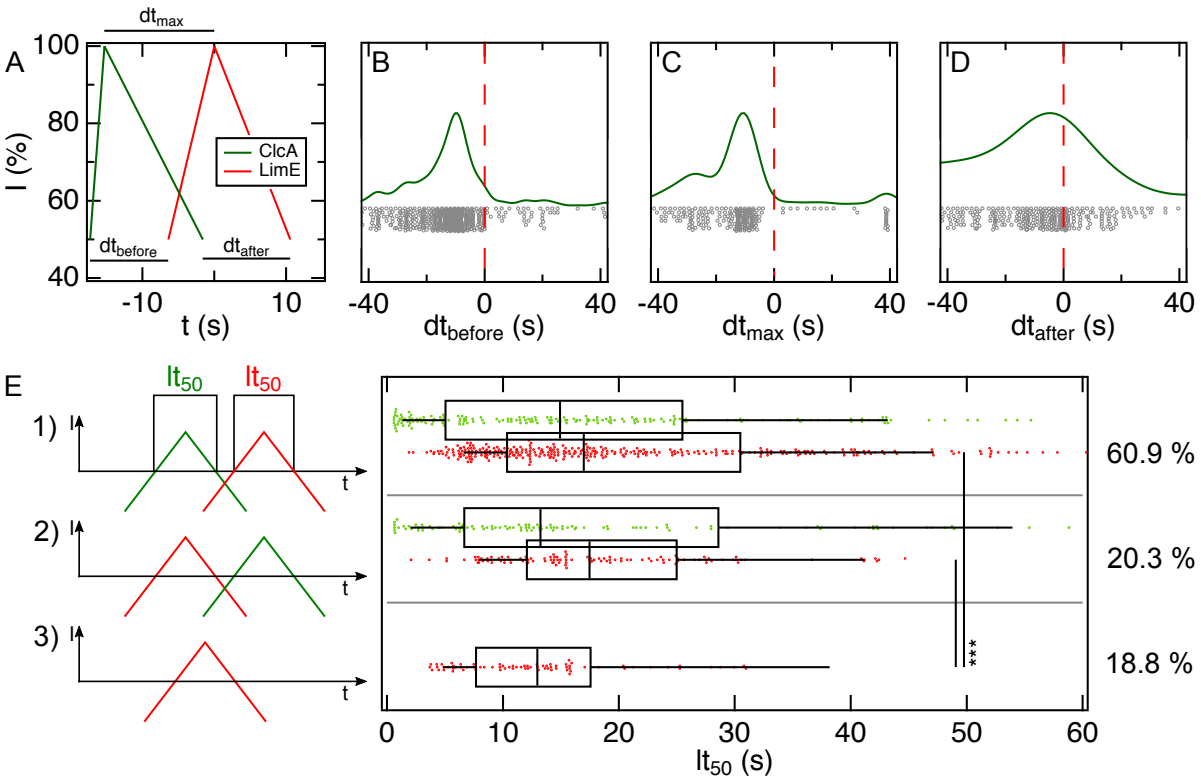

Figure 6.11: Co-localization studies of actin foci and clathrin pits - A: Summary of the ClcA (green) and LimE (red) signal, based on median values of the experiments. B to D show the timeshift, as shown in A, of ClcA signal to the corresponding LimE signal (red line). E: Half lifetime of actin (red) and clathrin (green) if 1) clathrin appears before actin, 2) actin appears before clathrin or 3) actin appears without clathrin.

contrast, LimE appearing independent of ClcA, has a reduced lifetime of 13.0 s, which means that there are two types of actin foci, with different functions.

The next focus were the substructures within the contact area by combining bright field microscopy for cell identification with RICM for contact area dynamics and dual colour TIRFM for actin-clathrin dynamics as shown in 6.12A. We thus combined RICM to analyse the membrane movement with TIRFM to track fluorescence-tagged actin foci and clathrin punctua as shown for an individual, typical focus in figure 6.12B/C. Previous results from conference precedings using this approach already suggested a dual role of actin foci in adhesion and endocytosis[158]. The total observation duration is 3 minutes while the time resolution is 0.4 fps to reduce bleaching effects. In figure 6.12C the RICM intensity decrease indicates that the membrane approaches the substrate (grey scale, from 30 s on) at the same location where two clathrin spots appear (40 s and 90 s) and afterwards an actin focus (105 s). Actin disappearance (115 s) therefore hints to the internalization procedure of the upper clathrin spots in the form of an endosome (105 s), while the originally actin free clathrin structure persists longer. The process is completed by retraction of the membrane from the substrate (130 s onward) even though both new actin or clathrin structures appear occasionally in the field of view and might initiate a new cycle.

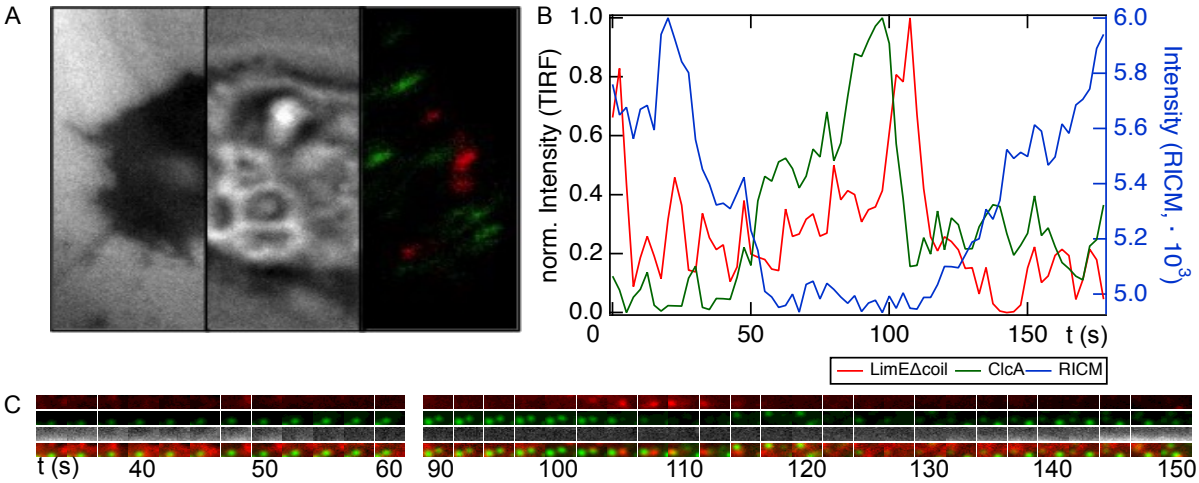

Figure 6.12: Overview of membrane movement of actin foci - A: Collage of RICM, BF and dual label TIRFM images of *D.d.* cells. B: Local adhesion analysis: combination of TIRFM and RICM for observation of clathrin and actin activity and contact area increase - Intensity profile of actin (LimEΔcoil-mRFPmars) and clathrin signal (ClcA-GFP) in comparison to the RICM intensity reflecting membrane height changes (blue). C: As an example, the actin focus from B is shown as a image series with LimEΔcoil-mRFPmars, ClcA-GFP and RICM. Merge of the two TIRFM intensities over time in last row.

In the setup of experiment 21 cells were measured. As shown in figure 6.13A, the membrane moves towards the substrate 26 s before the actin foci appears. Figure 6.13B shows that the membrane is lifted 43 s after the foci disappears. Furthermore the intensity of the RICM signal was analysed for foci with and without ClcA signal, as shown in figure 6.13C. For both categories two groups can be found, one close to the substrate and a second one further away.

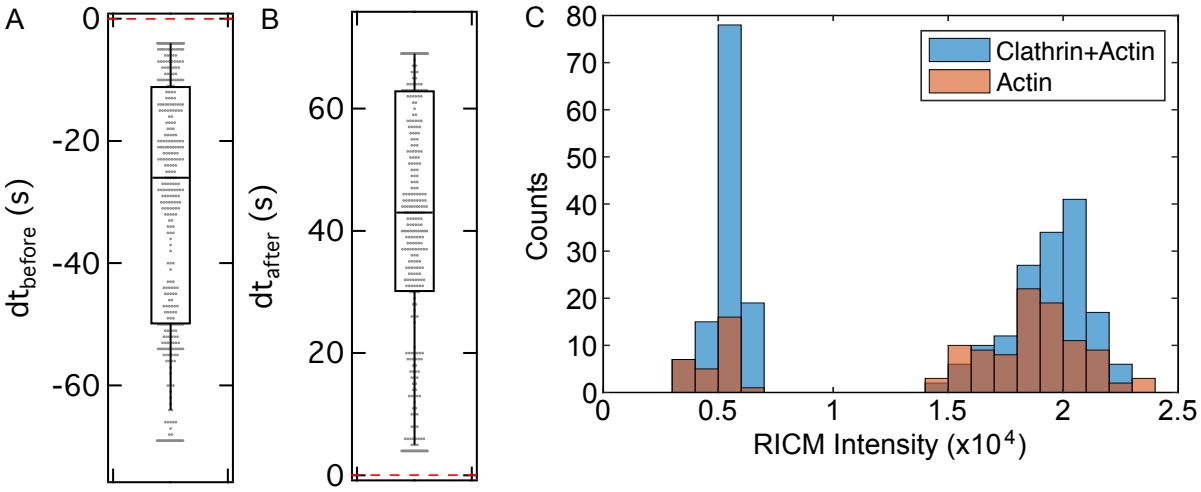

Figure 6.13: Membrane movement at actin foci - A: Timeshift between the appearing actin signal and the membrane movement to the substrate.[158] B: Timeshift between the disappearing actin signal and the membrane movement from the substrate. C: Histogram of the membrane intensity for actin foci with (blue) and without (orange) clathrin co-localization.

A quantitative co-localization analysis reveals 81.2% spatial coincidence. Thus we can state that clathrin and actin mainly appear sequentially but sometimes also independently or simultaneously. Note that 81.2% coincidence values are both close to previous findings of 82% [159], but also the temporal clathrin-actin shifts resemble recent findings by Amato et al.[7]. In summary, actin foci as well as clathrin structures strongly coincide, but a small subpopulation of each structures can be found to exist independently. It can be assumed that the two clathrin populations that are at different distances from the surface also have different functions.

7 Discussion

7.1 Cell-substrate adhesion of *D.d.* influenced on micro-patterns

Adherent mammalian cells possess dedicated adhesion complexes with specialised adhesion proteins. Surfaces need to be extensively pre-treated to allow these cells to adhere. In contrast, *Dictyostelium discoideum* (*D.d.*) is able to adhere to almost all surfaces especially due to glycoprotein-mediated non-specific adhesion, mainly by Van der Waals interactions[62]. A common method of passivating a substrate to block cell adhesion is to coat the substrate with macromolecular "brushes" made of polyethylene glycol (PEG)[160, 161]. In the present work, we used 30% PEG gels, with a 1 μm layer thickness, so that the adhesion of *D.d.* has been successfully blocked completely. This massive layer thickness prevents Van der Waals interactions between the cell and the glass surface. Therefore hiding the glass substrate properties from the cells. It is assumed that even a thin layer ($\approx$ 10 nm [162]) of PEG is sufficient to block the adhesion of *D.d.*: micro-structuring with PEG brushes requires extensive laboratory equipment (photolithography) as described by Tzvetkova-Chevolleau et al.[163] as well as special substrates and expensive chemicals such as initiator or cross-linker. PEG-gels can be produced with much less effort and equipment. The big advantages of the gel-based method are the use for micro-patterned structures with sharp edges as well as the use of standard microscope cover glasses.

This research has however shown that several aspects give *D.d.* the ability to adhere to PEG gels. First, adhesion and thus also PEG repulsion depends on the developmental stage of *D.d.*.

Vegetative cells always showed lower adhesion on PEG than on glass, but the strongest effects were found with developed cells. The wildtype AX4 is not able to adhere to PEG in its developed state and therefore migrates only on glass. In contrast, vegetative wildtype AX4 cells can adhere and migrate on PEG.

AX2 wildtype cells showed an increase in adhesion property with increasing developmental stage on PEG. Earlier studies[121] could already observe the phenomenon of development-dependent cell-substrate adhesion changes in the wildtype AX3. The adhesion changes matched the ones upon SadA and SibA loss, and were supported by mRNA expression level reductions. This suggests that the adhesion apparatus adapted to chemotaxis during development. Thus in the developed state, *D.d.* reduces adhesion and switches to directed migration to increase chemotaxis efficiency. This requires extensive reorganisation of the cytoskeleton and adhesome to overcome specific adhesion forces, as exemplarily shown in figure 7.1 via step spectroscopy[41].

The step force decreases after starvation started (3 h) and increases slightly during later development (6 h). In contrast, the number of steps decreases from vegetative state (0 h) to later development (6 h), but still steps can be detected. The treatment with Latrunculin shows only a few steps in contrast to developed cells, which shows that the involvement of the cytoskeleton in cell-substrate adhesion is essential. Wang et al.[164] attributed cell-cell contacts responsible for the symmetry break during early streaming, therefore switching from cell-substrate to cell-cell contact signalling. Further research is needed to clarify this phenomenon.

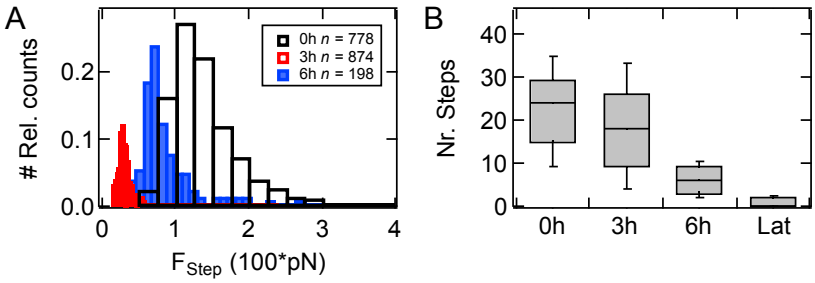

Figure 7.1: Step analysis of developed *D.d.* - A: Tether force and B: Amount of tethers from SCFS of AX3 WT cells on a glass surface during starvation-induced development (switch from medium to PB buffer at t= 0 h). 5 μM Latrunculin A (LatA) treatment is shown as reference. Printed with the permission of the publisher[41].

It is noticeable that developed AX4 cells cannot adhere to PEG gel surfaces, whereas developed AX2 cells can. SCFS measurements show that maximum adhesion forces, F_{max}, for AX2 cells of glass and PEG-gel surfaces are almost identical, which is consistent with the results of the bulk assay on micro-patterned substrates; exemplary comparison of labelled cells can be found in figure 7.2.

Secondly, the adhesiveness of *D.d.* on PEG gels depends strongly on the examined axenic background. SCFS-based F_{max} seems to be a better indicator than W_{adh} for comparison to the optically determined cell fraction found on different types of surfaces when applied to a micro-structured substrates. A summary of all F_{max} measurements is shown in table 7.1. In the past, several studies have reported on strain-dependent behaviour of *D.d.*. The periodic movement of slugs leads to an optical density wave. Where for example $\approx$ 90% of all measured slugs of the wildtype NC4 showed waves, in comparison no waves could be detected in the wildtype AX3[165]. This phenomenon could for example be observed in multicellular pattern formation between NC4 and AX2[166].

Single cells also show phenotypic differences depending on their strain, for example in the localisation of the actin polymerisation regulator SCAR and the motility of vegetative *D.d.* cells[167] (NC4A2 vs AX3). Bloomfield et al.[18] pointed out that certain genome segments are duplicated within different wildtype strains, therefore explaining the strong phenotypical variation for different axenic strains. One central hypothesis for the adhesion variability observed in the present thesis is linked to the expression of talin[168], which is involved in cell-substrate adhesion as an actin-anchoring, adhesion

site scaffolding, cytoplasmic protein, linked to transmembrane adhesion proteins[69]. McCann et al.[169] showed that strongly adhesive surfaces like glass strongly depend on actomyosin contractility for detachment of single cells, while weakly adhesive substrates like the PEG brushes instead rely on talin signalling and thus control small adhesive forces. While the talin gene sequence in AX2 cells is a full-length homologue of mammalian talin[168], it was shown for AX3 and thus their derivates such as AX4 that the talin A gene is present in a shortened form, which is however not comparable to a talin-null mutant: Tarantola et al.[121] studied adhesion properties of the wildtype AX3 and talin null cells by SCFS and microfluidic shear force-assay. There, vegetative wildtype AX3 showed significantly different adhesive properties compared to AX3 with a talin A deletion.

Table 7.1: Summary of the results from SCFS - Median of adhesion force (F_{max} in nN) for vegetative and developed wildtypes (WT) AX2 and AX4 on glass or PEG substrate, with additional single or double fluorescence tags of the actomyosin or microtubule cytoskeleton. In general there is a significant difference between Glass and PEG, except for the developed AX2 cells, which is shown in orange.

WT	Label		vegetative		developed	
			Glass	PEG	Glass	PEG
AX2			3.0	0.2	1.6	0.5
AX2	LimE		3.6	0.9	3.5	1.0
AX2	MyoII		4.5	0.1	4.1	0.5
AX2	LimE	Tub	3.2	1.0		
AX4			2.1	1.4	3.6	0.3
AX4	LimE		2.4	0.4	1.5	0.3
AX4	LimE	CorA	3.3	0.4	2.0	0.1

Instead, it is assumed that the stiffness of the membrane is affected, since talin is coupled to the actomyosin cortex together with SadA and SibA, itself controlling localisation of SadA[84, 170]. It has already been shown with RICM in the past, that cells react to different surface compositions with modulation of the actomyosin cortex[66, 169]. Future AFM studies could specifically characterise cortical tension and membrane bending moduli of AX2 and AX4 cells lacking talin in a similar way, combining AFM and RICM. For the present study however the different reaction of the two strains to surface properties could be attributed to the truncated talin in AX4.

Thirdly, the adhesiveness of *D.d.* is influenced by fluorophores connected to the actomyosin network. This finding cannot be generalised and needs to be studied for each combination of fluorophores and cytoskeletal components individually. In vegetative AX4 cells on glass, the expression of the labelled actin binding domain does not influence the adhesion strength, whereas in AX2 it leads to a significant increase of adhesion

strength (see table 7.1). The same applies to the labelling of myosin in AX2. In addition, double labelling *D.d.* cells causes a significant increase of F_{max} as compared to the single label, as long as actin or myosin components are involved. Tubulin labelling did not affect adhesion to glass. Leonhardt et al.[150] already showed comparable results of adhesion properties for the tagged α-tubulin in *D.d.*. On PEG the influence of labelling cytoskeletal components is less conclusive: for example, adhesion force of AX2 can be increased by the expression of LimE, but not by labelling myosin II. For AX4 labelling even leads to decreasing adhesive forces. Thus strongly adhesive surfaces like glass strongly depend on unperturbed actomyosin contractility to regulate cellular adhesion, which otherwise is increased. Weakly adhesive substrates like the PEG gel instead rely on more subtle effects, as already suggested in [169].

The strongest effect was found in developed AX2 cells between PEG and glass. F_{max} increases when fluorescent markers of actin and myosin are expressed.

Expressed fluorophores may influence binding sites. Similar observations could be made with other markers or in other cells in a similar context: Flores et al.[171] recently showed that Lifeact, a marker for F-actin, can induce dose-response artefacts at the cellular level, most likely due to reduced binding of cofilin to actin filaments. In rat muscle cells, GFP expression was shown to interfere with actin-myosin interactions[172]. In breast cancer cells, GFP expression alters the expression of proteins responsible for protein folding, cytoskeletal organisation or the cellular immune response[173]. In *D.d.* it was shown that GFP-tagged myosin can save all myosin-null cell defects[174] in regards to chemotactic migration.

In summary, adhesion of *D.d.* cells to PEG gel shows a dependency on the axenic background, the developmental stage and the fluorescent protein marker expression, but it is also obvious that further characterisation of unspecific and specific contributions to adhesion both from substrate and the cellular adhesome is necessary. This should

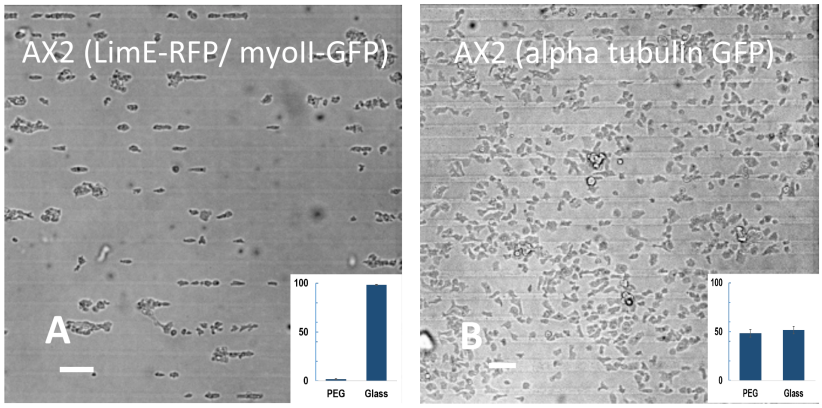

Figure 7.2: Developed AX2 cells expressing fluorescent label - Micrographs of developed AX2 cells expressing both LimE-RFP and myoII-GFP (A) and α-tubulin-GFP (B) on the micro-patterned substrate taken 10 min after plating. Insets: relative coverage of cells on PEG-gel and glass stripes. (Scale bar: 50 μm)[43]

motivate more studies on individual fluorophores and cytoskeletal components. For example, developed AX2 cells with fluorescent markers for tubulin on micro-structured substrate show similar adhesion properties on PEG and glass, as shown in figure 7.2, thus comparable to the WT.

7.2 Adhesion strategies of *D.d.* - a force spectroscopy study

In this project the cell-substrate adhesion of vegetative *D.d.* on model surfaces was investigated using AFM-based SCFS to identify the relevant forces involved in amoeboid adhesion. The combination of TIRFM and AFM did not provide the desired results, as the optical resolution in both xy- and z-direction were insufficient.

Within this work SCFS was used to measured adhesion properties of vegetative *D.d.* in combination with a multilayered substrate of Si/SiO_2, whose adhesion properties can be tuned in a controlled manner. We found that the general adhesion markers (F_{max}, W_{adh}) increase with decreasing SiO_2 layer thickness, thereby confirming that long-range V.d.W. interactions are significantly involved in the adhesion of *D.d.*. This result coincides with earlier work on the adhesion of the bacterium *Staphylococcus carnosus*[130, 175] and the eukaryotic microalga *Chlamydomonas reinhardtii*[176] on the same set of model substrates. Additionally Loomis et al.[62] already predicted that *D.d.* adhesion would rely on V.d.W. forces in the pN to nN range, which is consistent with our results.

AFM-based SCFS was used in all three projects. The shape of adherent cells can be assumed as sessile droplets[177], which is confirmed by experimental observations. We were able to analytically reproduce and numerically simulate the retraction part of the

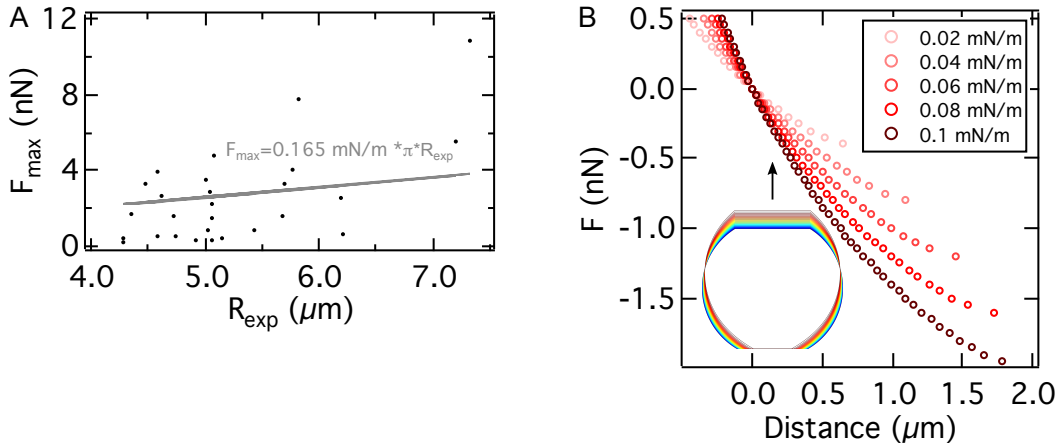

Figure 7.3: Characterisation of FD curves - A: SCFS-BF microscopy combination for single cell radius R_{exp} versus F_{max} detection. Linear regression (grey) yields an adhesion energy per unit area of AX2 of 0.165 mNm^{-1}. B: Computational FD curves up to the critical adhesion force for different adhesion energies per unit area w. The inset shows the shape evolution during pulling (increasing pulling forces from blue to red).

force-distance curves up to the critical adhesion force, both for cells with and without the main adhesion molecule SadA. This indicates that in the continuum part of the FD curve the adhesion energy density w describes the adhesion independent of the binding and unbinding kinetics of specialised binding molecules.

The shape of the curve depends on elastic parameters of the cell cortex and a simple approximation of the model leads to the critical adhesion force $F_{crit} \approx \pi w R_{susp}$ with the adhesion energy per unit area w and the radius of the cell in suspension R_{susp}. The results from the SCFS measurements also generally follow the prediction of the linear F_{crit}-dependence on R_{exp} (figure 7.3A). The critical adhesion force is independent of the cell mechanics, making it the most appropriate variable to observe the adhesion strength w, as shown in figure 7.3B, where the shape of the curve is changed significantly with w and also the cell shape upon pulling.

7.2.1 Role of V.d.W. forces and the hydrophobic effect

V.d.W. forces are rather weak, but not negligible: they are equally distributed and a function of the entire interacting surface, so that they influence both local fluctuations in the distance between ventral membrane and the substrate as well as the 'position' of adhesion clusters. This can be a factor influencing adhesion and migration dynamics.

In addition, we observed that the maximum adhesion forces is influences by the wettability of the surface, see table 7.2. This supports the Lifshitz theory that the V.d.W. attraction in an aqueous solution increases when the dielectric constants of the cells and the surface are equal[178].

In contrast to the large differences in the adhesion strength, no differences in the spreading behaviour could be proven. This shows that the system is dominated by mechanical homeostasis. Similar results were obtained with control measurements on glass surfaces with adhesive forces being consistent with earlier measurements[151]. It could be expected that the hydrophilic treatment of the surface would increase the wettability and as a consequence the spreading behaviour. However, this could not be confirmed for *D.d.* on the model substrates. It can be assumed that the actomyosin cortex generates active contractile forces and controls cortical tension to maintain the homeostasis of the spreading behaviour. Similar results have already been described using fluorescence microscopy[169] and RICM[164]: both studies have shown that a balance between protrusive and adhesion forces for *D.d.* exists which allows shape stabilisation on a variety of substrates. In contrast, multicellular development with its cell-cell contacts significantly disturbs this balance leading to desensitization for substrate properties.

It can be expected that adhesion energy density w and consequently the critical adhesion force contribute to V.d.W. interactions, whereas it is unknown how the stochastic unbinding events influence the second part of the FD curve. Therefore, a step analysis was carried out in addition to the global adhesions parameters. In summary, while step properties like step force, pulling length and step length do not show a clear trend, neither for the model substrates nor for the change of the wettability. The amount of steps per FD curve show similarities to the surface properties so that mainly the number of adhesion clusters seems to be affected.

Table 7.2: Overview of global adhesion properties based on SCFS- Summary of all measured cell types, substrates and conditions used in this study. References for literature values are added. Medians of maximal adhesion force (F_{max}) and adhesion work (W_{adh}) are given. In addition the adhesion energy density (w) is shown. Reprinted with the permission of the publisher[41].

Cells	Substrate	Conditions	$F_{\max}$ (nN)	W_{adh} (fJ)	w (mNm^{-1})
AX2[150]	Glass	PB	7.7	16.5	
AX3[121]	Glass	PB	7.6	27.3	
AX2	*N-SiO*$_2$	PB	5.4	10	0.34
AX2	*T-SiO*$_2$	PB	3.7	5.9	0.26
AX3	*T-SiO*$_2$	PB	3.7	11.6	0.24
AX3	*T-SiO*$_2$	PB+5 mM KCl	3.5	3.9	0.22
AX3	*T-SiO*$_2$	PB+20 mM KCl	2.1	1.0	0.13
AX3	*T-SiO*$_2$	PB+5 mM $MgCl_2$	1.9	5.0	0.12
AX3	*T-SiO*$_2$	PB+20 mM $MgCl_2$	1.8	1.0	0.12
AX2	*N-OTS*	PB	3.1	5.5	0.20
AX2	*T-OTS*	PB	2.1	2.2	0.13
AX3	*T-OTS*	PB	2.5	3.8	0.13
AX3+αM	*T-OTS*	PB	1.4	1.5	0.09
AX3+*sadA0*	*T-OTS*	PB	0.7	0.8	0.03
AX3+*sadA0*+αM	*T-OTS*	PB	0.5	0.3	0.02
AX3+LatA[121]	Glass	PB	0.2	0.2	

7.2.2 Influence of the electrostatic interactions

After the systematic investigation of the influence of long-range V.d.W. forces, electrostatic interactions that could control the adhesion forces were analysed. The soil in which *D.d.* lives in is a heterogeneous, three-dimensional environment, that is very porous with cavities filled with liquid. The surrounding material is frequently dissolved, which may result in a significant change of the ionic strength. In order to assess to what extent electrostatic interactions could contribute to *D.d.* adhesion, the ion content of the buffer was modulated.

Both the surface of the model substrates[130] as well as of a *D.d.* cell[179], in the corresponding development state, are negatively charged in the buffer. The maximum adhesion force decreases with increasing ionic strength (see table 7.2), which confirms data by Socol et al.[179]. Note that the osmotic pressure in the gap between cell and substrates is proportional to the ion concentration of the bulk solution, as these cells form no isolating monolayer. Experiments were conducted with changes of the ionic strength well below the ones which would lead to osmotic swelling or shrinking, which in turn would change shape, actomyosin cortex, membrane linkage and thus contact mechanics. For example, repulsive electrostatic forces could reduce the total adhesion force with increasing ion concentration. However, under the control of the flatness parameter, it

was assured that none of these shape changes occurred. Furthermore, it is known that the surfaces of developed *D.d.* cells are less negatively charged[180], which can influence the adhesion and migration behaviour of the cells in later developmental stages.

Further studies have shown that negatively charged particles that mimic the surface of the captured bacterium are more efficiently absorbed by *D.d.* than positively charged ones[181]. The three-dimensional structure of SadA, as shown in figure 2.13B, offers a possible explanation for the observed adhesion reduction on a molecular level. The molecular structure shows a bulky, folded extracellular domain containing three epidermal growth factor receptor (EGF) domains. Some of these domains are known to bind divalent ions[182]. Therefore, it could be possible that the increase in ionic strength causes a less adhesive conformational state of SadA. Both potassium and magnesium showed strong reducing properties on the global adhesion parameters and furthermore the pulling length from the step analysis. The step length was strongly influenced by the concentration of added potassium, which may be related to the potassium channels in the cell membrane. Similar relationships in ion dependent adhesion can also be observed with *Chlamydomonas*[183].

The used mM regime of ionic strengths is significantly lower than the realistic case of soil groundwater[184] possibly rendering the observed effects less strong than in nature. However, the regime was intentionally applied in order to exclude osmotic effects, which play a predominant role at higher ionic strengths[126], but can change contact geometry of the cell.

7.2.3 Influence of adhesion proteins, proteins cluster as well as glycocalyx

The adhesome was modified to identify the molecular basis of adhesion. On the one hand SadA was deleted and on the other hand the glycocalyx was degraded. In comparison to the previous subchapter, the manipulation of adhesomes has a stronger influence on adhesion force on the wildtype AX3, whereby the deletion of SadA reduces adhesion much more (factor of 3.6) than the degradation of the glycocalyx (factor of 1.8), as shown in table 7.2. The combination of deletion and degradation decreases the adhesion of the wildtype AX3 the most (factor of 5), indicating posttranslational glycosylation of SadA.

The cell volume is required for the calculation of the flatness. The radius of the cells can be estimated, assuming a spherical shape of a suspended cell. Glycolytic treatment generally reduces the radius slightly. However, the deletion of SadA increases the radius (below the threshold radius for multinucleation, which can be excluded[58]).

For HeLa cells, an adhesion energy per unit area of 0.09 $mN\ m^{-1}$ to 1.5 $mN\ m^{-1}$ could be measured by pipette aspiration[185]. Adhesion energy per unit area has also been calculated for *D.d.* using interference contrast imaging. For the wildtype AX2 a w of 0.22 $mN\ m^{-1}$ has been determined. In addition, talin A (0.06 $mN\ m^{-1}$) and cortexillin null mutants (0.15 $mN\ m^{-1}$) were measured[66]. Since both talin and cortexillin have been shown to be direct binding partners of SadA, the similarity of the values for w of

cells with a deletion of SadA can be explained.

After the critical rupture force is reached, which is described by continuum mechanics, the cell remains partially connected to the substrate at a few points. Finally, these attachment points are released stochastically until the cell is completely detached from the substrate. SadA0 cells have shown the strongest effect in step analysis, suggesting that SadA mediates steps. In addition, the deletion of SadA also increase the adhesion energy per unit area w. However, these two effects have different binding lifetimes of SadA as a consequence, because the steps occur after reaching the critical adhesion force. One possible interpretation would be that nanoscale clusters have a greater dynamic range than individual disperse bonds. Mechanically, the cortical cell organisation and thus the tension could also be influenced. Biochemically, knock-out could also have side effects, which could be alleviated by knock-down in the future. Glycolysis also showed a significant effect in rupture events, especially in the wildtype. This suggests that either SadA is glycosylated or other unknown proteoglycans are involved. Kowal et al.[59] had already proposed other modifications: I) posttranslational phosphorylation of the cytoplasmic domain of SadA, which interacts with cortexilin II) different isoforms at different adhesion states. This could lead to a disturbance with the cluster partners like adhesion protein SibA or Phg1A (relevant in phagocytosis), which could affect the cluster stability.

Based on the slope of the FD curve before the step, one can distinguish between lipid tethers including peripheral proteins or rupture of receptors anchored to the cytoskeleton [186, 187]. In the FD curve, pure membrane tethers can be seen as a force plateau. The plateau forces depend on the bending modulus of the membrane and the tension of the underlying cytoskeleton. If the receptors are coupled to the cytoskeleton, the force increases non-linearly under tension[186]. Since the focus of the present work is on integrin free binding to the surface, no distinction can yet be made between different types of binding events and therefore it will be referred to tether-like steps.

In order to influence the step characteristics, glycolysis is less efficient than deletion of SadA, only the pulling length is influenced. The glycocalyx is the first interface relevant for general adhesion, the changed composition can also induce general effects, as already described for amoeboid cancer cells[188].

The SadA clusters reflected by steps do not react as strongly to changes in bulk surface properties as the maximum adhesion force. This indicates that the SadA bond is based on local interactions such as hydrogen bonds instead of hydrophobic interactions and long-range V.d.W. forces. Assuming that SadA is coupled to the actin cytoskeleton, the cell should be able to adapt or maintain step forces as well as the lifetime of the bonds like integrins.

The FD curve cannot be fully described by the continuum approximation. Rupture events in the FD curve beyond the critical adhesion force, contribute significantly to the integral adhesion energy W_{adh}. Durable molecular contacts lead to discrete steps in the FD curve, which results in de-wetting. Clusters can be responsible for the increased lifetime of these bonds. The involved molecules can be assumed to be parallel bonds, which are kinetically trapped. The rate of bond release increases with the loading rate. Such that cooperative bonds could carry higher loads. Together with a finite range

potential, stochastic bond breakage is possible. In addition, new bonds can be formed which increase the lifetime of the contact.

Therefore, as cells with a deletion of SadA as well as glycocalyx degradation show only minimal adhesion, these two contributions are identified as the main component for substrate adhesion of *D.d.*. Even in the absence of both components, *D.d.* is able to adhere to the surface, indicating the robustness of the organisms adhesive strategies mentioned above, e.g. based on DLVO forces.

7.3 Actin foci dynamics and adhesion cluster mechanics of *D.d.*

In the present work, AFM-based step spectroscopy was used to analyse adhesion spot mechanics of *D.d.* in conjunction with the usage of advanced optics to assess actin foci dynamics. For both approaches, the setup relied on a selection of cells lacking key actin binding proteins. Furthermore LimE probes were characterized as well as different axenic backgrounds. Finally, the relevance of actin foci for clathrin dynamics was investigated.

7.3.1 Differences of the wildtypes AX2, AX3 and DH1

Regarding the axenic laboratory strains and actin LimE probes, within this work three different axenic wildtype backgrounds were used as controls: AX2, AX3 and DH1. They all originally delineate from the isolated parental strain NC4[19] and were identified over the last century upon minimal, bacteria-free medium optimization in different labs[20, 110]. As Bloomfield et al.[18] pointed out, these differences between strains relate to several gene deletions and can be the basis for further phenotypical selection, for example DH1 being an uracil auxotroph mutant of AX3[23]. No strong variability between the different wildtype strains could be observed with respect to the step spectroscopy, e.g. the number of steps (5-8), the step force (110 to 128 pN) and step length (0.55 to 0.76 μm) for these wildtypes, besides the total lift-off distance. The pulling length being significantly reduced to 12.7 μm for AX3 as compared to AX2 (19.1 μm) and DH1 (17.6 μm), which is a collective readout capturing the rupture of all adhesion contacts. These could be related to the increased relative contact, probably indicating increased non-specific adhesive bonds based on the interaction surface, e.g. due to van der Waals forces.

In addition, the adhesion properties were investigated using AFM-based SCFS. This method is particularly suitable for the analysis of single cells, as vertical forces can be both applied and detected in a large working range. The resulting force-distance curves contain characteristic parameters such as the maximum adhesion force F_{max}, as well as the adhesion work W_{adh}.

As a further mean to compare axenic strains, the adhesion properties were determined via the contact area from RICM in relation to the projected bright field area. Here, AX3 cells show an increased ratio compared to the other wildtype cells. Furthermore, the

actin foci readout was similar for all WTs and labels even though sampling rates slightly varied between AX3, AX2 and DH1.

The global parameters F_{max} and W_{adh} showed no WT strain sensitivity. However RICM shows that AX3 possess a high contact area ($\approx 80\%$). In the case of AX2 and DH1 only 50% of their projected BF area is actually contact area. Therefore, only AX3 show some degree of divergence from the other WTs, with less actin foci accompanying more contact area and a reduced total lift-off (pulling length) distance. Such a discrepancy between axenic strains has been described previously[43] and might be linked to the shortened, however still functional, TalA protein found in AX3 as compared to AX2[121], however, this behaviour could not be observed for DH1, which is a direct AX3-derivative cell line. Furthermore, having more actin foci was shown previously to correlate with lower migratory speed for *D.d.* AX2[5]. The reduced contact area, which was observed for AX2 could be a trade off between having more specific adhesion via SadA linked actin foci or less unspecific adhesion over a bigger contact area. The specified adhesion hampering migration of AX2.

7.3.2 Actin foci visualized via TIRFM with LimE

To visualise actin foci with TIRFM, the actin binding protein LimE as well as the shorter LimEΔcoil were used, which additionally linked to fluorophores like GFP or mRFPmars. Small but significant differences in number and lifetime of actin foci were found, but not in the temporal pattern of the signal as quantified by t_{before}/t_{after}. Regarding the usage of labels, a reduction in the lifetime of LimE-mRFPmars over LimE-GFP to LimEΔcoil-mRFPmars was found, which might be directly hinting at reduced diffusion rates expectable upon size variation of these labels[92, 99, 103]. Therefore the desired amount of observable foci might be relevant for the choice of label, especially when the truncated LimEΔcoil also shows lower unspecific cytoplasmic background fluorescence[106] albeit more blinking. This is consistent with a previous study focused on various actin labels and their different dynamical aspects in *D.d.* cells[95] necessitating parallel usage of different labels.

In addition, actin foci were examined optically using TIRFM: therefore, a tracking software has been developed to compare the properties of actin foci with the results of force spectroscopy. This has been validated using manual foci tracking and was assessed cumulatively using KDE plots.

The number of appearing foci per minute ranges from 15.5-17.0 min^{-1}. The mean lifetime of a focus is 10.3 s, with the exception of DH1. When determining the cell contour, it was observed that the wildtypes show significant differences in size, which influences the density of the foci, but not the distance from individual foci to their nearest neighbours, which is almost constant at 0.5 μm. With the difference in size of the cells, it can be assumed that the distance of the foci from the centre of mass might be also influenced. Therefore this distance was assessed and normalised to a reference radius at the cell contour to compare the position of the foci in the cell. R_{max} is this radius, where a higher probability for foci can be observed.

Furthermore, different experimental conditions, like sampling rate and time interval

($\mathcal{S}$, $\mathcal{L}$) were used and tested on AX2 with GFP-labelled LimE, which was primarily used as ABP/label combination for further experiments. The major properties (N_{foci}, l_{norm}, nn) are not influenced by this.

However, experimental uncertainties exist due to varying expression levels for different wildtype/vector combinations and therefore future studies might compare different pairings.

7.3.3 Deletion or inhibition of key actin binding proteins

Beyond wildtype characterisation, key actin binding proteins were inhibited or deleted to investigate their influence on actin foci.

SadA0

As previous studies have shown[41, 121], the adhesive properties decreases when the transmembrane protein SadA is absent compared to the corresponding wildtype AX3. This can be demonstrated with both RICM and AFM-based SCFS, which shows that SadA is relevant for substrate adhesion of *D.d.*. In addition the adhesion parameters were assessed in dependence of speed and contact time. It was observed that the adhesion properties (F_{max}, W_{adh}, N_{Step}, F_{Step}, $l_{pulling}$) of AX3 increase with increasing speed and contact time. The deletion of SadA, however, gives contrary results: In contrast to the WT cells F_{max}, W_{adh} and the number of steps decreases with increasing velocity for the deletion of the protein SadA. Therefore SadA containing wildtype cells behave similar to catch bonds[189] while its deletion leads to slip bond-like properties when modulating pulling rates, when 30 s for cluster formation are allowed. However, more detailed studies on isolated molecules of SadA in regards to their lifetime will be needed.

Surprisingly, AX3 with missing SadA shows twice as much actin foci as the wildtype in TIRFM, but with a slightly shorter lifetime, larger positional shift and higher velocity of the foci. The number of actin foci thus is inversely proportional to the number of steps in the FD curve, as summarized in table 7.3. Similar observations have been already shown in the past with Clc0 cells[190], where the endocytotic apparatus is disturbed. As well as myosinII0 or PTEN0 cells, which triggers all severe disturbances of the actin dynamics and polarisation.

In addition the size of the cells increases by 50%, but not to levels of multinucleated cells[58]. The foci appear more at the periphery compared to the wildtype with small hotspots at R_{max} with a regular distance: Actin foci are very homogeneously distributed over the cell surface.

In the literature on actin foci[5] it was shown that the absence of myosin II increases the number of actin foci and prolongs their lifetime, although actin and myosin II are not co-localised. In contrast, SibA-myoII are co-localised for force transmission especially at the rear of migrating cells, and SadA-myoVII interaction was postulated[58, 84, 159].

ScarA0

Deletion of ScarA showed little change in the adhesion properties in the SCFS analysis, so no analysis of the actin foci of ScarA0 cells was performed. In RICM an increased contact area was measured compared to the wildtype AX2. Possibly a Scar deletion is compensated by WASp[191].

Table 7.3: Influence of key actin binding protein deletion on cell-substrate adhesion of *D.d.* - Step analysis of FD curves from inhibited/deleted key actin binding proteins and the corresponding axenic background. Wildtype (AX3, AX2, DH1) parameters are comparable. SadA0, CK666 and TalA0 affect the steps strongly in amount (N_{Step}), the step force (F_{Step} in pN) and the pulling length (l_{Pulling} in μm). The step length (l_{Step} in μm) increases with the deletion of TalA and TalB. Furthermore the general parameter maximal adhesion force (F_{max} in nN) and -work (W_{adh} in fJ) are shown, both show similarities with F_{Step}. For comparison the relative contact area is shown. ‡ already published in [150]. Furthermore the number of actin foci (N_{Foci} in $1/s$) and the half lifetime (lt_{50} in s) from TIRFM are shown.

	AX3	SadA0	**AX2**	ScarA0	CK666	TalA0	ForA0	**DH1**	TalB0
N_{Step}	7	2^{***}	8	6^{NS}	2.5^{***}	2^{***}	6^{NS}	5	5^{NS}
F_{Step}	128	88^{***}	124	109^{***}	85^{***}	84^{***}	110^{***}	113	101^{***}
l_{Step}	0.61	0.95^{NS}	0.55	0.54^{NS}	0.41^{***}	0.93^{***}	0.65^{NS}	0.76	1.18^{***}
l_{Pulling}	12.7	2.6^{***}	19.1	13.6^{**}	4.0^{***}	2.5^{***}	13.8^{**}	17.6	18^{NS}
F_{max}	5.9	1.4^{***}	5.5	5.2^{NS}	3.8^{***}	$2.0^{***‡}$	3.1^{***}	5.3	3.7^{***}
W_{adh}	9.4	0.5^{***}	10.9	9.0^{*}	3.0^{***}	1.7^{***}	6.6^{***}	8.9	7.5^{*}
$\frac{RICM}{BF}$	0.81	0.4^{***}	0.56	0.68^{**}	0.61^{NS}	$0.22^{***‡}$	0.71^{***}	0.48	0.49^{NS}
N_{Foci}	17	33.5^{***}	16.7		8.7^{**}	16.2^{NS}	15^{NS}	15.5	0
lt_{50}	10.2	9.6^{**}	10.4		13.1^{***}	12.2^{***}	10.4^{NS}	8.0	16.2

CK666

The branching of actin fibres by Arp2/3 complex was inhibited by CK666, as deletion of the Arp2/3 would have been lethal[124]. The inhibition showed a significant reduction of the adhesion properties (F_{max}, W_{adh}, N_{Step}, F_{Step}, l_{Step}, $l_{pulling}$) measured by AFM-based SCFS. In contrast to SadA0 the step length decreases. Regardless of the inhibition, we still found actin foci, but only 50% of the wildtype amount and with a significantly increased lifetime ($\approx 30\%$). Therefore, we assume here an increase in the growth of the SadA cluster, but not in its stability, as it cannot resist any major force. The inhibition of the branching reduces the amount of foci hotspots in the KDE plots. This is the only manipulation of key actin binding proteins where both the number of actin foci and the number of steps in the FD curve are reduced.

CK666 inhibits gel-like actin- a central contribution to the actomyosin cortex- and thus planar protrusion, like lamellipodia or pseudopodia. There seems to be a connection between structural integrity of adhesion cluster and Arp2/3. Accordingly, the Arp2/3 complex is also relevant for curvotaxis[192].

TalA0

Deletion of the actin anchoring protein TalA shows similar changes in adhesion properties as inhibition of CK666. However, the step length is significantly increased. The number of actin foci did not change significantly, but the lifetime is significantly increased.

Hotspots of actin foci can be still detected in the KDE plots. It is very likely that TalA is relevant for the equilibrium of SadA cluster and Arp2/3-depended actin structures. As mentioned before talin A is crucial for weak adhesion to passivated surfaces and highly polymorphic in different axenic strains. In all likelihood, force transmission between the SadA cluster and the Arp2/3-dependent actin structures is mediated by TalA, which makes compensatory effects likely.

ForA0

Only minor changes in adhesion properties were observed when deleting ForA. The contact area of RICM for ForA0 was also increased. The analysis showed that the deletion of ForA has no influence on the number and lifetime of the actin foci. However, the positional shift and velocity increased significantly. The foci are slightly more present in the periphery. In addition, the cells are smaller compared to the wildtype AX2 cells and the distance between the foci is smaller, too. Especially noticeable is the distribution of the foci in the cell. Regarding KDE plots, hardly any foci can be observed near the centre of mass. In addition, at R_{max} there are more local hotspots of actin foci. One explanation for this result is that a compensation by other formin proteins could occur, as molecular redundancy studies of Litschko et al.[193] showed: Formin-null single and double mutants (ForA0 or ForE0 or ForH0) showed only moderate changes in the cortical fluidity, while simultaneous deletion of ForA, ForE and ForH resulted in massive changes in cortical actin flow and architecture. Recently, formin was shown to be relevant for a minority of cortical actin, but especially for longer actin fibres determining elasticity and thus cortical tension[194] - in higher eukaryotes even for stress fibres, which *D.d.* does not possess. More recently Schroeder has shown that the Arp2/3 complex plays a major role for adhesion in complex environments and contact guidance[192].

TalB0

The deletion of the actin anchor protein TalB shows a slight reduction of W_{adh} and no changes in the amount of steps per FD curve compared to the wildtype DH1, but surprisingly hardly any actin foci could be detected. Usually a compensation by the other talin protein could occur[69].

More recently it was shown that talin A binds actin filaments pre-stretched by myosin II especially at the uropod of developed cells, while talin B is enriched at the anterior cell pole excluded from those regions[195].

In summary, it was shown that wildtype, inhibition of the Arp2/3 complex or deletion of ForA show a proportional dependency between the number of steps in the FD curve and the number of actin foci on the ventral side of the cell, as shown in Figure 7.4.

It is assumed that the deletion of TalA or SadA influences the stability of the adhesome and therefore steps can no longer be identified in the FD curve. To confirm this observation, further experiments with the inhibitor CK666 should be conducted in a concentration dependent manner as already shown in first experiments by Schröder[192].

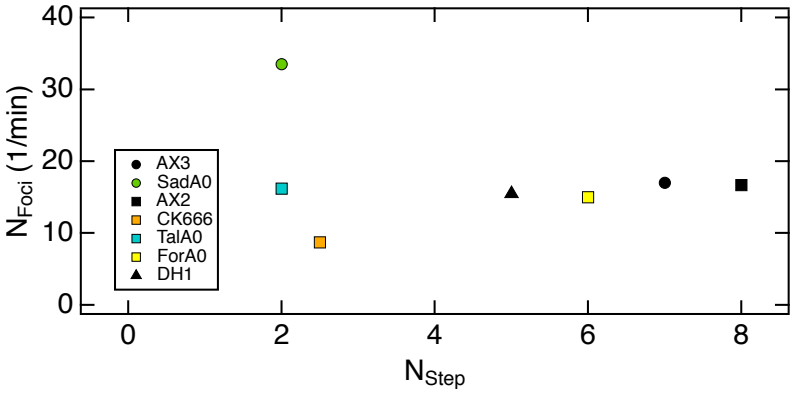

Figure 7.4: Relationship between the number of actin foci and the number of steps - For this purpose, the data from the TIRFM measurement were combined with those from the SCFS measurement and the medians of related categories were plotted against each other.

For eukaryotic cells with integrins, step-slope cut-offs could be defined, which allow differentiation of processes associated with cytoskeletal attachment or unspecific lipid cylinder formation events[196, 197], thus the distinction of jumps from tethers. This could be of central importance for future step spectroscopy of *D.d.*. However, an appropriate threshold definition based on further experiments with antibodies against adhesion proteins like SadA will be necessary. In addition, key actin protein deletion could be combined with model substrates to quantify non-specific forces.

Note that for different vectors encoding various fluorescence tags expression levels can vary, which should be quantified in future. In addition to sequential scanning and filter usage, the overlap of emission and excitation of fluorophore spectra in dual labelled cells should be kept in mind when selecting fluorophores for double labelling.

7.3.4 Relationship between clathrin-mediated endocytosis (CME) and actin foci

Finally, in the present work, the relationship between clathrin-mediated endocytosis (CME) and actin foci was analysed. 80% of the observed actin foci co-localise with clathrin. Similar results have been described by Heinrich et al.[159]. Surprisingly, it was observed that 20% of the clathrin structures appear after an actin focus: this might hint at a clathrin plaque where clathrin stabilizes actin based adhesion points[116]. Independent of the sequence of appearance, as long as clathrin is co-localised with actin, the actin foci lifetime is increased, while clathrin lifetime is unaffected. This suggests that the clathrin-actin interplay is highly versatile.

In addition, with the combination of TIRFM and RICM, the movement of the membrane at the position of actin focus could be observed. It was noticed, that the membrane moves to the substrate well before the appearance of a clathrin signal and only after actin has vanished the membrane lifts again.

Some recent studies have shown a discrepancy between marcopinocytic dynamics of axenic strains compared to wildtype NC4, which feeds on bacteria. It has been shown that Ras- and actin activity is increased in axenic strains and pseudopod dynamics are shifted to high Ras activity, also due to elevated macropinocytosis. It can be excluded that the actin foci observed here are the result of a developing macropinocytotic incision, but are rather involved in CME[198]. No micropinosomes are observable in the actin signal. Furthermore, it has recently been shown that CME-associated actin foci can also take part at Scar-mediated dynamics and cell polarisation via rho-GTPases by WASp[7] in a feedback loop thus linking CME to both adhesion and migration. The foci described here can be assumed to take over several actin functions and thereby highlight a functional flexibility and reorganisation of actin.

Several recent studies on eukaryotes with integrins such as Amato et al.[7] have studied clathrin plaques in more detail. Clathrin pits, which are involved in CME and clathrin patches involved in adhesion could explain the sequence of appearance of two groups as described above. They have been found, for example, in adhesion sites upon mitosis near the nucleus and as structures of frustrated endocytosis, which are relevant for durotaxis and thus for mechanosensoring[50]. Clathrin patches normally show a longer lifetime. A method to detect these lifetimes could be time-resolved metal-induced energy transfer (MIET): the advantage of this method is the nanometer resolution optics in the axial range[199, Chapter 8]. In first stationary dual colour experiments the deletion of Clc could be linked to actin height changes[190].

The whole chapter can be summarized as follows: the most important finding is that the number of actin foci decreased in line with number of steps decreasing when the Arp2/3-complex is inhibited. In contrast, SadA deletion increases the number of actin foci with decreasing step number. Moreover, formins are not reflected in step or foci dynamics and TalA are more relevant for adhesion points then TalB. Regarding Clc co-localisation, two different subgroups could be identified, each with increased actin lifetimes: clathrin appearing before actin as expectable for canonical CME as well as actin appearing before clathrin possibly related to clathrin plaque formation.

8 Conclusion

Based on the hypothesis formulated in the introduction, the following conclusion on the adhesion behaviour of amoeba *D.d.* is drawn:

Is there an efficient protocol to prevent the adhesion of *D.d.*?

30% PEG gels with a 1 μm layer thickness inhibit the adhesion of *D.d.*. However, it was discovered that some wildtype strains do not have this effect and that the developmental state and fluorescence-tagged cytoskeleton proteins reduce or eliminate this effect. Using SCFS, a significant reduction in adhesion force could always be detected between glass and PEG substrates, regardless of the conditions mentioned above.

Can we identify and quantify forces involved in *D.d.* adhesion by intelligent substrate design?

Using multilayer model substrates, Van der Waals forces could be identified as one driving force category. By silanating the substrates, additional hydrophobic forces were observed. The change in the ionic strength of the medium also revealed that electrostatic forces are involved in *D.d.* adhesion. However, the strongest adhesion forces are provided by the glycocalyx and the transmembrane protein SadA or their combination, as summarized in figure 8.1.

Actin foci represent signalling hubs relevant in the adhesion of *D.d.*

Clear differences could be made between the formin contribution, which create long actin fibres more relevant to cortical tension than adhesion and the gel-like actin network induced by Arp2/3 complex. Its inhibition reduces both step and spot density. The connection of the network to the substrate also plays a decisive role: the deletion of SadA and TalA also reduces the adhesion force, as forces probably cannot be transferred to the substrate. However, it can also be observed that the number of actin foci increases significantly, thus influencing the stability of actin foci.

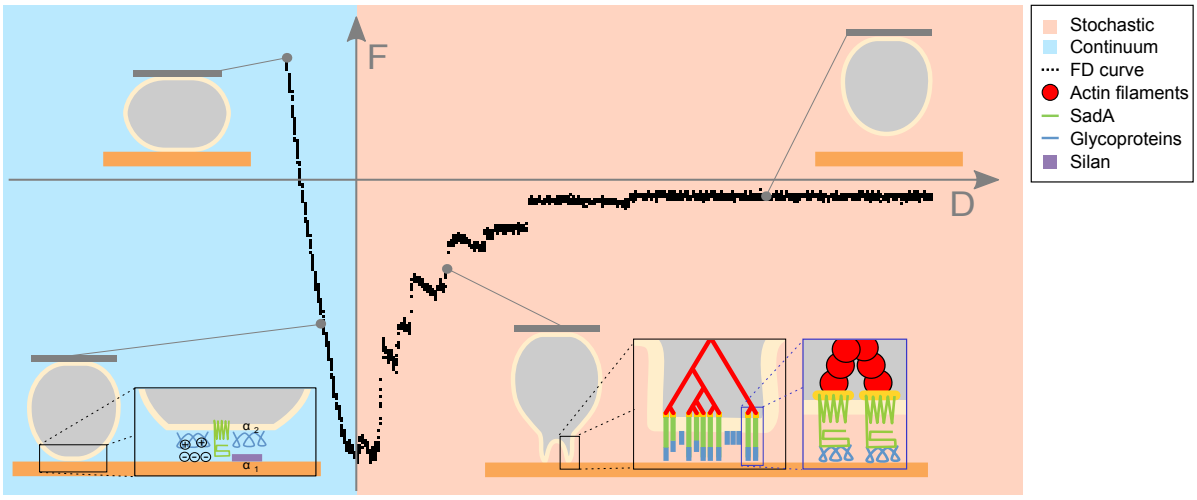

Figure 8.1: Phases of cell substrate adhesion - A FD curve from an AFM-based SCFS experiment (black). At the minimum of the FD curve the plot is divided into two parts: continuum (light blue) and a stochastic (light orange) part. In addition cartoons show the interaction of the cell to the underlying substrate during de-attachment. The continuum part is mainly influenced by the underlying substrate. In comparison, the stochastic part is mainly influenced by the adhesion proteins of the cell. Printed with the permission of the publisher [41].

Are actin foci both involved in adhesion and endocytosis?

Besides actin foci that occur without CME, Clc clusters probably occur mainly together with actin foci, which could represent both pits and adhesion plaques. The latter probably contribute to the adhesion of actin foci. Furthermore, it could also be shown that clathrin plaques attach to actin structures. It is also assumed that this stabilises adherent structures.

List of Figures

List of Tables

Bibliography

[1] Gilles R Dagenais, Darryl P Leong, Sumathy Rangarajan, Fernando Lanas, Patricio Lopez-Jaramillo, Rajeev Gupta, Rafael Diaz, Alvaro Avezum, Gustavo BF Oliveira, Andreas Wielgosz, et al. Variations in common diseases, hospital admissions, and deaths in middle-aged adults in 21 countries from five continents (pure): a prospective cohort study. *The Lancet*, 395(10226):785–794, 2020.

[2] Lauren S Havel, Erik R Kline, Alessandra M Salgueiro, and Adam I Marcus. Vimentin regulates lung cancer cell adhesion through a vav2–rac1 pathway to control focal adhesion kinase activity. *Oncogene*, 34(15):1979–1990, 2015.

[3] E. K. Paluch, I. M. Aspalter, and M. Sixt. Focal adhesion-independent cell migration. *Annual Review of Cell and Developmental Biology, Vol 32*, 32:469–490, 2016.

[4] Kevin L. Prime and George M. Whitesides. Self-assembled organic monolayers: model systems for studying adsorption of proteins at surfaces. *Science*, pages 1164–1167, 1991.

[5] K. S. Uchida and S. Yumura. Dynamics of novel feet of dictyostelium cells during migration. *J Cell Sci*, 117(Pt 8):1443–55, 2004.

[6] Masahito Tanaka, Koushiro Fujimoto, and Shigehiko Yumura. Regulation of the total cell surface area in dividing dictyostelium cells. *Frontiers in Cell and Developmental Biology*, 8, 2020.

[7] Clelia Amato, Peter A. Thomason, Andrew J. Davidson, Karthic Swaminathan, Shehab Ismail, Laura M. Machesky, and Robert H. Insall. Wasp restricts active rac to maintain cells' front-rear polarization. *Current Biology*, 29(24):4169 – 4182.e4, 2019.

[8] James H Vines and Jason S King. The endocytic pathways of dictyostelium discoideum. *International Journal of Developmental Biology*, 63(8-9-10):461–471, 2019.

[9] Danton H O'Day and Alex Keszei. Signalling and sex in the social amoebozoans. *Biological Reviews*, 87(2):313–329, 2012.

[10] Juliet C. Coates and Adrian J. Harwood. Cell-cell adhesion and signal transduction during dictyostelium development. *Journal of Cell Science*, 114(24):4349–4358, 2001.

[11] Miho Iijima, Yi Elaine Huang, and Peter Devreotes. Temporal and spatial regulation of chemotaxis. *Developmental cell*, 3(4):469–478, 2002.

[12] Carole A Parent and Peter N Devreotes. Molecular genetics of signal transduction in dictyostelium. *Annual review of biochemistry*, 65(1):411–440, 1996.

[13] Joan E Strassmann, Yong Zhu, and David C Queller. Altruism and social cheating in the social amoeba dictyostelium discoideum. *Nature*, 408(6815):965–967, 2000.

[14] Rex L Chisholm and Richard A Firtel. Insights into morphogenesis from a simple developmental system. *Nature reviews Molecular cell biology*, 5(7):531–541, 2004.

[15] P. N. Devreotes, S. Bhattacharya, M. Edwards, P. A. Iglesias, T. Lampert, and Y. C. Miao. Excitable signal transduction networks in directed cell migration. *Annual Review of Cell and Developmental Biology, Vol 33*, 33:103–125, 2017.

[16] L Eichinger, JA Pachebat, G Glöckner, M-A Rajandream, R Sucgang, M Berriman, J Song, R Olsen, Ku Szafranski, Q Xu, et al. The genome of the social amoeba dictyostelium discoideum. *Nature*, 435(7038):43–57, 2005.

[17] Jeroen Roelofs and Peter JM Van Haastert. Genes lost during evolution. *Nature*, 411(6841):1013–1014, 2001.

[18] Gareth Bloomfield, Yoshimasa Tanaka, Jason Skelton, Alasdair Ivens, and Robert R Kay. Widespread duplications in the genomes of laboratory stocks of dictyostelium discoideum. *Genome biology*, 9(4):R75, 2008.

[19] R. Sussman and M. Sussman. Cultivation of dictyostelium discoideum in axenic medium. *Biochemical and Biophysical Research Communications*, 29(1):53 – 55, 1967.

[20] D. J. Watts and J. M. Ashworth. Growth of myxamoebae of the cellular slime mould Dictyostelium discoideum in axenic culture. *Biochemical Journal*, 119(2):171–174, 09 1970.

[21] Jakob Franke and Richard Kessin. A defined minimal medium for axenic strains of dictyostelium discoideum. *Proceedings of the National Academy of Sciences of the United States of America*, 74(5):2157, 1977.

[22] Gareth Bloomfield, David Traynor, Sophia P Sander, Douwe M Veltman, Justin A Pachebat, and Robert R Kay. Neurofibromin controls macropinocytosis and phagocytosis in dictyostelium. *Elife*, 4:e04940, 2015.

[23] Michael J Caterina, JL Milne, and Peter N Devreotes. Mutation of the third intracellular loop of the camp receptor, car1, of dictyostelium yields mutants impaired in multiple signaling pathways. *Journal of Biological Chemistry*, 269(2):1523–1532, 1994.

[24] Jeffrey A Hadwiger and Richard A Firtel. Analysis of g alpha 4, a g-protein subunit required for multicellular development in dictyostelium. *Genes & Development*, 6(1):38–49, 1992.

[25] M Schwalb and R Roth. Axenic growth and development of the cellular slime mould, dictyostelium discoideum. *Microbiology*, 60(2):283–286, 1970.

[26] Miguel Vicente-Manzanares, Xuefei Ma, Robert S Adelstein, and Alan Rick Horwitz. Non-muscle myosin ii takes centre stage in cell adhesion and migration. *Nature reviews Molecular cell biology*, 10(11):778–790, 2009.

[27] Elisabeth G Rens and Roeland MH Merks. Cell shape and durotaxis explained from cell-extracellular matrix forces and focal adhesion dynamics. *Iscience*, 23(9):101488, 2020.

[28] Anton Bukatin, Igor Kukhtevich, Norbert Stoop, Jörn Dunkel, and Vasily Kantsler. Bimodal rheotactic behavior reflects flagellar beat asymmetry in human sperm cells. *Proceedings of the National Academy of Sciences*, 112(52):15904–15909, 2015.

[29] Sébastien G Ricoult, Timothy E Kennedy, and David Juncker. Substrate-bound protein gradients to study haptotaxis. *Frontiers in bioengineering and biotechnology*, 3:40, 2015.

[30] Anne J Ridley and Alan Hall. The small gtp-binding protein rho regulates the assembly of focal adhesions and actin stress fibers in response to growth factors. *Cell*, 70(3):389–399, 1992.

[31] Sandrine Etienne-Manneville and Alan Hall. Rho gtpases in cell biology. *Nature*, 420(6916):629–635, 2002.

[32] Cameron Tropea and Alexander L Yarin. *Springer handbook of experimental fluid mechanics*. Springer Science & Business Media, 2007.

[33] Gregor Trefalt and Michal Borkovec. Overview of dlvo theory. *Laboratory of Colloid and Surface Chemistry, University of Geneva, Switzerland*, pages 1–10, 2014.

[34] J.N. Israelachvili. Intermolecular and surface forces. *Academic Press*, 1992.

[35] Peter R Bergethon and Elizabeth R Simons. *Biophysical chemistry: molecules to membranes*. Springer Science & Business Media, 2012.

[36] Melissa A Brown, Charles S Wallace, Charles C Anamelechi, Edward Clermont, William M Reichert, and George A Truskey. The use of mild trypsinization conditions in the detachment of endothelial cells to promote subsequent endothelialization on synthetic surfaces. *Biomaterials*, 28(27):3928–3935, 2007.

[37] Nagendran Ramalingam, Christof Franke, Evelin Jaschinski, Moritz Winterhoff, Yao Lu, Stefan Brühmann, Alexander Junemann, Helena Meier, Angelika A Noegel, Igor Weber, et al. A resilient formin-derived cortical actin meshwork in the rear drives actomyosin-based motility in 2d confinement. *Nature communications*, 6(1):1–15, 2015.

[38] Claudia Arbore, Laura Perego, Marios Sergides, and Marco Capitanio. Probing force in living cells with optical tweezers: from single-molecule mechanics to cell mechanotransduction. *Biophysical reviews*, pages 1–18, 2019.

[39] Amelia Ahmad Khalili and Mohd Ridzuan Ahmad. A review of cell adhesion studies for biomedical and biological applications. *International journal of molecular sciences*, 16(8):18149–18184, 2015.

[40] Ulrich S. Schwarz and Jérôme R.D. Soiné. Traction force microscopy on soft elastic substrates: A guide to recent computational advances. *Biochimica et Biophysica Acta (BBA)-Molecular Cell Research*, 1853(11):3095–3104, 2015.

[41] Nadine Kamprad, Hannes Witt, Marcel Schröder, Christian Titus Kreis, Oliver Bäumchen, Andreas Janshoff, and Marco Tarantola. Adhesion strategies of dictyostelium discoideum - a force spectroscopy study. *Nanoscale*, 10:22504–22519, 2018.

[42] Françoise Brochard-Wyart and Pierre-Gilles de Gennes. Unbinding of adhesive vesicles. *Comptes Rendus Physique*, 4(2):281 – 287, 2003.

[43] Richa Karmakar, Christoph Schich, Nadine Kamprad, Vanessa Scheller, Edgar Gutierrez, Alex Groisman, Wouter-Jan Rappel, and Marco Tarantola. Novel micropatterning technique reveals dependence of cell-substrate adhesion and migration of social amoebas on parental strain, development, and fluorescent markers. *PloS one*, 15(7):e0236171, 2020.

[44] S.I. Jeon, J.H. Lee, J.D. Andrade, and Pr.G. De Gennes. Protein-surface interactions in the presence of polyethylene oxide: I. simplified theory. *Journal of colloid and interface science*, 142(1):149–158, 1991.

[45] G.A. Dunn and J.P. Heath. A new hypothesis of contact guidance in tissue cells. *Experimental cell research*, 101(1):1–14, 1976.

[46] M. K. Driscoll, X. Y. Sun, C. Guven, J. T. Fourkas, and W. Losert. Cellular contact guidance through dynamic sensing of nanotopography. *Acs Nano*, 8(4):3546–3555, 2014.

[47] Anne Reversat, Florian Gaertner, Jack Merrin, Julian Stopp, Saren Tasciyan, Juan Aguilera, Ingrid de Vries, Robert Hauschild, Miroslav Hons, Matthieu Piel, et al. Cellular locomotion using environmental topography. *Nature*, pages 1–4, 2020.

[48] Christoph Blum. *Curvotaxis and Pattern Formation in the Actin Cortex of Motile Cells*. Phd thesis, Universität Göttingen, 2015.

[49] Bryant L Doss, Meng Pan, Mukund Gupta, Gianluca Grenci, René-Marc Mège, Chwee Teck Lim, Michael P Sheetz, Raphaël Voituriez, and Benoît Ladoux. Cell response to substrate rigidity is regulated by active and passive cytoskeletal stress. *Proceedings of the National Academy of Sciences*, 117(23):12817–12825, 2020.

[50] Chika Okimura, Yuichi Sakumura, Katsuya Shimabukuro, and Yoshiaki Iwadate. Sensing of substratum rigidity and directional migration by fast-crawling cells. *Physical Review E*, 97(5):052401, 2018.

[51] Peter Loskill, Hendrik Hähl, Thomas Faidt, Samuel Grandthyll, Frank Müller, and Karin Jacobs. Is adhesion superficial? silicon wafers as a model system to study van der waals interactions. *Advances in colloid and interface science*, 179:107–113, 2012.

[52] A. Sebe-Pedros, A. J. Roger, F. B. Lang, N. King, and I. Ruiz-Trillo. Ancient origin of the integrin-mediated adhesion and signaling machinery. *Proceedings of the National Academy of Sciences of the United States of America*, 107(22):10142–10147, 2010.

[53] Evelyne Bergeret, Jackie Perrin, Michael Williams, Didier Grunwald, Elodie Engel, Dominique Thevenon, Emmanuel Taillebourg, Franz Bruckert, Pierre Cosson, and Marie-Odile Fauvarque. Tm9sf4 is required for drosophila cellular immunity via cell adhesion and phagocytosis. *Journal of cell science*, 121(20):3325–3334, 2008.

[54] Romain Froquet, Nathalie Cherix, Raphael Birke, Mohammed Benghezal, Elisabetta Cameroni, François Letourneur, Hans-Ulrich Mösch, Claudio De Virgilio, and Pierre Cosson. Control of cellular physiology by tm9 proteins in yeast and dictyostelium. *Journal of Biological Chemistry*, 283(11):6764–6772, 2008.

[55] S. Cornillon, E. Pech, M. Benghezal, K. Ravanel, E. Gaynor, F. Letourneur, F. Bruckert, and P. Cosson. Phg1p is a nine-transmembrane protein superfamily member involved in dictyostelium adhesion and phagocytosis. *Journal of Biological Chemistry*, 275(44):34287–34292, 2000.

[56] S. Cornillon, L. Gebbie, M. Benghezal, P. Nair, S. Keller, B. Wehrle-Haller, S. J. Charette, F. Bruckert, F. Letourneur, and P. Cosson. An adhesion molecule in free-living dictyostelium amoebae with integrin beta features. *Embo Reports*, 7(6):617–621, 2006.

[57] S. Cornillon, R. Froquet, and P. Cosson. Involvement of sib proteins in the regulation of cellular adhesion in dictyostelium discoideum. *Eukaryotic Cell*, 7(9):1600–1605, 2008.

[58] P. Fey, S. Stephens, M. A. Titus, and R. L. Chisholm. Sada, a novel adhesion receptor in dictyostelium. *Journal of Cell Biology*, 159(6):1109–1119, 2002.

[59] A. S. Kowal and R. L. Chisholm. Uncovering a role for the tail of the dictyostelium discoideum sada protein in cell-substrate adhesion. *Eukaryotic Cell*, 10(5):662–671, 2011.

[60] S Nir and M Andersen. Van der waals interactions between cell surfaces. *The Journal of membrane biology*, 31(1):1–18, 1977.

[61] Kellar Autumn, Metin Sitti, Yiching A Liang, Anne M Peattie, Wendy R Hansen, Simon Sponberg, Thomas W Kenny, Ronald Fearing, Jacob N Israelachvili, and Robert J Full. Evidence for van der waals adhesion in gecko setae. *Proceedings of the National Academy of Sciences*, 99(19):12252–12256, 2002.

[62] W. F. Loomis, D. Fuller, E. Gutierrez, A. Groisman, and W. J. Rappel. Innate non-specific cell substratum adhesion. *Plos One*, 7(8), 2012.

[63] Anna Bagorda and Carole A Parent. Eukaryotic chemotaxis at a glance. *Journal of cell science*, 121(16):2621–2624, 2008.

[64] DJG Rees, Sarah E Ades, SJ Singer, and Richard O Hynes. Sequence and domain structure of talin. *Nature*, 347(6294):685–689, 1990.

[65] J. Niewohner, I. Weber, M. Maniak, A. Müller-Taubenberger, and G. Gerisch. Talin-null cells of dictyostelium are strongly defective in adhesion to particle and substrate surfaces and slightly impaired in cytokinesis. *Journal of Cell Biology*, 138(2):349–361, 1997.

[66] Rudolf Simson, Eva Wallraff, Jan Faix, Jens Niewöhner, Günther Gerisch, and Erich Sackmann. Membrane bending modulus and adhesion energy of wild-type and mutant cells of dictyostelium lacking talin or cortexillins. *Biophysical journal*, 74(1):514–522, 1998.

[67] M Tsujioka, LM Machesky, SL Cole, K Yahata, and K Inouye. A unique talin homologue with a villin headpiece-like domain is required for multicellular morphogenesis in dictyostelium. *Current Biology*, 9(7):389–394, 1999.

[68] Ines Carrin, Irene Murgia, Andrew McLachlan, and Robert R Kay. A mutational analysis of dictyostelium discoideum multicellular development. *Microbiology*, 142(4):993–1003, 1996.

[69] Masatsune Tsujioka, Kunito Yoshida, Akira Nagasaki, Shigenobu Yonemura, Annette Müller-Taubenberger, and Taro Q. P. Uyeda. Overlapping functions of the two talin homologues in dictyostelium. *Eukaryotic Cell*, 7(5):906–916, 2008.

[70] Susan Nicholson-Dykstra, Henry N Higgs, and Elizabeth S Harris. Actin dynamics: growth from dendritic branches. *Current Biology*, 15(9):R346–R357, 2005.

[71] Pierre Dustin. Microtubule poisons. In *Microtubules*, pages 171–233. Springer, 1984.

[72] Elaine Fuchs and Klaus Weber. Intermediate filaments: structure, dynamics, function and disease. *Annual review of biochemistry*, 63(1):345–382, 1994.

[73] Elaine Fuchs and Don W Cleveland. A structural scaffolding of intermediate filaments in health and disease. *Science*, 279(5350):514–519, 1998.

[74] Thomas D Pollard, William C Earnshaw, and Lippincott-Schwartz. *Cell biology*. Elsevier Health Sciences, 2007.

[75] Till Bretschneider, Hans G Othmer, and Cornelis J Weijer. Progress and perspectives in signal transduction, actin dynamics, and movement at the cell and tissue level: lessons from dictyostelium. *Interface Focus*, 6(5):20160047, 2016.

[76] Clement PM Scipion, Umesh Ghoshdastider, Fernando J Ferrer, Tsz-Ying Yuen, Jantana Wongsantichon, and Robert C Robinson. Structural evidence for the roles of divalent cations in actin polymerization and activation of atp hydrolysis. *Proceedings of the National Academy of Sciences*, 115(41):10345–10350, 2018.

[77] Byron Hetrick, Min Suk Han, Luke A Helgeson, and Brad J Nolen. Small molecules ck-666 and ck-869 inhibit actin-related protein 2/3 complex by blocking an activating conformational change. *Chemistry & biology*, 20(5):701–712, 2013.

[78] Thomas D. Pollard and John A. Cooper. Actin, a central player in cell shape and movement. *Science*, 326(5957):1208–1212, 2009.

[79] Thomas D Pollard. Regulation of actin filament assembly by arp2/3 complex and formins. *Annu. Rev. Biophys. Biomol. Struct.*, 36:451–477, 2007.

[80] R Dyche Mullins, John A Heuser, and Thomas D Pollard. The interaction of arp2/3 complex with actin: nucleation, high affinity pointed end capping, and formation of branching networks of filaments. *Proceedings of the National Academy of Sciences*, 95(11):6181–6186, 1998.

[81] Brad J Nolen and Thomas D Pollard. Insights into the influence of nucleotides on actin family proteins from seven structures of arp2/3 complex. *Molecular cell*, 26(3):449–457, 2007.

[82] N. Ibarra, A. Pollitt, and R.H. Insall. Regulation of actin assembly by SCAR/WAVE proteins. *Biochemical Society Transactions*, 33(6):1243–1246, 10 2005.

[83] Gary Laevsky and David A Knecht. Cross-linking of actin filaments by myosin ii is a major contributor to cortical integrity and cell motility in restrictive environments. *Journal of Cell Science*, 116(18):3761–3770, 2003.

[84] M. Tsujioka, S. Yumura, K. Inouye, H. Patel, M. Ueda, and S. Yonemura. Talin couples the actomyosin cortex to the plasma membrane during rear retraction and cytokinesis. *Proceedings of the National Academy of Sciences of the United States of America*, 109(32):12992–12997, 2012.

[85] Raymond W Washington and David A Knecht. Actin binding domains direct actin-binding proteins to different cytoskeletal locations. *BMC Cell Biology*, 9(1):1–16, 2008.

[86] Yoshio Fukui and Shinya Inoué. Amoeboid movement anchored by eupodia, new actin-rich knobby feet in dictyostelium. In *Collected Works Of Shinya InouÉ: Microscopes, Living Cells, and Dynamic Molecules (With DVD-ROM)*, pages 787–802. World Scientific, 2008.

[87] Shigehiko Yumura and Toshiko Kitanishi-Yumura. Fluorescence-mediated visualization of actin and myosin filaments in the contractile membrane-cytoskeleton complex of dictyostelium discoideum. *Cell structure and function*, 15(6):355–364, 1990.

[88] Partha Pratim Modal and Alberto Diaspro. *Fundamentals of Fluorescence Microscopy: Exploring Life with Light*. Springer, 2014.

[89] Olesya V Stepanenko, Olga V Stepanenko, Irina M Kuznetsova, Vladislav V Verkhusha, and Konstantin K Turoverov. Beta-barrel scaffold of fluorescent proteins: folding, stability and role in chromophore formation. In *International review of cell and molecular biology*, volume 302, pages 221–278. Elsevier, 2013.

[90] Mats Ormö, Andrew B Cubitt, Karen Kallio, Larry A Gross, Roger Y Tsien, and S James Remington. Crystal structure of the aequorea victoria green fluorescent protein. *Science*, 273(5280):1392–1395, 1996.

[91] Annette Müller-Taubenberger and Kurt I Anderson. Recent advances using green and red fluorescent protein variants. *Applied microbiology and biotechnology*, 77(1):1–12, 2007.

[92] Markus Fischer, Ilka Haase, Evelyn Simmeth, Günther Gerisch, and Annette Müller-Taubenberger. A brilliant monomeric red fluorescent protein to visualize cytoskeleton dynamics in dictyostelium. *FEBS letters*, 577(1-2):227–232, 2004.

[93] Clare M Waterman-Storer, Arshad Desai, J Chloe Bulinski, and ED Salmon. Fluorescent speckle microscopy, a method to visualize the dynamics of protein assemblies in living cells. *Current biology*, 8(22):1227–S1, 1998.

[94] Anne-Catherine Schmit and Anne-Marie Lambert. Microinjected fluorescent phalloidin in vivo reveals the f-actin dynamics and assembly in higher plant mitotic cells. *The Plant Cell*, 2(2):129–138, 1990.

[95] Michael G Lemieux, Dani Janzen, Rander Hwang, Jeannette Roldan, Irene Jarchum, and David A Knecht. Visualization of the actin cytoskeleton: different f-actin-binding probes tell different stories. *Cytoskeleton*, 71(3):157–169, 2014.

[96] Airlie J McCoy, Paola Fucini, Angelika A Noegel, and Murray Stewart. Structural basis for dimerization of the dictyostelium gelation factor (abp120) rod. *Nature structural biology*, 6(9):836–841, 1999.

[97] Ronald R Dubreuil. Structure and evolution of the actin crosslinking proteins. *Bioessays*, 13(5):219–226, 1991.

[98] Ka Ming Pang, Eunkyung Lee, and David A Knecht. Use of a fusion protein between gfp and an actin-binding domain to visualize transient filamentous-actin structures. *Current biology*, 8(7):405–408, 1998.

[99] N. Schneider, I. Weber, J. Faix, J. Prassler, A. Müller-Taubenberger, J. Kohler, E. Burghardt, G. Gerisch, and G. Marriott. A lim protein involved in the progression of cytokinesis and regulation of the mitotic spindle. *Cell Motility and the Cytoskeleton*, 56(2):130–139, 2003.

[100] T Khurana, B Khurana, and AA Noegel. Lim proteins: association with the actin cytoskeleton. *Protoplasma*, 219(1-2):1–12, 2002.

[101] Sharon Chien, Chang Y Chung, Sujatha Sukumaran, Nicholas Osborne, Susan Lee, Charlene Ellsworth, James G McNally, and Richard A Firtel. The dictyostelium lim domain-containing protein lim2 is essential for proper chemotaxis and morphogenesis. *Molecular biology of the cell*, 11(4):1275–1291, 2000.

[102] Bharat Khurana, Taruna Khurana, Nandkumar Khaire, and Angelika A Noegel. Functions of lim proteins in cell polarity and chemotactic motility. *The EMBO journal*, 21(20):5331–5342, 2002.

[103] Josef Prassler, Alexander Murr, Susanne Stocker, Jan Faix, John Murphy, and Gerard Marriott. Ddlim is a cytoskeleton-associated protein involved in the protrusion of lamellipodia in dictyostelium. *Molecular Biology of the Cell*, 9(3):545–559, 1998.

[104] Vedrana Filić, Maja Marinović, Jan Faix, and Igor Weber. A dual role for rac1 gtpases in the regulation of cell motility. *Journal of cell science*, 125(2):387–398, 2012.

[105] Christian Westendorf. *Oscillatory dynamics of the actin cytoskeleton*. Phd thesis, Universität Göttingen, 2012.

[106] Till Bretschneider, Stefan Diez, Kurt Anderson, John Heuser, Margaret Clarke, Annette Müller-Taubenberger, Jana Köhler, and Günther Gerisch. Dynamic actin patterns and arp2/3 assembly at the substrate-attached surface of motile cells. *Current Biology*, 14(1):1–10, 2004.

[107] Julia Riedl, Alvaro H Crevenna, Kai Kessenbrock, Jerry Haochen Yu, Dorothee Neukirchen, Michal Bista, Frank Bradke, Dieter Jenne, Tad A Holak, Zena Werb, et al. Lifeact: a versatile marker to visualize f-actin. *Nature methods*, 5(7):605–607, 2008.

[108] Takeshi Asakura, Takuya Sasaki, Fumiko Nagano, Ayako Satoh, Hiroshi Obaishi, Hideo Nishioka, Hiroshi Imamura, Kazuhiko Hotta, Kazuma Tanaka, Hiroyuki Nakanishi, et al. Isolation and characterization of a novel actin filament-binding protein from saccharomyces cerevisiae. *Oncogene*, 16(1):121–130, 1998.

[109] Jason S King and Robert R Kay. The origins and evolution of macropinocytosis. *Philosophical Transactions of the Royal Society B*, 374(1765):20180158, 2019.

[110] W.F. Loomis. Sensitivity of dictyostelium discoideum to nucleic acid analogues. *Experimental Cell Research*, 64(2):484 – 486, 1971.

[111] Marko Kaksonen, Christopher P Toret, and David G Drubin. Harnessing actin dynamics for clathrin-mediated endocytosis. *Nature reviews Molecular cell biology*, 7(6):404–414, 2006.

[112] Carmen Aguado-Velasco and Mark S Bretscher. Circulation of the plasma membrane in dictyostelium. *Molecular biology of the cell*, 10(12):4419–4427, 1999.

[113] Catherine M Buckley, Navin Gopaldass, Cristina Bosmani, Simon A Johnston, Thierry Soldati, Robert H Insall, and Jason S King. Wash drives early recycling from macropinosomes and phagosomes to maintain surface phagocytic receptors. *Proceedings of the National Academy of Sciences*, 113(40):E5906–E5915, 2016.

[114] Kathryn S Riddelle-Spencer and Theresa J O'halloran. Purification of clathrin heavy and light chain from dictyostelium discoideum. *Protein expression and purification*, 11(3):250–256, 1997.

[115] Douwe M Veltman and Robert H Insall. Wasp family proteins: their evolution and its physiological implications. *Molecular biology of the cell*, 21(16):2880–2893, 2010.

[116] Francesco Baschieri, Stéphane Dayot, Nadia Elkhatib, Nathalie Ly, Anahi Capmany, Kristine Schauer, Timo Betz, Danijela Matic Vignjevic, Renaud Poincloux, and Guillaume Montagnac. Frustrated endocytosis controls contractility-independent mechanotransduction at clathrin-coated structures. *Nature communications*, 9(1):1–13, 2018.

[117] Andrew J. Davidson, Clelia Amato, Peter A. Thomason, and Robert H. Insall. WASP family proteins and formins compete in pseudopod− and bleb−based migration. *Journal of Cell Biology*, 217(2):701–714, 11 2017.

[118] THERESA J O'HALLORAN and RICHARD GW ANDERSON. Characterization of the clathrin heavy chain from dictyostelium discoideum. *DNA and cell biology*, 11(4):321–330, 1992.

[119] Tracy Ruscetti, James A Cardelli, Maria L Niswonger, and Theresa J O'halloran. Clathrin heavy chain functions in sorting and secretion of lysosomal enzymes in dictyostelium discoideum. *The Journal of cell biology*, 126(2):343–352, 1994.

[120] Jingshan Wang, Valerie C Virta, Kathryn Riddelle-Spencer, and Theresa J O'Halloran. Compromise of clathrin function and membrane association by clathrin light chain deletion. *Traffic*, 4(12):891–901, 2003.

[121] M. Tarantola, A. Bae, D. Fuller, E. Bodenschatz, W. J. Rappel, and W. F. Loomis. Cell substratum adhesion during early development of dictyostelium discoideum. *Plos One*, 9(9), 2014.

[122] Rajib Schubert, Nico Strohmeyer, Mitasha Bharadwaj, Subramanian P Ramanathan, Michael Krieg, Jens Friedrichs, Clemens M Franz, and Daniel J Muller. Assay for characterizing the recovery of vertebrate cells for adhesion measurements by single-cell force spectroscopy. *FEBS letters*, 588(19):3639–3648, 2014.

[123] Mitsuyoshi Nakao, Kyungsook Kim, Kenichi Nagase, David W Grainger, Hideko Kanazawa, and Teruo Okano. Phenotypic traits of mesenchymal stem cell sheets fabricated by temperature-responsive cell culture plate: structural characteristics of msc sheets. *Stem cell research & therapy*, 10(1):1–14, 2019.

[124] Yun Dong, Sonbol Shahid-Salles, Dan Sherling, Nathan Fechheimer, Nathan Iyer, Lance Wells, Marcus Fechheimer, and Ruth Furukawa. De novo actin polymerization is required for model hirano body formation in dictyostelium. *Biology open*, 5(6):807–818, 2016.

[125] Hsin-Fang Hsu, Eberhard Bodenschatz, Christian Westendorf, Azam Gholami, Alain Pumir, Marco Tarantola, and Carsten Beta. Variability and order in cytoskeletal dynamics of motile amoeboid cells. *Physical Review Letters*, 119(14):148101, 2017.

[126] D. F. Lusche, D. Wessels, and D. R. Soll. The effects of extracellular calcium on motility, pseudopod and uropod formation, chemotaxis, and the cortical localization of myosin ii in dictyostelium discoideum. *Cell Motility and the Cytoskeleton*, 66(8):567–587, 2009.

[127] Jared C Cochran, Morgan E Thompson, and F Jon Kull. Metal switch-controlled myosin ii from dictyostelium discoideum supports closure of nucleotide pocket during atp binding coupled to detachment from actin filaments. *Journal of Biological Chemistry*, 288(39):28312–28323, 2013.

[128] PC Newell, D Malchow, and JD Gross. The role of calcium in aggregation and development ofdictyostelium. *Experientia*, 51(12):1155–1165, 1995.

[129] Christian Titus Kreis. *Microalgal Adhesion to Model Substrates*. Phd thesis, Universität Göttingen, 2017.

[130] P. Loskill, H. Hähl, N. Thewes, C. T. Kreis, M. Bischoff, M. Herrmann, and K. Jacobs. Influence of the subsurface composition of a material on the adhesion of staphylococci. *Langmuir*, 28(18):7242–7248, 2012.

[131] M. Lessel, O. Bäumchen, M. Klos, H. Hahl, R. Fetzer, M. Paulus, R. Seemann, and K. Jacobs. Self-assembled silane monolayers: an efficient step-by-step recipe for high-quality, low energy surfaces. *Surface and Interface Analysis*, 47(5):557–564, 2015.

[132] Martin P. Stewart, Adrian W. Hodel, Andreas Spielhofer, Cedric J. Cattin, Daniel J. Müller, and Jonne Helenius. Wedged afm-cantilevers for parallel plate cell mechanics. *Methods*, 60(2):186–194, 2013.

[133] Hans-Jürgen Butt, Brunero Cappella, and Michael Kappl. Force measurements with the atomic force microscope: Technique, interpretation and applications. *Surface science reports*, 59(1-6):1–152, 2005.

[134] H-J Butt and Manfred Jaschke. Calculation of thermal noise in atomic force microscopy. *Nanotechnology*, 6(1):1, 1995.

[135] Andreas Janshoff, Marcus Neitzert, York Oberdörfer, and Harald Fuchs. Force spectroscopy of molecular systems?single molecule spectroscopy of polymers and biomolecules. *Angewandte Chemie International Edition*, 39(18):3212–3237, 2000.

[136] Yekaterina A Miroshnikova, Huy Q Le, David Schneider, Torsten Thalheim, Matthias Rübsam, Nadine Bremicker, Julien Polleux, Nadine Kamprad, Marco Tarantola, Irène Wang, et al. Adhesion forces and cortical tension couple cell proliferation and differentiation to drive epidermal stratification. *Nature cell biology*, 20(1):69–80, 2018.

[137] Jens Friedrichs, Kyle R. Legate, Rajib Schubert, Mitasha Bharadwaj, Carsten Werner, Daniel J. Müller, and Martin Benoit. A practical guide to quantify cell adhesion using single-cell force spectroscopy. *Methods*, 60(2):169–178, 2013.

[138] Ediz Sariisik, Denitsa Docheva, Daniela Padula, Cvetan Popov, Jan Opfer, Matthias Schieker, Hauke Clausen-Schaumann, and Martin Benoit. Probing the interaction forces of prostate cancer cells with collagen i and bone marrow derived stem cells on the single cell level. *PLoS One*, 8(3):e57706, 2013.

[139] Jens Friedrichs, Jonne Helenius, and Daniel J Müller. Stimulated single-cell force spectroscopy to quantify cell adhesion receptor crosstalk. *Proteomics*, 10(7):1455–1462, 2010.

[140] Gilbert Ng, Karan Sharma, Sandra M Ward, Melanie D Desrosiers, Leslie A Stephens, W Michael Schoel, Tonglei Li, Clifford A Lowell, Chang-Chun Ling, Matthias W Amrein, et al. Receptor-independent, direct membrane binding leads to cell-surface lipid sorting and syk kinase activation in dendritic cells. *Immunity*, 29(5):807–818, 2008.

[141] J. Friedrichs, J. Helenius, and D. J. Muller. Quantifying cellular adhesion to extracellular matrix components by single-cell force spectroscopy. *Nature Protocols*, 5(7):1353–1361, 2010.

[142] Danny Fuller, Wen Chen, Micha Adler, Alex Groisman, Herbert Levine, Wouter-Jan Rappel, and William F Loomis. External and internal constraints on eukaryotic chemotaxis. *Proceedings of the National Academy of Sciences*, 107(21):9656–9659, 2010.

[143] George Biddell Airy. On the diffraction of an object-glass with circular aperture. *TCaPS*, 5:283, 1835.

[144] Richard W Cole, Tushare Jinadasa, and Claire M Brown. Measuring and interpreting point spread functions to determine confocal microscope resolution and ensure quality control. *Nature protocols*, 6(12):1929–1941, 2011.

[145] G Toraldo Di Francia. Super-gain antennas and optical resolving power. *Il Nuovo Cimento (1943-1954)*, 9(3):426–438, 1952.

[146] Ralph Gräf, Jens Rietdorf, and Timo Zimmermann. Live cell spinning disk microscopy. In *Microscopy techniques*, pages 57–75. Springer, 2005.

[147] AFM Tariqul Islam, Haicen Yue, Margarethakay Scavello, Pearce Haldeman, Wouter-Jan Rappel, and Pascale G Charest. The camp-induced g protein subunits dissociation monitored in live dictyostelium cells by bret reveals two activation rates, a positive effect of caffeine and potential role of microtubules. *Cellular signalling*, 48:25–37, 2018.

[148] Daniela Gabriel, Ulrike Hacker, J. Köhler, A. Müller-Taubenberger, Jean-Marc Schwartz, Monika Westphal, and Günther Gerisch. The contractile vacuole network of dictyostelium as a distinct organelle: its dynamics visualized by a gfp marker protein. *Journal of cell science*, 112(22):3995–4005, 1999.

[149] Steven Vogel. *Comparative biomechanics: life's physical world*. Princeton University Press, 2013.

[150] H. Leonhardt, M. Gerhardt, N. Höppner, K. Kruger, M. Tarantola, and C. Beta. Cell-substrate impedance fluctuations of single amoeboid cells encode cell-shape and adhesion dynamics. *Physical Review E*, 93(1), 2016.

[151] T. J. Lampert, N. Kamprad, M. Edwards, J. Borleis, A. J. Watson, M. Tarantola, and P. N. Devreotes. Shear force-based genetic screen reveals negative regulators of cell adhesion and protrusive activity. *Proceedings of the National Academy of Sciences of the United States of America*, 114(37):E7727–E7736, 2017.

[152] Bryan A Millis. Evanescent-wave field imaging: an introduction to total internal reflection fluorescence microscopy. In *Molecular Profiling*, pages 295–309. Springer, 2012.

[153] ibidi. *Instructions μ-Dish^{35mm,high} Glass Bottom*, 5 2015.

[154] Jude Hemanth and Valentina Emilia Balas. *Biologically Rationalized Computing Techniques For Image Processing Applications*. Springer, 2018.

[155] Zdravko I Botev, Joseph F Grotowski, Dirk P Kroese, et al. Kernel density estimation via diffusion. *The annals of Statistics*, 38(5):2916–2957, 2010.

[156] Hsin-Fang Hsu. *Oscillatory instabilities of intracellular fiber networks*. PhD thesis, Georg-August University School of Science (GAUSS) Göttingen, 2015.

[157] Peter Moritz Loskill. *Unraveling the impact of subsurface and surface properties of a material on biological adhesion-a multi-scale approach*. Phd thesis, Universität Saarland, 2012.

[158] N Kamprad and M Tarantola. The dual role of actin foci in adhesion and endocytosis of dictyostelium discoideum. In *Technische Systeme für die Lebenswissenschaften*. Institut für Bioprozess- und Analysenmesstechnik e.V., 2018.

[159] Doris Heinrich, Simon Youssef, Britta Schroth-Diez, Ulrike Engel, Daniel Aydin, Jacques Blümmel, Joachim Pius Spatz, and Günther Gerisch. Actin-cytoskeleton dynamics in non-monotonic cell spreading. *Cell adhesion & migration*, 2 2:58–68, 2008.

[160] Benjamin Geiger, Joachim P Spatz, and Alexander D Bershadsky. Environmental sensing through focal adhesions. *Nature reviews Molecular cell biology*, 10(1):21–33, 2009.

[161] J Thomas Parsons, Alan Rick Horwitz, and Martin A Schwartz. Cell adhesion: integrating cytoskeletal dynamics and cellular tension. *Nature reviews Molecular cell biology*, 11(9):633–643, 2010.

[162] S Gon, Kushi-Nidhi Kumar, Klaus Nüsslein, and Maria M Santore. How bacteria adhere to brushy peg surfaces: Clinging to flaws and compressing the brush. *Macromolecules*, 45(20):8373–8381, 2012.

[163] Tzvetelina Tzvetkova-Chevolleau, Edward Yoxall, David Fuard, Franz Bruckert, Patrick Schiavone, and Marianne Weidenhaupt. Microscale adhesion patterns for the precise localization of amoeba. *Microelectronic engineering*, 86(4-6):1485–1487, 2009.

[164] C. L. Wang, S. Chowdhury, M. Driscoll, C. A. Parent, S. K. Gupta, and W. Losert. The interplay of cell-cell and cell-substrate adhesion in collective cell migration. *Journal of the Royal Society Interface*, 11(100), 2014.

[165] Dirk Dormann and Cornelis J Weijer. Propagating chemoattractant waves coordinate periodic cell movement in dictyostelium slugs. *Development*, 128(22):4535–4543, 2001.

[166] Satoshi Sawai, Yasuo Maeda, and Yasuji Sawada. Spontaneous symmetry breaking turing-type pattern formation in a confined dictyostelium cell mass. *Physical Review Letters*, 85(10):2212, 2000.

[167] Alice Y Pollitt, Simone L Blagg, Neysi Ibarra, and Robert H Insall. Cell motility and scar localisation in axenically growing dictyostelium cells. *European journal of cell biology*, 85(9-10):1091–1098, 2006.

[168] Gene information for tala. *Dicty Base*, http://dictybase.org/gene/DDB_G0290481, 2010.

[169] C. P. McCann, E. C. Rericha, C. L. Wang, W. Losert, and C. A. Parent. Dictyostelium cells migrate similarly on surfaces of varying chemical composition. *Plos One*, 9(2), 2014.

[170] R. Froquet, M. le Coadic, J. Perrin, N. Cherix, S. Cornillon, and P. Cosson. Tm9/phg1 and sada proteins control surface expression and stability of siba adhesion molecules in dictyostelium. *Molecular Biology of the Cell*, 23(4):679–686, 2012.

[171] Luis R Flores, Michael C Keeling, Xiaoli Zhang, Kristina Sliogeryte, and Núria Gavara. Lifeact-taggfp2 alters f-actin organization, cellular morphology and biophysical behaviour. *Scientific reports*, 9(1):1–13, 2019.

[172] Onnik Agbulut, Catherine Coirault, Nicolas Niederländer, Alexis Huet, Patrick Vicart, Albert Hagège, Michel Puceat, and Philippe Menasche. Gfp expression in muscle cells impairs actin-myosin interactions: implications for cell therapy. *Nature methods*, 3(5):331–331, 2006.

[173] JVF Coumans, David Gau, Anne Poljak, V Wasinger, Partha Roy, and Pierre Moens. Green fluorescent protein expression triggers proteome changes in breast cancer cells. *Experimental cell research*, 320(1):33–45, 2014.

[174] Sheri L Moores, James H Sabry, and James A Spudich. Myosin dynamics in live dictyostelium cells. *Proceedings of the National Academy of Sciences*, 93(1):443–446, 1996.

[175] N. Thewes, P. Loskill, P. Jung, H. Peisker, M. Bischoff, M. Herrmann, and K. Jacobs. Hydrophobic interaction governs unspecific adhesion of staphylococci: a

single cell force spectroscopy study. *Beilstein Journal of Nanotechnology*, 5:1501–1512, 2014.

[176] Christian Titus Kreis, Alice Grangier, and Oliver Bäumchen. In vivo adhesion force measurements of chlamydomonas on model substrates. *Soft Matter*, 15(14):3027–3035, 2019.

[177] Yuan Lin and LB Freund. Forced detachment of a vesicle in adhesive contact with a substrate. *International journal of solids and structures*, 44(6):1927–1938, 2007.

[178] V.A. Parsegian. van der waals forces. *Cambrigdge University Press*, 2006.

[179] Marius Socol, Christine Lefrou, Franz Bruckert, Didier Delabouglise, and Marianne Weidenhaupt. Synchronization of dictyostelium discoideum adhesion and spreading using electrostatic forces. *Bioelectrochemistry*, 79(2):198–210, 2010.

[180] YASUO MAEDA. Changes in charged groups on the cell surface during development of the cellular slime mold dictyostelium discoideum: an electron microscopic study. *Development, Growth & Differentiation*, 22(4):679–685, 1980.

[181] RAYMOND Hellio and ANTOINETTE Ryter. Role of particle electrostatic charge in adhesion and ingestion in dictyostelium discoideum amoeboid cells. *Journal of cell science*, 79(1):327–342, 1985.

[182] Zihe Rao, Penny Handford, Mark Mayhew, Vroni Knott, George G Brownlee, and David StuartZ. The structure of a ca2+-binding epidermal growth factor-like domain: its role in protein-protein interactions. *Cell*, 82(1):131–141, 1995.

[183] Christian Titus Kreis, Marine Le Blay, Christine Linne, Marcin Michal Makowski, and Oliver Bäumchen. Adhesion of chlamydomonas microalgae to surfaces is switchable by light. *Nature Physics*, 14(1):45–49, 2018.

[184] Somayeh Ramezanian, Hien Xuan Ta, Balasingam Muhunthan, and Nehal Abu-Lail. Role of ionic strength in the retention and initial attachment of pseudomonas putida to quartz sand. *Biointerphases*, 13(4):041005, 2018.

[185] Marie-Josée Colbert, Françoise Brochard-Wyart, Cécile Fradin, and Kari Dalnoki-Veress. Squeezing and detachment of living cells. *Biophysical journal*, 99(11):3555–3562, 2010.

[186] Ediz Sariisik, Cvetan Popov, Jochen P Müller, Denitsa Docheva, Hauke Clausen-Schaumann, and Martin Benoit. Decoding cytoskeleton-anchored and non-anchored receptors from single-cell adhesion force data. *Biophysical journal*, 109(7):1330–1333, 2015.

[187] Michael Krieg, Jonne Helenius, Carl-Philipp Heisenberg, and Daniel J Muller. A bond for a lifetime: employing membrane nanotubes from living cells to determine receptor–ligand kinetics. *Angewandte Chemie*, 120(50):9921–9923, 2008.

[188] Joe Chin-Hun Kuo, Jay G Gandhi, Roseanna N Zia, and Matthew J Paszek. Physical biology of the cancer cell glycocalyx. *Nature Physics*, 14(7):658–669, 2018.

[189] Samuel Hertig and Viola Vogel. Catch bonds. *Current Biology*, 22(19):R823–R825, 2012.

[190] Christoph Schich. Interplay of actin foci and clathrin rich areas upon dictyostelium discoideum adhesion. Master's thesis, Universität Göttingen, 2020.

[191] Douwe M. Veltman, Jason S. King, Laura M. Machesky, and Robert H. Insall. SCAR knockouts in Dictyostelium: WASP assumes SCAR's position and upstream regulators in pseudopods. *Journal of Cell Biology*, 198(4):501–508, 08 2012.

[192] Marcel Schröder. Cell-substrate adhesion and contact guidance of dictyostelium discoideum on surfaces of varying curvatures. Master's thesis, Universität Göttingen, 2018.

[193] Christof Litschko, Stefan Brühmann, Agnes Csiszár, Till Stephan, Vanessa Dimchev, Julia Damiano-Guercio, Alexander Junemann, Sarah Körber, Moritz Winterhoff, Benjamin Nordholz, et al. Functional integrity of the contractile actin cortex is safeguarded by multiple diaphanous-related formins. *Proceedings of the National Academy of Sciences*, 116(9):3594–3603, 2019.

[194] Marco Fritzsche, Christoph Erlenkämper, Emad Moeendarbary, Guillaume Charras, and Karsten Kruse. Actin kinetics shapes cortical network structure and mechanics. *Science advances*, 2(4):e1501337, 2016.

[195] Masatsune Tsujioka, Taro Q. P. Uyeda, Yoshiaki Iwadate, Hitesh Patel, Keitaro Shibata, Tenji Yumoto, and Shigenobu Yonemura. Actin-binding domains mediate the distinct distribution of two dictyostelium talins through different affinities to specific subsets of actin filaments during directed cell migration. *PLOS ONE*, 14(4):1–22, 04 2019.

[196] M. Benoit, D. Gabriel, G. Gerisch, and H. E. Gaub. Discrete interactions in cell adhesion measured by single-molecule force spectroscopy. *Nat Cell Biol*, 2(6):313–7, 2000.

[197] Hyejeong Kim, Hannes Witt, Tabea Oswald, and Marco Tarantola. Adhesion of epithelial cells to pnipam treated surfaces for temperature-controlled cell sheet harvesting. *ACS Applied Materials & Interfaces*, 2020.

[198] Douwe M Veltman, Thomas D Williams, Gareth Bloomfield, Bi-Chang Chen, Eric Betzig, Robert H Insall, and Robert R Kay. A plasma membrane template for macropinocytic cups. *Elife*, 5:e20085, 2016.

[199] T. Salditt, A. Egner, and D. Russel Luke. *Nanoscale Photonic Imaging*. Springer International Publishing, 1 edition, 2020.

Acknowledgments

I would like to thank Dr. Marco Tarantola for guiding me during my PhD and teaching me to conduct independent research. The work presented in this dissertation would not have been possible without him pointing me to interesting fields of research and arranging appropriate contacts. Prof. Dr. A. Janshoff is one of these contacts. I would like to thank him for providing technical know-how, expertise as well as social commitment. Dr. Tarantola's supervision always focused on allowing independent research while providing advice and help whenever it was needed.

My thanks to Prof. Dr. Bodenschatz for allowing me to work in his group, which is a unique mixture of theoretical and experimental approaches. This mixture runs through the entire institute. At this point, I would also like to thank Dr. Bäumchen and Dr. Kreis for the successful collaboration. I thank the DFG for funding this project - A08 in SFB937 and for the uncomplicated extension during my parental leave.

With regard to my experimental work, I thank Maren Stellar Müller for providing the cell culture I worked with. Furthermore, I thank Katharina Gunkel, who always made time for my questions. In terms of scientific discussions and advice, I thank Dr. Turco, Dr. Westendorf and Dr. Bae who were helpful in analysing the data.

Finally, thank you to my family who motivated and supported me. Thanks to Benjamin, who believes in me, puts up with my moods and supports me in balancing science and family.